On using
the interleaved Numerical Renormalization Group
as an impurity solver for
the Dynamical Mean Field Theory

Andreas Gleis
Bachelor thesis

chair of theoretical solid state physics
faculty of physics
Ludwig-Maximilians-Universität München

Supervisor:
Prof. Dr. Jan von Delft

Über die Nutzung der seriellen Numerischen Renormalisierungsgruppe als Störstellen Löser für die Dynamische Molekularfeldtheorie

Andreas Gleis
Bachelorarbeit

Lehrstuhl für theoretische Festkörperphysik
Fakultät für Physik
Ludwig-Maximilians-Universität München

Betreuer:
Prof. Dr. Jan von Delft

Contents

1. Introduction 3

I. Theory 5

2. Dynamical mean field theory (DMFT) 7
  2.1. Classical mean field theory . . . 7
  2.2. General procedure of DMFT . . . 8
  2.3. Lattice Green's function . . . 9
  2.4. Impurity Green's function . . . 11
  2.5. General DMFT equations and iterative procedure . . . 11
  2.6. DMFT on the Bethe lattice . . . 12

3. Numerical Renormalization Group (NRG) 15
  3.1. Hamiltonian . . . 15
  3.2. General Procedure . . . 15
  3.3. Discretization of the bath . . . 16
  3.4. Mapping on semi-infinite tight binding chain . . . 17
  3.5. Iterative Diagonalization . . . 19
  3.6. Matrix product states and symmetries . . . 22
  3.7. Approximate complete eigenbasis and full density matrix . . . 24
  3.8. Calculation of spectral functions . . . 25

4. Interleaved Numerical Renormalization Group 27
  4.1. Basic concept . . . 27
  4.2. z-averaging within iNRG . . . 29

5. Using NRG as an impurity solver for DMFT 31
  5.1. Self energy trick . . . 31
  5.2. Logarithmic discretization within DMFT . . . 31

6. Anderson-Hund model (AHM) 35

II. Results 37

7. One band Anderson Hund Model 39
  7.1. Basic results without z-shifting . . . 39

7.2. Z-averaging for the one band model . . . 45
7.3. One-band Mott insulator transition (MIT) . . . 49

8. Two band Anderson Hund Model 51
8.1. Band symmetric results without z-averaging . . . 51
8.2. Bandsymmetric results with z-averaging . . . 55
8.3. Bandsymmetric two band Mott insulator transition . . . 60
8.4. Band asymmetric two band results . . . 64

9. Three band Anderson Hund Model 69
9.1. Band symmetric three band results without z-averaging . . . 69
9.2. Band symmetric results with z-averaging . . . 72
9.3. Band symmetric three band Mott insulator transition (MIT) . . . 78
9.4. Band-asymmetric three band results . . . 80

10. Conclusion and outlook 89

III. Appendix 91

A. Basics of quantum many-particle theory 93

B. Calculation of the Lattice Green's Function 95

C. Calculation of the Impurity Green's Function 97

D. NRG transformation 99
D.1. Hamiltonian . . . 99
D.2. Logarithmic Discretization . . . 99
D.3. First Transformation . . . 100
D.4. Second Transformation (mapping on semi-infinite tight-binding-chain) . . . 101

1. Introduction

Materials with strong electron-electron interactions compared to the kinetic energy, are a considerable challenge in condensed matter physics as perturbation methods cannot be applied.

Strong electronic correlations arise typically for materials with partially filled d- or f-shells which are spatially more confined than s- or p-shells. This leads to a small overlap of orbitals between neighboring atoms and therefore low kinetic energies, rising the importance of electron-electron interactions. Examples are transition metals and their oxides, ruthenates and iron pnictides. They exhibit strongly correlated many body phenomena such as the Mott metal-insulator (MIT) transition or high temperature superconductivity.

To treat such materials theoretically a quantum mean field approach, the Dynamical Mean field theory (DMFT), has been developed [6],[14]. It treats an arbitrary site of the lattice model as an impurity coupled to a non-interacting bath with effective parameters, presenting the rest of the lattice. These effective parameters are determined self consistently.

As DMFT reduces the lattice model to an effective quantum impurity model, an accurate impurity solver is needed to obtain a correct description of the material physics. A good choice is the Numerical Renormalization (NRG) which was first used by K.G.Wilson to treat the Kondo model [18]. It applies a logarithmic discretization to the bath with exponentially improved resolution around the Fermi-level, yielding highly accurate real-frequency spectral resolution at arbitrary low energies. However the computational effort of NRG scales exponentially with the number of considered bands (orbitals) in DMFT. While one and two-band calculations can still be performed with NRG using modern computers, three band calculations are only possible if the models exhibit additional band symmetries that can be exploited in the NRG procedure.

For ruthenates and iron pnictides, the interesting physical properties arise from the interplay of up to 5 bands. Due to crystal field splitting the degeneracy of some bands is usually broken. Thus standard NRG methods cannot be used to study these highly relevant models.

Only recently a modification of NRG, called interleaved NRG (iNRG), has been developed by A. Mitchell [8] which reduces the exponential scaling with the number of bands. The method was implemented and already tested as an impurity solver in the group of Jan von Delft at LMU Munich by Katharina Stadler [11] for up to three-channel impurity models and turned out to be very reliable.

In this thesis we will now test the performance of iNRG as an impurity solver for DMFT, using the codes of Andreas Weichselbaum and Katharina Stadler.

In the first part of this thesis the basic theoretical background of the applied methods

will be discussed. Before presenting the standard NRG (sNRG) method and the iNRG modification in chapter 3 and chapter 4, respectively, DMFT will be introduced in chapter 2. We will then discuss the characteristics arising when NRG methods are used as an impurity solver for DMFT in chapter 5 and at last introduce the Anderson Hund Model in chapter 6, which was used as a test model for our results in the second part.
The second part starts with simple one band calculations in chapter 7. Here we will perform a first quality check of the DMFT+iNRG method by comparing the results with corresponding sNRG calculations. We will first perform two basic one-band calculations and compare spectral data and Wilson chain couplings of iNRG and sNRG results. After that we will examine the performance of z-averaging in iNRG and last but not least the one-band Mott insulator transition will be studied. In chapter 8 we will turn to two band calculations. First we will the two-band Anderson Hund model with band symmetry and we again start by examining simple results and then turn to the performance of z-averaging. After that we study the band-symmetric Mott insulator transition in great detail. Chapter 8 will be finished with examining asymmetric two band models and comparing iNRG with sNRG results. Last but not least chapter 9 will treat three band DMFT+NRG calculations. Here sNRG results are available only for the band-symmetric case, as sNRG is computationally too costly if no band-symmetry can be exploited. In the first part of chapter 9 band-symmetric calculations for both iNRG and sNRG are compared and the performance of z-shifting is again tested. In the second part of chapter 9 we will show band-asymmetric three band calculations that have been achieved with the DMFT+iNRG approach.
Chapter 10 gives a conclusion of our results and provides an outlook to possible future directions based on the iNRG+DMFT approach.

Part I.

Theory

2. Dynamical mean field theory (DMFT)

First steps towards DMFT were delivered by D. Vollhardt and W. Metzner in their work on the Hubbard model in infinite dimensions [7], the basic DMFT framework was then later established by A. Georges and G. Kotliar in [5]. DMFT is a mean field approximation to treat quantum lattice problems. It freezes out spacial fluctuations but takes into account temporal quantum fluctuations and is therefore dynamical. Good reviews on DMFT can be found in [14] and [6]. To get an understanding of the basic ideas of DMFT it is instructive to shortly recapitulate classical mean field theory in the context of the Ising model.

2.1. Classical mean field theory

The Ising model describes spins on a lattice interacting with nearest neighbors and an external magnetic field. It is described by the following Hamiltonian:

$$H = -\frac{1}{2}\sum_{(i,j)} J_{ij} S_i S_j - h \sum_i S_i \quad , \tag{2.1}$$

where $\sum_{(i,j)}$ is a sum over all pairs of nearest neighbors with ferromagnetic couplings $J_{ij} > 0$. $\sum_i$ is a sum over all lattice sites and h an external field. The goal of a mean field approach is now to reduce the complex lattice model to an effective single site problem. For the Ising model this can be done with the approximation $\Delta S_i \Delta S_j = 0$, where $\Delta S_i \equiv S_i - \langle S_i \rangle$ was defined:

$$\begin{aligned} H &= -\frac{1}{2}\sum_{(i,j)} J_{ij}(\langle S_i \rangle + \Delta S_i)(\langle S_j \rangle + \Delta S_j) - \sum_i h S_i \\ &\simeq -\frac{1}{2}\sum_{(i,j)} J_{ij}(\langle S_i \rangle \langle S_j \rangle + \Delta S_i \langle S_j \rangle + \Delta S_j \langle S_i \rangle) - \sum_i h S_i = \tilde{H} \end{aligned} \tag{2.2}$$

With the assumption of a translational invariant system, in other terms $\langle S_i \rangle = \langle S_j \rangle \equiv \langle S \rangle$ and $J_{ij} \equiv J$, our approximate form of H becomes

$$
\begin{aligned}
\tilde{H} &= -\frac{1}{2}\sum_{(i,j)} J(\langle S \rangle^2 + \Delta S_i \langle S \rangle + \Delta S_j \langle S \rangle) - \sum_i h S_i \\
&= \sum_i \left[-\sum_{nn} \frac{1}{2} J(\langle S \rangle^2 + 2 \cdot \Delta S_i \langle S \rangle) - h S_i \right] \\
&= \sum_i \left[\sum_{nn} (\frac{1}{2} J \langle S \rangle^2 - J S_i \langle S \rangle) - h S_i \right] \\
&= \frac{1}{2} z N J \langle S \rangle^2 - \sum_i S_i \left[z J \langle S \rangle + h \right] = E_0 - h_{eff} \sum_i S_i \quad ,
\end{aligned}
\tag{2.3}
$$

where N is the total number of sites and z is the coordination number. $E_0 = \frac{1}{2} z N J \langle S \rangle^2$ is just an energy offset and thus physically irrelevant. $-h_{eff} \sum_i S_i$ is the Hamiltonian of N noninteracting spins in an external field $h_{eff} = zJ \langle S \rangle + h$, which yields for the magnetization $\langle S \rangle$:

$$
\langle S \rangle = \tanh(\beta h_{eff}) = \tanh(\beta z J \langle S \rangle + \beta h) \tag{2.4}
$$

Eq. (2.4) is a self consistency equation for $\langle S \rangle$. The mean field approximation $\langle \Delta S_i \Delta S_j \rangle = 0$ becomes exact in the limit of infinite coordination number where we have to rescale J

$$
J = \frac{\tilde{J}}{z}, \quad \tilde{J} = const. \tag{2.5}
$$

to get physical quantities like the magnetization to remain finite. In the following section we will extend the concepts discussed here to quantum lattice models with arbitrary on site interactions, following the ideas given in [14], [6] and [13].

2.2. General procedure of DMFT

Within DMFT a quantum lattice model is mapped self consistently on an effective single site quantum impurity model.
The lattice model exhibits nearest neighbor hopping and arbitrary on site interactions, but no site to site interactions. In general, the form of the Hamiltonian of the lattice model is

$$
H_{\text{latt}} = \sum_{\nu,i} (\varepsilon_{d,\nu} - \mu) n_{\nu,i} + \sum_i H_i^{\text{int}} + \sum_\nu \sum_{\langle i,j \rangle} t_\nu c_{\nu,i}^\dagger c_{\nu,j} \tag{2.6}
$$

where $c_{\nu,i}^{(\dagger)}$ are (creation) annihilation operators for electrons of type ν on site i. $\nu = (\sigma, m)$ is a composite index of spin $\sigma \in \{\uparrow, \downarrow\}$ and orbital number $m \in \{1, \dots, N_c\}$ with number operator $n_{\nu,i} = c_{\nu,i}^\dagger c_{\nu,i}$, flavor-dependent energy $\varepsilon_{d,\nu}$ and chemical potential μ. $\sum_{\langle i,j \rangle}$ is a sum over all pairs of nearest neighbors, coupled with hopping amplitude t_ν.

H_i^{int} is an arbitrary interaction Hamiltonian for site i. An example for the specific form of H_i^{int} is given in Sec. 6.
In the quantum mean-field approach, the lattice model is mapped onto a quantum impurity model with effective parameters, that exhibits the same local interaction term as the original model:

$$H = H_{\text{imp}} + H_{\text{hyb}} + H_{\text{bath}} \quad , \tag{2.7}$$

$$H_{\text{bath}} = \sum_{\nu} \sum_{k \in 1.BZ} (\varepsilon_{k,\nu} - \mu) c^{\dagger}_{\nu,k} c_{\nu,k} \quad , \tag{2.8}$$

$$H_{\text{imp}} = \sum_{\nu} (\varepsilon_{d,\nu} - \mu) d^{\dagger}_{\nu} d_{\nu} + H^{\text{int}} \quad , \tag{2.9}$$

$$H_{\text{hyb}} = \sum_{\nu} \sum_{k \in 1.BZ} V_k^{\nu} (d^{\dagger}_{\nu} c_{\nu,k} + c^{\dagger}_{\nu,k} d_{\nu}) \quad . \tag{2.10}$$

Eq. (2.8) describes a non-interacting bath with dispersion relation $\varepsilon_{k,\nu}$ and annihilation operators $c_{k,\nu}$ for bath electrons with momentum k and flavor ν. The Hamiltonian Eq. (2.9) describes a single site (impurity) with the same local interactions as the lattice model with flavor dependent binding energy $\varepsilon_{d,\nu}$, annihilation operators d_{ν} and local interaction H^{int}. H_{hyb} in Eq. (2.10) couples bath and impurity with hybridization V_k. In this impurity model Hamiltonian H_{hyb} and H_{bath} have to be determined self-consistent. This is done by demanding that the on site lattice Green's function $\langle\langle c_{\nu,i}, c^{\dagger}_{\nu,i} \rangle\rangle_{\omega}$ equals the impurity Green's function $\langle\langle d_{\nu}, d^{\dagger}_{\nu} \rangle\rangle_{\omega}$ and the on site lattice self-energy $\Sigma_{latt}(\omega)$ equals the impurity self-energy $\Sigma_{imp}(\omega)$, where the approximation of a k-independent lattice self-energy has to be made. When these steps are performed, one arrives at a self-consistency equation for the hybridization function

$$\Delta_{\nu}(\omega) = \sum_{k \in 1.BZ} \frac{V_k^2}{\omega - \varepsilon_{k,\nu}} \tag{2.11}$$

which fully determines the interplay of bath and impurity. The exact form of H_{hyb} and H_{bath} is not needed. In the following sections these steps will be performed explicitly. For simplicity, the index ν will be dropped.

2.3. Lattice Green's function

In the interacting lattice model (2.6), the non-interacting part is diagonal in k-space with (creation) annihilation operators $c_k^{(\dagger)}$ and dispersion relation ε_k. It can therefore (without index ν) be written as

$$H_{latt} = \sum_{k \in 1.BZ} (\varepsilon_k - \mu) c^{\dagger}_k c_k + \sum_i H_i^{int} \tag{2.12}$$

To solve the lattice model, we calculate the lattice Green's function $\langle\langle c_k, c^{\dagger}_k \rangle\rangle_{\omega}$. With an equation of motion ansatz we get the following expression:

$$\omega \, \langle\langle c_k, c^{\dagger}_k \rangle\rangle_{\omega} = \langle [c_k, c^{\dagger}_k]_+ \rangle_T + \langle\langle [c_k, H_{latt}]_-, c^{\dagger}_k \rangle\rangle_{\omega} \tag{2.13}$$

Here, $\langle ... \rangle_T$ is the thermodynamic average in the grand canonical ensemble, $[...]_+$ is the anticommutator and $[...]_-$ the commutator. $\langle [c_k, c_k^\dagger]_+ \rangle_T = 1$ follows from the fermionic anticommutation relations. $\langle\langle [c_k, H_{latt}]_-, c_k^\dagger \rangle\rangle_\omega$ is calculated in appendix B and yields

$$\langle\langle [c_k, H_{latt}]_-, c_k^\dagger \rangle\rangle_\omega = (\varepsilon_k - \mu) \langle\langle c_k, c_k^\dagger \rangle\rangle_\omega + \Sigma_{latt}(k,\omega) \langle\langle c_k, c_k^\dagger \rangle\rangle_\omega . \tag{2.14}$$

With this expression we get

$$\langle\langle c_k, c_k^\dagger \rangle\rangle_\omega = \frac{1}{\omega - \varepsilon_k + \mu - \Sigma_{latt}(k,\omega)} \tag{2.15}$$

for the k-dependent lattice Green's function.
To map this onto an impurity model, we need to get an expression for the local Green's function of a single site via fourier transformation:

$$\begin{aligned} \langle\langle c_i, c_i^\dagger \rangle\rangle_\omega &= \frac{1}{N} \sum_{k \in 1.BZ} e^{ik(R_i - R_i)} \langle\langle c_k, c_k^\dagger \rangle\rangle_\omega \\ &= \frac{1}{N} \sum_{k \in 1.BZ} \frac{1}{\omega - \varepsilon_k + \mu - \Sigma(k,\omega)} \end{aligned} \tag{2.16}$$

Here, N is the total number of k vectors in the first Brillouin zone. The problem with the above expression is the k-dependence of the self-energy $\Sigma_{latt}(k, \omega)$. This is where the DMFT-approximation comes in: we strip the k-dependence of the self-energy or in other words, we take the self-energy to be purely local.

$$\begin{aligned} &\Sigma_{latt}(k,\omega) \to \Sigma_{latt}(\omega) \\ &\Sigma_{i,j}(\omega) \to \Sigma_{i,j}(\omega)\delta_{i,j} \end{aligned} \tag{2.17}$$

With this approximation and the density of states of the non interacting lattice, $\rho_0(\varepsilon)$, we get an expression for the single site Green's function we can handle:

$$\begin{aligned} \langle\langle c_i, c_i^\dagger \rangle\rangle_\omega &\simeq \frac{1}{N} \sum_{k \in 1.BZ} \frac{1}{\omega - \varepsilon_k + \mu - \Sigma_{latt}(\omega)} \\ &= \int_{-\infty}^{\infty} d\varepsilon \quad \frac{\rho_0(\varepsilon)}{\omega - \varepsilon + \mu - \Sigma_{latt}(\omega)} \end{aligned} \tag{2.18}$$

As in in [13], [14] and [6], it can be shown that the approximation of a momentum independent self-energy becomes exact for an infinite coordination number. The main arguments involve a $\frac{1}{\sqrt{z}}$ scaling of the nearest neighbor hopping amplitude to get a finite density of states for $z \to \infty$. This then leads to a $\left(\frac{1}{\sqrt{z}}\right)^{|R_i - R_j|}$ dependence of $\langle\langle c_i, c_j^\dagger \rangle\rangle_\omega$, with $|R_i - R_j|$ measured in the Manhattan metric in terms of the lattice constant (i.e. $|R_i - R_j| = 2$ for next nearest neighbors), collapsing the perturbation expansion of the self-energy in position space to the same site.

2.4. Impurity Green's function

In order to map the lattice model on an impurity model, we need the impurity Green's function of the impurity model corresponding to our lattice model. The impurity model consists of an impurity Hamiltonian H_{imp}, a non-interacting bath H_{bath} and a hybridization term that couples bath and impurity, H_{hyb}. For the full Hamiltonian of the model we get:

$$\begin{aligned}
H_{imp} &= (\varepsilon_d - \mu)d^\dagger d + H_{int}^{imp} \\
H_{bath} &= \sum_{k\in 1.BZ} (\varepsilon_k - \mu)c_k^\dagger c_k \\
H_{hyb} &= \sum_{k\in 1.BZ} V_k(d^\dagger c_k + c_k^\dagger d) \\
H &= H_{imp} + H_{bath} + H_{hyb}
\end{aligned} \tag{2.19}$$

We now seek an expression for the impurity Green's function $\langle\langle d, d^\dagger\rangle\rangle_\omega$. The explicit calculation is done in appendix C with the following result:

$$\begin{aligned}
\langle\langle d, d^\dagger\rangle\rangle_\omega &= \frac{1}{\omega - \varepsilon_d + \mu - \sum_k \frac{V_k^2}{\omega-\varepsilon_k} - \Sigma_{imp}(\omega)} \\
&= \frac{1}{\omega - \varepsilon_d + \mu - \Delta(\omega) - \Sigma_{imp}(\omega)},
\end{aligned} \tag{2.20}$$

with the hybridization function $\Delta(\omega)$ defined as

$$\Delta(\omega) \equiv \sum_{k\in 1.BZ} \frac{V_k^2}{\omega - \varepsilon_k}. \tag{2.21}$$

with imaginary part

$$\Gamma(\omega) = -Im(\Delta(\omega)) = \pi \sum_{k\in 1.BZ} V_k^2 \delta(\omega - \varepsilon_k) \tag{2.22}$$

2.5. General DMFT equations and iterative procedure

With the expressions (2.20) for the Green's function of the impurity model, $\langle\langle d, d^\dagger\rangle\rangle_\omega$, and (2.18) for the single site Green's function of the lattice model, $\langle\langle c_i, c_i^\dagger\rangle\rangle_\omega$, we can now map the lattice model onto an effective quantum impurity model. In order to do that, we demand that the single site lattice Green's function equals the impurity Green's function and the local on site lattice self-energy $\Sigma_{latt}(\omega)$ equals the self-energy of the impurity, $\Sigma_{imp}(\omega)$.

$$\langle\langle d, d^\dagger\rangle\rangle_\omega \overset{!}{=} \langle\langle c_i, c_i^\dagger\rangle\rangle_\omega \tag{2.23}$$

$$\Sigma_{imp}(\omega) \overset{!}{=} \Sigma_{latt}(\omega) \equiv \Sigma(\omega) \tag{2.24}$$

With those two equations and ε_d in equation (2.20) given by the model we consider, the form of $\Delta(\omega)$ in equation (2.20) is determined uniquely.

$$\begin{aligned}\Delta(\omega) &= \omega - \varepsilon_d + \mu - \Sigma_{imp}(\omega) - \langle\langle d, d^\dagger \rangle\rangle_\omega^{-1} \\ &\overset{(2.23)}{\underset{(2.24)}{=}} \omega - \varepsilon_d + \mu - \Sigma(\omega) - \langle\langle c_i, c_i^\dagger \rangle\rangle_\omega^{-1}\end{aligned} \tag{2.25}$$

Equation (2.25) is the self consistency equation of DMFT. We start by calculating the non-interacting lattice density of states, $\rho_0(\varepsilon)$ and taking some arbitrary initial on site self-energy $\Sigma(\omega)$, i.e. $\Sigma(\omega) = 0$. With this starting condition an iterative procedure follows:

1. The on site lattice Green's function is calculated via equation (2.18)
2. With equation (2.25) the hybridization function for the impurity model is calculated
3. A new local self-energy is calculated by solving the impurity model. This requires an efficient and accurate impurity solver. We will use the Numerical Renormalization Group for this step.
4. With the new local self-energy we continue with step 1.

This iterative procedure is repeated until the self-energy changes by less than some given precision ϵ.

2.6. DMFT on the Bethe lattice

In this work the Bethe lattice in the limit of infinite dimensions will be used for DMFT calculations. In z dimensions the Bethe lattice is a graph where each lattice site has z nearest neighbors without containing cycles.

The specific type of the lattice only enters DMFT via the non interacting density of states in equation (2.18), $\rho_0(\varepsilon)$. For the Bethe lattice in infinite dimensions, $\rho_0(\varepsilon)$ has a semi-elliptic form (see appendix D of [13]):

$$\rho_0(\varepsilon) = \frac{2}{\pi D}\sqrt{1 - \left(\frac{\varepsilon}{D}\right)^2} \tag{2.26}$$

with $\varepsilon \in [-D, D]$ and half bandwidth D.

The lattice Green's function is obtained by solving the integral

$$\langle\langle c_i, c_i^\dagger \rangle\rangle_\omega = \int_{-\infty}^{\infty} d\varepsilon \quad \frac{\rho_0(\varepsilon)}{\xi - \varepsilon} \tag{2.27}$$

where $\xi = \omega - \Sigma_{latt}(\omega) + \mu$ and is thus formally the Hilbert transform of $\rho_0(\varepsilon)$. When evaluating this integral for $\rho_0(\varepsilon)$ given in equation (2.26), we get

$$\langle\langle c_i, c_i^\dagger \rangle\rangle_\omega = \frac{2}{D^2}\left(\xi - \sqrt{\xi^2 - D^2}\right), \tag{2.28}$$

yielding an expression for ξ:

$$\xi = \frac{D^2}{4} \langle\langle c_i, c_i^\dagger \rangle\rangle_\omega + \langle\langle c_i, c_i^\dagger \rangle\rangle_\omega^{-1} \tag{2.29}$$

This can now be inserted into the DMFT self-consistency equation (2.25) which results in an expression for $\Delta(\omega)$ respectively $\Gamma(\omega)$:

$$\Delta(\omega) = \left(\frac{D}{2}\right)^2 \langle\langle c_i, c_i^\dagger \rangle\rangle_\omega - \varepsilon_d \tag{2.30}$$

$$\Gamma(\omega) = \pi \left(\frac{D}{2}\right)^2 A_{i,i}(\omega) \tag{2.31}$$

with the local spectral function $A_{i,i}(\omega) = -\frac{1}{\pi} Im(\langle\langle c_i, c_i^\dagger \rangle\rangle_\omega)$.

3. Numerical Renormalization Group (NRG)

The Numerical Renormalization Group is a non perturbative way to solve quantum impurity models, where an impurity with a small amount of degrees of freedom couples to a non-interacting bath with $\to \infty$ degrees of freedom. It was first introduced by K.G. Wilson in [18] to solve the Kondo model. A detailed review of the NRG method and its applications is given in [3].

3.1. Hamiltonian

The dimension of the impurity Hamiltonian is low enough to be diagonalized exactly. We choose an arbitrary impurity basis $\{|i\rangle\}$ and corresponding annihilation (creation) operators $d_i^{(\dagger)}$.
As the bath is non-interacting, the many-particle states are just product states of the single-particle states and therefore the bath can also be diagonalized exactly with eigenstates $|k,\nu\rangle$ and corresponding annihilation (creation) operators $c_{k,\nu}^{(\dagger)}$ and eigenenergies $\varepsilon_{k,\nu} \in [D_\nu^-, D_\nu^+]$. The chemical potential μ must be in $[D_\nu^-, D_\nu^+]$ and will be set to 0.
The impurity and bath states couple with hopping amplitudes $V_k^{\nu,i}$ so that we get the following Hamiltonian:

$$\begin{aligned} H &= H_{imp} + H_{hyb} + H_{bath} \\ &= H_{imp} + \sum_{\nu,i} \sum_{k \in 1.BZ} V_k^{\nu,i} \Big(d_i^\dagger c_{k,\nu} + c_{k,\nu}^\dagger d_i \Big) \quad + \sum_{\nu} \sum_{k \in 1.BZ} \varepsilon_{k,\nu} c_{k,\nu}^\dagger c_{k,\nu} \end{aligned} \tag{3.1}$$

$\nu = (m_{bath}, \sigma)$ and $i = (m_{imp}, \sigma)$ are composite indices of bath/impurity orbital number $m_{bath/imp} \in \{1, \dots, N_c^{bath/imp}\}$ and spin $\sigma \in \{\uparrow, \downarrow\}$, similar to ν in section 2.2.
Note that for the application of NRG as an impurity solver for DMFT, $N_c^{imp} = N_c^{bath} \equiv N_c$. Therefore m_{bath} is equivalent to $m_{imp} \equiv m$ and i equivalent to ν. This means that within DMFT, following section 2.2, $V_k^{\nu,i} = 0$ if $\nu = (m, \sigma) \neq (m', \sigma') = i$, thus $V_k^{\nu,i} \equiv V_k^\nu$ as in equation (2.10).

3.2. General Procedure

The Hamiltonian of the impurity model can in general not be solved exactly, as the impurity Hamiltonian may contain arbitrary interactions and the bath Hamiltonian adds $\to \infty$ degrees of freedom to that. In order to get an approximate solution, the bath is discretized to lower its dimension. For that a logarithmic discretization is used so that the resolution for low energy excitations is exponentially enhanced. With some approximations to the bath, but not the hybridization and the impurity, the Hamiltonian is then mapped on a semi-infinite chain with exponentially decaying couplings and diagonalized iteratively. The whole procedure from discretization to the mapping on a tight-binding-chain is described in more detail in appendix D.

3.3. Discretization of the bath

To discretize the bath, a discretization parameter $\Lambda > 1$ is chosen. With $D_\nu = min\{|D_\nu^-|, |D_\nu^+|\}$, the energy axis of each band ν in respect to its hybridization with impurity state i is discretized resulting in energy intervals $I^\lambda_{n,\nu,i}$ with $\lambda = \pm$, $n \in \mathbb{N}$ and a shift parameter $z_{\nu,i} \in [0, 1)$:

$$\begin{aligned} I^+_{n,\nu,i} &= (D_\nu \Lambda^{-1-z_{\nu,i}}, D_\nu^+] & I^+_{n,\nu,i} &= (D_\nu \Lambda^{-n-z_{\nu,i}}, D_\nu \Lambda^{-n+1-z_{\nu,i}}] \\ I^-_{n,\nu,i} &= [D_\nu^-, -D_\nu \Lambda^{-1-z_{\nu,i}}) & I^-_{n,\nu,i} &= [-D_\nu \Lambda^{-n+1-z_{\nu,i}}, -D_\nu \Lambda^{-n-z_{\nu,i}}) \end{aligned} \tag{3.2}$$

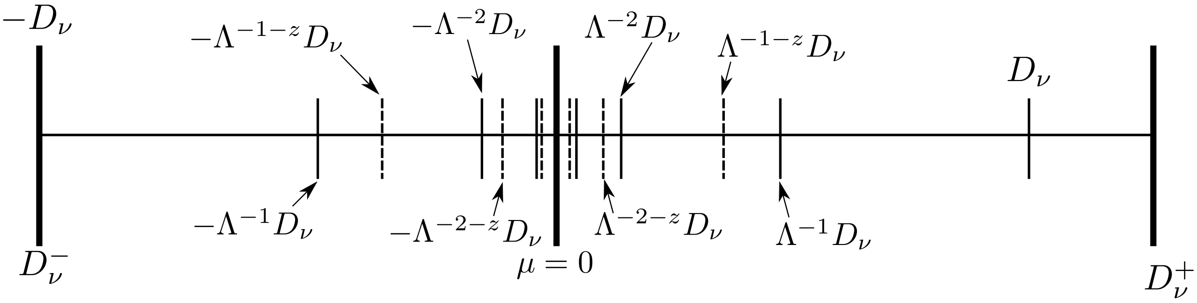

Figure 3.1.: Logarithmic discretization of band ν, $min\{|D_\nu^-|, |D_\nu^+|\} = |D_\nu^-| = D_\nu$. The solid lines correspond to a discretization with $z = 0$, the dashed ones to $z > 0$.

The length of those intervals (apart from the $n = 1$ ones) is $D_\nu \Lambda^{-n-z_{\nu,i}}(\Lambda - 1) \sim \Lambda^{-n}$ which gives exponentially enhanced resolution near the chemical potential. $z_{\nu,i}$ allows to shift the discretization grid points. This so called z-shifting can be used to increase the precision of the NRG results by averaging over the results of several NRG calculations with different $z_{\nu,i}$. Usually, $z_{\nu,i} \equiv z$ is chosen the same for each pair (ν, i), but this is not mandatory which will be exploited within the framework of the interleaved NRG method, discussed in chapter 4.

In the calculations for this thesis, we perform up to $n_z = 8$ z-shift. For the calculations with the standard NRG method discussed in this chapter the same shift parameter $z_{\nu,i} \equiv z$ is used for all pairs $z_{\nu,i}$ and shifted uniformly over the interval $[0, 1)$:

$$z \in \left\{0, \frac{1}{n_z}, \frac{2}{n_z}, \ldots, \frac{n_z - 1}{n_z}\right\} \quad , \tag{3.3}$$

where n_z is the number of different shift parameters. Z-shifting within the interleaved NRG is discussed in section 4.2.

3.4. Mapping on semi-infinite tight binding chain

In the next step, an orthogonal transformation is constructed so that in each interval exactly one states couples directly to the impurity. All bath states but those that couple directly to the impurity will be neglected for the further procedure. For the Hamiltonian we now get

$$H^{star} = H_{imp} + \sum_{n,\lambda} \sum_{\nu,i} \xi_{i,\nu}^{n,\lambda} (a_i^{n,\lambda,\nu})^\dagger a_i^{n,\lambda,\nu} + \sum_{n,\lambda} \sum_{\nu,i} \gamma_{n,\lambda}^{\nu,i} \Big(d_i^\dagger a_i^{n,\lambda,\nu} + h.c. \Big) \quad , \tag{3.4}$$

where $\sum_{n,\lambda}$ is the sum over the intervals described in the previous section and $\sum_{\nu,i}$ is the sum over all impurity states and all bands. The operators $(a_i^{n,\lambda,\nu})^{(\dagger)}$ annihilate (create) the directly coupling bath states with energies $\xi_{i,\nu}^{n,\lambda}$ and coupling $\gamma_{n,\lambda}^{\nu,i}$. These couplings and energies are obtained from an orthogonal transformation, described in appendix D. In this thesis a different approach for the calculations of the representative energies $\xi_{i,\nu}^{n,\lambda}$ was used. This approach uses a differential equation to calculate the representative energies, which is obtained by insisting to reproduce the continuous bath density of states in the limit of an infinite amount of z-shifts. For more details see [20] and [19]. Due to its form, the Hamiltonian of equation (3.4) is ofthen referred to as the star Hamiltonian:

$$H^{star} = H_{imp} + \sum_{\nu,i} H_{\nu,i}^{star}$$

$$H_{\nu,i}^{star} = \begin{pmatrix}
\ddots & & & \vdots & \vdots & \vdots & & & \\
& \xi_{i,\nu}^{n,-} & & \vdots & \gamma_{n,-}^{\nu,i} & \vdots & & & \\
& & \ddots & 0 & \vdots & \vdots & & & \\
\cdots & 0 & \cdots & \xi_{i,\nu}^{1,-} & \gamma_{1,-}^{\nu,i} & 0 & \cdots & 0 & \cdots \\
\cdots & \gamma_{n,-}^{\nu,i} & \cdots & \gamma_{1,-}^{\nu,i} & 0 & \gamma_{1,+}^{\nu,i} & \cdots & \gamma_{n,+}^{\nu,i} & \cdots \\
\cdots & 0 & \cdots & 0 & \gamma_{1,+}^{\nu,i} & \xi_{i,\nu}^{1,+} & \cdots & 0 & \cdots \\
& & & 0 & \vdots & 0 & \ddots & & \\
& & & \vdots & \gamma_{n,+}^{\nu,i} & \vdots & & \xi_{i,\nu}^{n,+} & \\
& & & \vdots & \vdots & \vdots & & & \ddots
\end{pmatrix}$$

The Matrix elements $\gamma_{n,\lambda}^{\nu,i}$ are scaling like $\sim \Lambda^{-\frac{n}{2}}$ and $\xi_{i,\nu}^{n,\lambda}$ like $\sim \Lambda^{-n}$ due to the decreasing length of the intervals $I_n^\lambda \sim \Lambda^{-n}$ with increasing n. Each of the $H_{\nu,i}^{star}$ can be brought into a tridiagonal form via a second orthogonal transformation

$$H^{chain}_{\nu,i} = \begin{pmatrix} 0 & t_0^{\nu,i} & 0 & \cdots & \cdots & \\ t_0^{\nu,i} & \epsilon_0^{i,\nu} & \ddots & & & \\ 0 & \ddots & \ddots & t_n^{\nu,i} & & \\ \vdots & & t_n^{\nu,i} & \epsilon_n^{i,\nu} & \ddots & \\ \vdots & & & \ddots & \ddots & \ddots \end{pmatrix}$$

$$H^{chain}_{\nu,i} = t_0^{\nu,i}(d_i^\dagger f_0^{\nu,i} + h.c.) + \sum_{n=1}^{\infty} t_n^{\nu,i}((f_n^{\nu,i})^\dagger f_{n-1}^{\nu,i} + h.c.) + \sum_{n=0}^{\infty} \epsilon_n^{\nu,i}(f_n^{\nu,i})^\dagger f_n^{\nu,i} \tag{3.5}$$

$$H^{chain} = H_{imp} + \sum_{\nu,i} H^{chain}_{\nu,i} \tag{3.6}$$

with basis states $\{|f_n^{\nu,i}\rangle\}, n \in \mathbb{N}$ and corresponding annihilation operators $f_n^{\nu,i}$. The hopping amplitudes $t_n^{\nu,i}$ usually inherit the $\sim \Lambda^{-\frac{n}{2}}$ dependence from the $\gamma_{n,\lambda}^{\nu,i}$ while the $\epsilon_n^{\nu,i}$ usually fall off even faster, like Λ^{-n} as the $\xi_{i,\nu}^{n,\lambda}$. H^{chain} in general represents $\nu_{max} \cdot i_{max}$ semi infinite tight binding chains with exponentially decaying hopping amplitudes. These chains are also called Wilson chains. I will call H^{chain} the full Wilson chain, $H^{chain}_{\nu,i}$ a subchain, a site of a subchain a subsite and all subsites of a certain value of n a supersite.

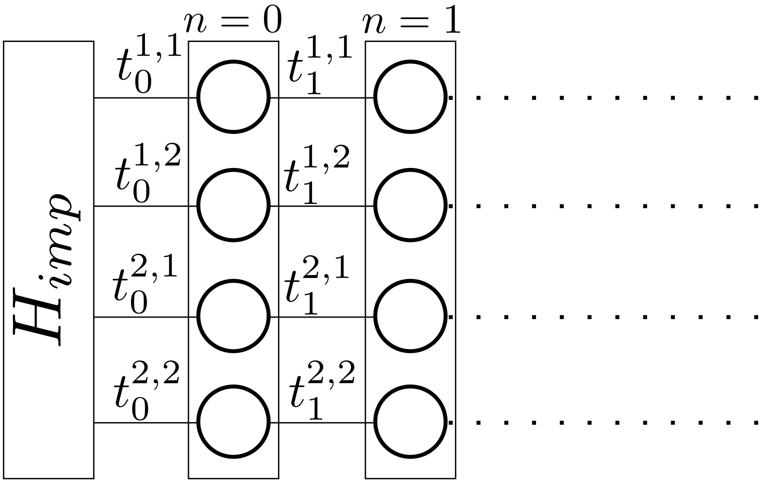

Figure 3.2.: Graphical illustration of a full Wilson chain with $\nu_{max} = 2$ and $i_{max} = 2$. The two rectangles with superscript $n = 0$ and $n = 1$ illustrate supersite 0 respectively 1. The circles within the rectangles illustrate the 4 subsites within each supersite.

It should be clarified here that usually the number of subchains is smaller than $\nu_{max} \cdot i_{max}$, as normally not every single particle impurity state i hybridizes with every bath electron type ν. An example is the use of NRG with DMFT. As already mentioned in section 3.1, only bath electrons and impurity electrons with the same orbital index m and spin index σ hybridize, yielding only $2 \cdot N_c$ subchains rather than $2 \cdot N_c \cdot 2 \cdot N_c$ subchains.

3.5. Iterative Diagonalization

The tight-binding-chain Hamiltonian in equation (3.6) now has a manageable form for approximative diagonalization which will be done by iteratively adding a supersite and diagonalizing the Hamiltonian. As the hopping amplitudes $t_n^{\nu,i}$ and the on-site energies $\epsilon_n^{\nu,i}$ decrease by $\Lambda^{-\frac{n}{2}}$ with increasing n, the n-th site is a perturbation of the order $\Lambda^{-\frac{1}{2}}$ relative to site n-1. We can terminate the Wilson chain (3.6) at the first site $n = L$ where our required energy resolution $\delta E \geq \sum_\nu D_\nu \Lambda^{-\frac{L}{2}}$. More on the required energy resolution δE will be in section 3.7. The terminated Wilson chain

$$H_{\nu,i}^L = t_0^{\nu,i}(d_i^\dagger f_1^{\nu,i} + h.c.) + \sum_{n=1}^{L} t_n^{\nu,i}((f_n^{\nu,i})^\dagger f_{n+1}^{\nu,i} + h.c.) + \sum_{n=0}^{L} \epsilon_n^{\nu,i}(f_n^{\nu,i})^\dagger f_n^{\nu,i} \tag{3.7}$$

$$H^L = H_{imp} + \sum_{\nu,i} H_{\nu,i}^L \tag{3.8}$$

is now diagonalized iteratively.

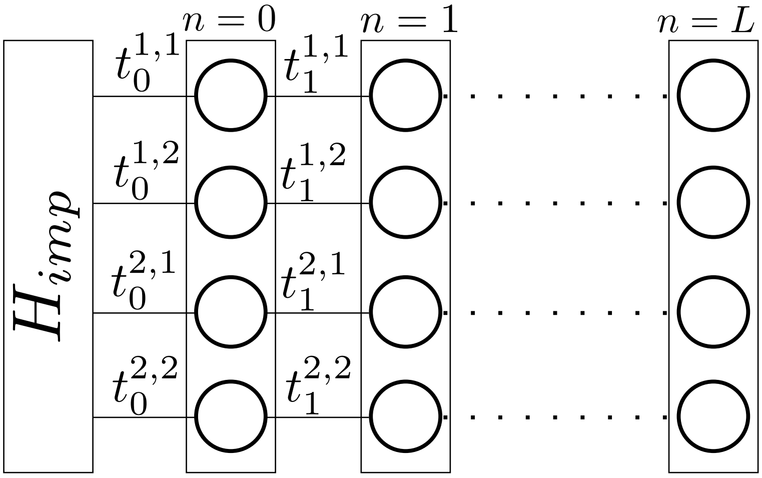

Figure 3.3.: Terminated Wilson chain corresponding to the Wilson chain in figure 3.2

When the diagonalization is performed, two problems occur:

1. Numerical matrix diagonalization has an error. As the weight of site n scales as $\Lambda^{-\frac{n}{2}}$ the relative accuracy of each site gets worse as we go down the chain up to the point where the numerical error is larger than the correction of the site.

2. The dimension of H^L is far too large to diagonalize it within an appropriate amount of time and memory. If the number of our Wilson subchains is κ, the local many-particle-basis of any supersite is 2^κ. When we take N sites into account plus the impurity with dimension d_{imp}, we get:

$$dim(H^{N-1}) = d_{imp} \cdot (2^\kappa)^N = d_{imp} \cdot 2^{N \cdot \kappa} \tag{3.9}$$

   In this section we will deal with the exponential N-dependence. The exponential κ-dependence is the point where the interleaved NRG-method, discussed in section 4, comes in.

The first problem is dealt with an iterative renormalization group procedure. For that we define the following series of Hamiltonians H^N:

$$H^N_{\nu,i} = t_0^{\nu,i}(d_i^\dagger f_1^{\nu,i} + h.c.) + \sum_{n=1}^{N} t_n^{\nu,i}((f_n^{\nu,i})^\dagger f_{n-1}^{\nu,i} + h.c.) + \sum_{n=0}^{N} \epsilon_n^{\nu,i}(f_n^{\nu,i})^\dagger f_n^{\nu,i} \tag{3.10}$$

$$H^N_{ren} = \Lambda^{\frac{N}{2}} \left[H_{imp} + \sum_{\nu,i} H^N_{\nu,i} \right] \tag{3.11}$$

The Hamiltonian H^N_{ren} contains all sites up to site N and is renormalized by a factor of $\Lambda^{\frac{N}{2}}$ to cancel out the $\Lambda^{-\frac{N}{2}}$ dependence of the energy scale of site N to ensure equal relative accuracy for every site. We get from H^N_{ren} to H^{N+1}_{ren} by rescaling H^N_{ren} with $\Lambda^{\frac{1}{2}}$ and adding supersite $N+1$, rescaled by $\Lambda^{\frac{N+1}{2}}$:

$$H^{N+1}_{ren} = \Lambda^{\frac{1}{2}} H^N_{ren} + \Lambda^{\frac{N+1}{2}} \sum_{\nu,i} \left[t_{N+1}^{\nu,i}((f_{N+1}^{\nu,i})^\dagger f_N^{\nu,i} + h.c.) + \epsilon_{N+1}^{\nu,i}(f_{N+1}^{\nu,i})^\dagger f_{N+1}^{\nu,i} \right] \tag{3.12}$$

The original Wilson-chain Hamiltonian of equation (3.6) is retrieved by taking the following limit:

$$H^{chain} = \lim_{N \to \infty} \Lambda^{-\frac{N}{2}} H^N_{ren} \tag{3.13}$$

H^L is now diagonalized iteratively by first diagonalizing H^0_{ren} and then iteratively invoking equation (3.12) after H^N_{ren} is diagonalized and carrying out the diagonalization of H^{N+1}_{ren} until H^L_{ren} is reached. The eigenenergies of H^L_{ren} are then scaled with $\Lambda^{-\frac{L}{2}}$ to get the eigenenergies of H^L, the eigenstates are of course the same.
When the iterative diagonalization procedure is carried out, the problem occurs that the dimension of the state space will become too large to handle matrix diagonalizations. This problem is tackled by a truncation scheme. For that a maximum number of kept states is defined, N_{keep}, so that $2^\kappa \cdot N_{keep}$ dimensional matrix diagonalizations can still be managed reasonably. When, at some iteration $\tilde{N}$, the dimension of $H^{\tilde{N}}_{ren}$ exceeds N_{keep}, the $dim(H^{\tilde{N}}_{ren}) - N_{keep}$ states with the largest eigenenergies will be discarded and only the N_{keep} states with the lowest eigenenergies are kept. After that equation (3.12) is invoked. As only N_{keep} states have been kept, $H^{\tilde{N}+1}_{ren}$ is only considered on a $2^\kappa \cdot N_{keep}$ dimensional space, diagonalized and the $(2^\kappa - 1) \cdot N_{keep}$ states with the largest eigenenergies are again truncated. We will call the whole set of eigenstates acquired from the

diagonalization at some iteration N $\{|s_N\rangle\}$, the states kept from that iteration are called $|s_N^K\rangle$ and the discarded ones $|s_N^D\rangle$. Values for N_{keep} vary from a few hundred for two Wilson subchains (one band DMFT calculation) to 3000-5000 for six subchains (three band DMFT calculation).
To summarize, we get the following iterative diagonalization procedure, initialized by the diagonalization of H^0_{ren}:

1. H^N_{ren} is diagonalized. $\{|s_N\rangle\}$ are the eigenstates obtained from that diagonalization with corresponding eigenenergies $E^N_{s,ren}$
2. $\{|s_N\rangle\}$ is truncated and only the up to N_{keep} eigenstates $\{|s_N^K\rangle\}$ with the lowest eigenenergies are kept. The rest of the space, $\{|s_N^D\rangle\}$ is discarded.
3. The ground state energy is set to 0. This step is not mandatory.
4. The diagonalized H^N_{ren} is rescaled by $\Lambda^{\frac{1}{2}}$.
5. $\{|s_N^K\rangle\}$ is extended by some arbitrary local basis $\{|\sigma_{N+1}\rangle\}$ of supersite N+1 to get the product basis $\{|s_N\rangle^K \otimes |\sigma_{N+1}\rangle\}$. Then the Hamiltonian of supersite N+1, rescaled by $\Lambda^{\frac{N+1}{2}}$ is added to get H^{N+1}_{ren}, represented in the product basis $\{|s_N^K\rangle \otimes |\sigma_{N+1}\rangle\}$. Step 4. and 5. essentially corresponds to equation (3.12).
6. The whole procedure is repeated until supersite L is reached.

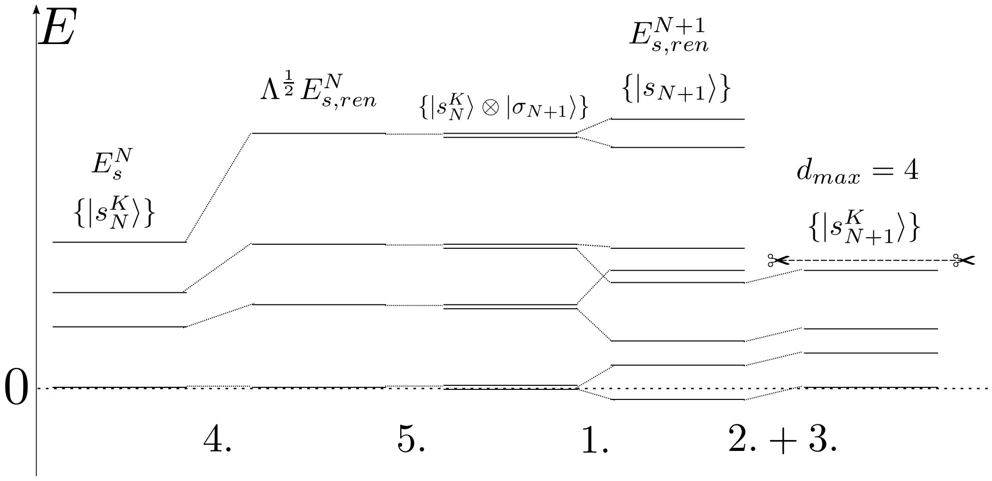

Figure 3.4.: iterative diagonalization procedure from $N \to N+1$:
The numbers indicate the steps within the enumeration above. In the illustrated case, N_{keep} is 4 and the dimension of the site-specific local basis is 2, which corresponds to a single Wilson subchain.

As this truncation scheme implies that we have to throw away almost the whole space H^L is acting on and only keep a small subspace, this procedure needs some explanation.

First of all, we are interested in a good resolution of the ground state and the first few excited states, but as the excitation energy E_{ex} from the ground state to an excited state gets larger, the state gets less important for thermodynamic calculations as it is exponentially subdued by a factor of $exp(-\frac{E_{ex}}{k_B T})$. This is one thing the introduced truncation scheme accomplishes: The lower the excitation energy, the later down the chain a state is discarded and the more exactly the state is calculated.
A more important question is how this truncation affects the outcome of the kept states. This a priori not completely clear, but can by justified by a perturbation theoretical argument. The additional term occurring when going from H^N to H^{N+1} is essentially a perturbation V of order $\sum_\nu D_\nu \Lambda^{-\frac{1}{2}} \sim \Lambda^{-\frac{1}{2}}$. In first order the correction of a given states $|\tilde{s}_N\rangle$ we get

$$|\tilde{s}_N\rangle_1 = \sum_{s,s\neq\tilde{s}} |s_N\rangle \frac{\langle s_N| V |\tilde{s}_N\rangle}{E^N_{\tilde{s},ren} - E^N_{s,ren}} \quad , \tag{3.14}$$

which means if $|\langle s_N|V|\tilde{s}_N\rangle| \sim \sum_\nu D_\nu \Lambda^{-\frac{1}{2}} << |E^N_{\tilde{s},ren} - E^N_{s,ren}|$ the correction to the state $|\tilde{s}_N\rangle$ can be neglected. This implies that we have to set N_{keep} sufficiently large so that the neglected corrections for the ground state are of an acceptable order. The outcome of the excited states is of course worse the larger their eigenenergies are. An other important thing to note is that one has to increase N_{keep} if one decreases Λ or otherwise the results might change for the worse.
With previously given arguments it seems more practical to set a certain maximum energy up to which all states are kept rather than defining a maximum dimension N_{keep}. We will do this by defining a characteristic energy scale for site N,

$$\omega_N = E_0 \Lambda^{-\frac{N}{2}} \quad , \tag{3.15}$$

with E_0 so that in the limit $N \to \infty$, $\frac{\sum_{\nu,i} t_N^{\nu,i}}{\omega_N} \to 1$. The rescaled truncation energy E_{trunc}, up to which the states are kept, is then given in terms of E_0. Common values for E_{trunc} vary from about $9 \cdot E_0$ for one band calculations to $7.5 \cdot E_0$ for three band calculations. Of course the number of states kept at each iteration varies when working with a fixed E_{trunc} rather than a fixed N_{keep}.
It is not clear how well the NRG results are for a given E_{trunc} or N_{keep}, but there exists a quantitative criterion called discarded weight that determines the quality of the result. Acceptable values for this quantity are $< 10^{-5}$. For more information on discarded weight see [15] and [11].

3.6. Matrix product states and symmetries

In this section I want to show that the states obtained by the NRG-procedure can be written as so called matrix product states (MPS). A comprehensive introduction to MPS can be found in [10].
When we perform one step of the iterative diagonalization procedure from $N \to N+1$, we express the eigenstates $|s_{N+1}\rangle$ of H^{N+1} as linear combinations of the product basis

$\{|s_N^K\rangle \otimes |\sigma_{N+1}\rangle\}$. With scalar coefficients $A_{\sigma_{N+1},s_N^K,s_{N+1}} = A^{\sigma_{N+1}}_{s_N^K,s_{N+1}}$, we get the following expression:

$$\begin{aligned} |s_{N+1}\rangle &= \sum_{\sigma_{N+1},s_N^K} A_{\sigma_{N+1},s_N^K,s_{N+1}} |s_N^K\rangle \otimes |\sigma_{N+1}\rangle \\ &= \sum_{\sigma_{N+1},s_N^K} A^{\sigma_{N+1}}_{s_N^K,s_{N+1}} |s_N^K\rangle \otimes |\sigma_{N+1}\rangle \end{aligned} \tag{3.16}$$

The coefficients $A^{\sigma_{N+1}}_{s_N^K,s_{N+1}}$ can be interpreted as matrix elements of matrices $A^{\sigma_{N+1}}$, one for each local basis state $|\sigma_{N+1}\rangle$. As we usually have to discard some of the states as discussed in section 3.5, the space spanned by $\{|s_{N+1}\rangle\}$ splits into a kept subspace spanned by $\{|s_{N+1}^K\rangle\}$ with coefficients $A^{\sigma_{N+1}}_{s_N^K,s_{N+1}^K}$ and a discarded one spanned by $\{|s_{N+1}^D\rangle\}$ with coefficients $A^{\sigma_{N+1}}_{s_N^K,s_{N+1}^D}$. If we order the columns of $A^{\sigma_{N+1}}$ in a way that the first N_{keep} columns are corresponding to $A^{\sigma_{N+1}}_{s_N^K,s_{N+1}^K}$ and the rest to $A^{\sigma_{N+1}}_{s_N^K,s_{N+1}^D}$, the matrix can be split into a matrix $A_K^{\sigma_{N+1}}$ with elements $A^{\sigma_{N+1}}_{s_N^K,s_{N+1}^K}$ and a second matrix $A_D^{\sigma_{N+1}}$ with elements $A^{\sigma_{N+1}}_{s_N^K,s_{N+1}^D}$. For the kept and discarded states we then get:

$$\begin{aligned} |s_{N+1}^K\rangle &= \sum_{\sigma_{N+1},s_N^K} A^{\sigma_{N+1}}_{s_N^K,s_{N+1}^K} |s_N^K\rangle \otimes |\sigma_{N+1}\rangle \\ &= \sum_{\sigma_{N+1},s_N^K} (A_K^{\sigma_{N+1}})_{s_N^K,s_{N+1}^K} |s_N^K\rangle \otimes |\sigma_{N+1}\rangle \end{aligned} \tag{3.17}$$

$$\begin{aligned} |s_{N+1}^D\rangle &= \sum_{\sigma_{N+1},s_N^K} A^{\sigma_{N+1}}_{s_N^K,s_{N+1}^D} |s_N^K\rangle \otimes |\sigma_{N+1}\rangle \\ &= \sum_{\sigma_{N+1},s_N^K} (A_D^{\sigma_{N+1}})_{s_N^K,s_{N+1}^D} |s_N^K\rangle \otimes |\sigma_{N+1}\rangle \end{aligned} \tag{3.18}$$

If we express the $|s_N^K\rangle$ states as linear combinations of$\{|s_{N-1}^K\rangle \otimes |\sigma_N\rangle\}$ and so on, we can express $|s_{N+1}\rangle$ in the product basis $\{|\sigma_{imp}\rangle \otimes |\sigma_0\rangle \otimes \cdots \otimes |\sigma_{N+1}\rangle\}$ of the site-specific basis:

$$\begin{aligned} |s_{N+1}^X\rangle &= \sum_{\substack{\sigma_{N+1}\ldots\sigma_0 \\ \sigma_{imp}}} \sum_{s_0^K\ldots s_N^K} A^{\sigma_0}_{\sigma_{imp},s_0^K} \cdots A^{\sigma_{N+1}}_{s_N^K,s_{N+1}^X} |\sigma_{imp}\rangle \otimes |\sigma_0\rangle \otimes \cdots \otimes |\sigma_{N+1}\rangle \\ &= \sum_{\substack{\sigma_{N+1}\ldots\sigma_0 \\ \sigma_{imp}}} (A_K^{\sigma_0} \cdots A_K^{\sigma_N} A_X^{\sigma_{N+1}})_{\sigma_{imp},s_{N+1}^X} |\sigma_{imp}\rangle \otimes \cdots \otimes |\sigma_{N+1}\rangle \end{aligned} \tag{3.19}$$

In this equation X is a placeholder for either K or D. The advantage of the MPS-formalism is that the matrices contain all the site-specific information about $|s_{N+1}\rangle^X$ and are an elegant way to keep track of all the kept and discarded states.

According to [16], MPS are also quite suitable for the implementation of abelian and especially non-abelian symmetries. The QSpace formulation described in [16] has been implemented by A. Weichselbaum and was used for the NRG calculations performed for this thesis.

3.7. Approximate complete eigenbasis and full density matrix

As stated in [17] it is possible within NRG to calculate a full, approximate eigenbasis of the Hamiltonian H^L from all the discarded states and the states obtained from the last diagonalization at site L. For that we define states

$$|e_N\rangle = \bigotimes_{n=N+1}^{L} |\sigma_n\rangle \tag{3.20}$$

from the local basis states $|\sigma_n\rangle$ of sites n. We now take the discarded states from site N and extend them with the $|e_N\rangle$,

$$|se_N^D\rangle = |s_N^D\rangle \otimes |e_N\rangle \tag{3.21}$$

, so that their dimension is the same as that of H^L. We also count all states obtained from the diagonalization of site L as discarded.
By construction, the states $|se_N^D\rangle$ are orthonormal, which follows from the orthonormality of the states $|s_N^X\rangle$ obtained from diagonalizing site N and the orthonormality of the $|e_N\rangle$. The states $\{|se_N^D\rangle\}$ also form a complete basis of the space H^L is acting on. This can be seen by simply counting the amount of states $|se_N^D\rangle$ we get.
These states are also approximate eigenstates of H^L,

$$H^L\,|se_N^D\rangle \simeq E_s^N\,|se_N^D\rangle \quad , \tag{3.22}$$

with non-rescaled eigenenergies E_s^N obtained from the diagonalization at site N for state $|s_N^D\rangle$ and are $(2^\kappa)^{(L-N)}$-fold degenerate, with κ being the number of Wilson chains as in section 3.5. With an approximate eigenbasis and corresponding eigenenergies, the full density matrix (FDM) can be constructed:

$$\rho \simeq \sum_{\{|se_N^D\rangle\}} |se_N^D\rangle\,\frac{e^{-\beta E_s^N}}{Z}\,\langle se_N^D| = \sum_N w_N \rho_{DD}^N \tag{3.23}$$

with normalization Z so that $Tr(\rho) = 1$ and $\beta = \frac{1}{k_B T}$. ρ_{DD}^N is the density matrix of the discarded states of site N,

$$\rho_{DD}^N = \sum_{\substack{\{|s_N^D\rangle\}\\ N=const}} |s_N^D\rangle\,\frac{e^{-\beta E_s^N}}{Z_N}\,\langle s_N^D| \quad , \tag{3.24}$$

where $Z_N = Tr(\rho_{DD}^N)_{|s_D^N\rangle}$. The weights $w_N = \frac{(2^\kappa)^{L-N} Z_N}{Z}$ select the shells relevant thermodynamic calculations. They peaked at about the Wilson chain site with characteristic energy $\lesssim k_B T$ with a width of about 5 to 10 shells, effectively terminating the Wilson chain when w_N becomes small enough.

3.8. Calculation of spectral functions

The complete basis obtained in the previous section can also be used to calculate spectral functions. For that we insert our approximate basis with the corresponding eigenenergies into the Lehman representation,

$$A_{B,C}(\omega) = \sum_{n,m} \langle n|\, C \,|m\rangle \, \frac{e^{-\beta E_m}}{Z} \, \langle m|\, B \,|n\rangle \, \delta(\omega - (E_n - E_m)) \quad , \tag{3.25}$$

with Z the norm of the density matrix, $Z = \sum_m e^{-\beta E_m}$. We then get a sequence of δ-peaks,

$$A_{\mathrm{raw}}(\omega) = \sum_j a_j \delta(\omega - \omega_j) \quad , \tag{3.26}$$

which have to be broadened to get a continuous spectral function. The broadening is done with a broadening kernel $K(\omega, \omega')$,

$$A(\omega) = \int d\omega' K(\omega, \omega') A_{\mathrm{raw}}(\omega), \tag{3.27}$$

with a log-Gaussian broadening kernel

$$K(\omega, \omega') = \frac{\Theta(\omega, \omega')}{\sqrt{\pi}\sigma|\omega|} e^{-\left(\frac{log(|\omega/\omega'|)}{\sigma} - \frac{\sigma}{4}\right)^2} \tag{3.28}$$

which is transitioned to a regular Gaussian below ω_0. In this thesis ω_0 will be set to $10 \cdot T$, with temperature T. The broadening parameter σ is dependent on the amount of z-shifts performed and on Λ. More on the calculation and broadening of spectral functions can be read in [13], p. 34-35, and with a lot of details in [17].

4. Interleaved Numerical Renormalization Group

The interleaved Numerical Renormalization Group (iNRG) method is a slightly altered form of the standard NRG (sNRG) method discussed in section 3. It approaches the problem that the dimension of the Hamiltonian is scaling exponentially with the number of Wilson subchains κ, shown in equation (3.9).

4.1. Basic concept

The basic concept of iNRG is to use the shift parameters $z_{\nu,i}$ to generate an energy scale separation between subsites of the Wilson chain supersites, allowing truncation between those subsites rather than only whole supersites. This effectively lowers the dimension of the local basis, leading to faster matrix diagonalizations.
We start with the couplings $t_n^{\nu,i}$ introduced in equation (3.6). According to [8] and [11], these couplings decay exponentially with n and $z_{\nu,i}$ as follows:

$$t_n^{\nu,i} \sim D_\nu \Lambda^{-z_{\nu,i}-\frac{n}{2}} \quad , \tag{4.1}$$

with D_ν, Λ, n and $z_{\nu,i}$ as defined in section 3.3. This scaling is now used to create an energy scale separation between subsites $(\tilde{\nu},\tilde{i})$ and (ν,i) within the same supersite n,

$$\frac{t_n^{\tilde{\nu},\tilde{i}}}{t_n^{\nu,i}} \sim \frac{D_{\tilde{\nu}}}{D_\nu} \Lambda^{-z_{\tilde{\nu},\tilde{i}}+z_{\nu,i}} \tag{4.2}$$

As noted in [8], a natural energy scale separation occurs for different band widths D_ν without using different shift parameters $z_{\nu,i}$. For the following discussion $D_{\tilde{\nu}} = D_\nu$ will be assumed and energy scale separation will be generated solely via the $z_{\nu,i}$. We assume that we want to divide each supersite into M_{iNRG} smaller sites, called iNRG sites, and enumerate those smaller sites with an index $\alpha \in \{1, \dots, M_{iNRG}\}$. For each of those iNRG sites we use a different shift parameter z_α so that

$$\begin{aligned} \frac{t_{n,\alpha+1}^{\nu,i}}{t_{n,\alpha}^{\tilde{\nu},\tilde{i}}} &\sim \Lambda^{z_{\alpha+1}-z_\alpha} \equiv \tilde{\Lambda}^{-\frac{1}{2}} \\ \frac{t_{n,\alpha+M_{iNRG}}^{\nu,i}}{t_{n,\alpha}^{\tilde{\nu},\tilde{i}}} &= \frac{t_{n+1,\alpha}^{\nu,i}}{t_{n,\alpha}^{\tilde{\nu},\tilde{i}}} \sim \Lambda^{-\frac{1}{2}} \quad , \end{aligned} \tag{4.3}$$

where the index α labels to which iNRG site $t_n^{\ni,i} \equiv t_{n,\alpha}^{\ni,i}$ belongs. This implies that $z_{\alpha+1} - z_\alpha = \frac{1}{2M_{iNRG}}$ and $\tilde{\Lambda} = \Lambda^{\frac{1}{M_{iNRG}}}$, leading to a Wilson chain M_{iNRG} times longer

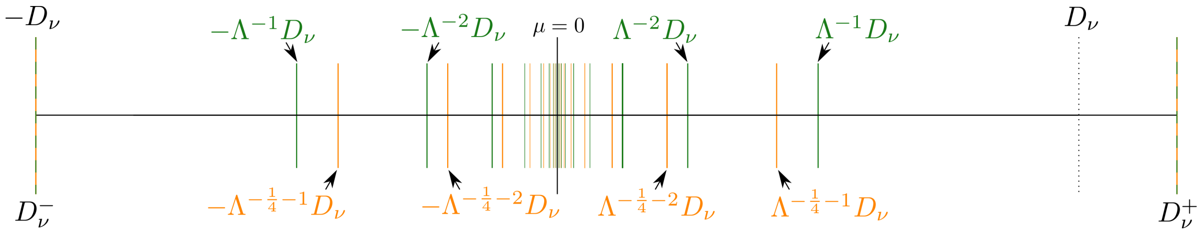
$-D_\nu$
$-\Lambda^{-1}D_\nu$
$-\Lambda^{-2}D_\nu$
$\mu = 0$
$\Lambda^{-2}D_\nu$
$\Lambda^{-1}D_\nu$
D_ν
D_ν^-
$-\Lambda^{-\frac{1}{4}-1}D_\nu$
$-\Lambda^{-\frac{1}{4}-2}D_\nu$
$\Lambda^{-\frac{1}{4}-2}D_\nu$
$\Lambda^{-\frac{1}{4}-1}D_\nu$
D_ν^+

Figure 4.1.: Discretization grid for iNRG corresponding to the grid shown in figure 3.1 without z-shift. The green lines are the grid points for $\alpha = 1$ ($z_{\alpha=1} = 0$), the orange lines for $\alpha = M_{iNRG} = 2$ ($z_{\alpha=2} = \frac{1}{4}$).

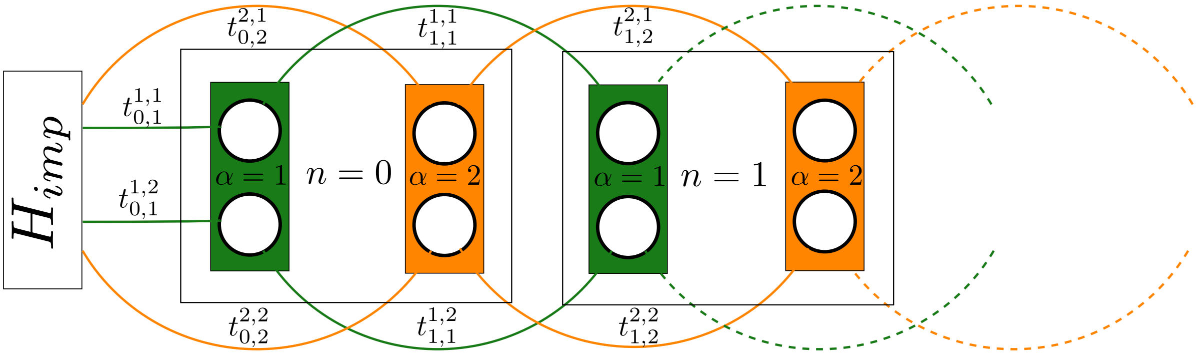
$t^{2,1}_{0,2}$
$t^{1,1}_{1,1}$
$t^{2,1}_{1,2}$
H_{imp}
$t^{1,1}_{0,1}$
$t^{1,2}_{0,1}$
$\alpha = 1$
$n = 0$
$\alpha = 2$
$\alpha = 1$
$n = 1$
$\alpha = 2$
$t^{2,2}_{0,2}$
$t^{1,2}_{1,1}$
$t^{2,2}_{1,2}$

Figure 4.2.: Interleaved Wilson chain with $M_{iNRG} = 2$, corresponding to the Wilson chain in figure 3.2. The related discretization grid is shown in figure 4.1. Associated colors show which grid points have been used for which sites. The number of subsites does not have to be the same for all α-indexed iNRG sites, i.e. one green $\alpha = 1$ subsite and three $\alpha = 2$ subsites would also be possible.

but with M_{iNRG}-th nearest neighbor hopping instead of nearest neighbor hopping and a reduced local basis, allowing faster matrix diagonalization.

As matrix diagonalizations scale with $\lesssim \dim^3$, depending on the symmetries that can be exploited, and the dimension scales exponentially with the amount of subsites, this procedure takes less computational resources. We will now estimate how many more operations sNRG takes compared to iNRG. For that we will assume that the matrix diagonalization scales with $\dim^3$ and all iNRG sites contain the same amount of subsites. The matrix dimension for sNRG is then

$$d^{\text{sNRG}} = N_{keep} \cdot 2^{\kappa} \tag{4.4}$$

while for iNRG it is

$$d^{\text{iNRG}} = N_{keep} \cdot 2^{\kappa/M_{iNRG}} \quad . \tag{4.5}$$

As we have M_{iNRG} more diagonalizations when using iNRG we get for the ratio of needed operations with iNRG, N_{op}^{iNRG} and those needed for sNRG, N_{op}^{sNRG}:

$$\frac{N_{op}^{sNRG}}{N_{op}^{iNRG}} \sim \frac{N_{keep} \cdot 2^{3\kappa}}{M_{iNRG} \cdot N_{keep} \cdot 2^{3\kappa/M_{iNRG}}} = \frac{1}{M_{iNRG}} 2^{3\kappa \cdot \frac{M_{iNRG}-1}{M_{iNRG}}} \quad , \tag{4.6}$$

scaling exponentially with κ.

For truncation we use the same energy based scheme as for sNRG (see section 3.5 and [11]). It should be noted here that the truncation energy for iNRG, E_{trunc}^{iNRG} is a little larger than the corresponding energy for sNRG, E_{trunc}^{sNRG}, to keep the same amount of states on average:

$$E_{trunc}^{iNRG} = E_{trunc}^{sNRG} \Lambda^{\frac{M_{iNRG}-1}{4 \cdot M_{iNRG}}} \tag{4.7}$$

More details on this can be found in [11].

4.2. z-averaging within iNRG

When z-shifting in iNRG calculations we split the total shift parameter $z_{\nu,i} = z_\alpha + z$ into the part that generates the energy scale separation between iNRG sites, z_α, and the parameter z that shifts the discretization points. As in section 3.3 we use the same z for all pairs (ν, i) and shift it uniformly over the interval $[0, 1)$ (see (3.3) in section 3.3):

$$z \in \left\{ 0, \frac{1}{n_z}, \frac{2}{n_z}, \dots, \frac{n_z - 1}{n_z} \right\} \quad , \tag{4.8}$$

where n_z is the number of z-shifts performed.

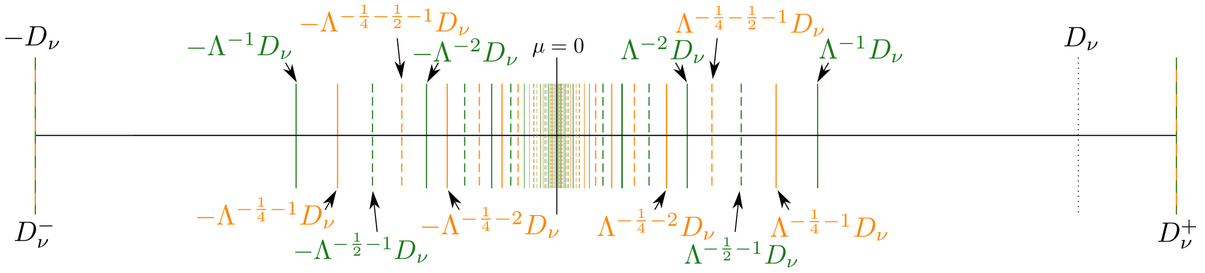
$-D_\nu$
$-\Lambda^{-1}D_\nu$
$-\Lambda^{-\frac{1}{4}-\frac{1}{2}-1}D_\nu$
$-\Lambda^{-2}D_\nu$
$\mu = 0$
$\Lambda^{-2}D_\nu$
$\Lambda^{-\frac{1}{4}-\frac{1}{2}-1}D_\nu$
$\Lambda^{-1}D_\nu$
D_ν
D_ν^-
$-\Lambda^{-\frac{1}{4}-1}D_\nu$
$-\Lambda^{-\frac{1}{2}-1}D_\nu$
$-\Lambda^{-\frac{1}{4}-2}D_\nu$
$\Lambda^{-\frac{1}{4}-2}D_\nu$
$\Lambda^{-\frac{1}{2}-1}D_\nu$
$\Lambda^{-\frac{1}{4}-1}D_\nu$
D_ν^+

Figure 4.3.: Discretization grids for iNRG with $n_z = 2$, corresponding to the grid in figure 4.1. The solid lines are associated with $z = 0$, the dashed lines with $z = \frac{1}{2}$. Colors are chosen to match those in figure 4.1 and 4.2.

For large n_z, $z_{\nu,i}$ may become > 1, for example for $n_z > 3$ and $M_{iNRG} = 2$, yielding very large first intervals and thus a very bad resolution at the band edges. A second problem is that for some values of z, the discretization points of some iNRG sites are shifted on those of other iNRG sites for a different $\tilde{z} \neq z$, essentially replicating the discretization with shift parameter $\tilde{z}$ with just larger first intervals. This happens for

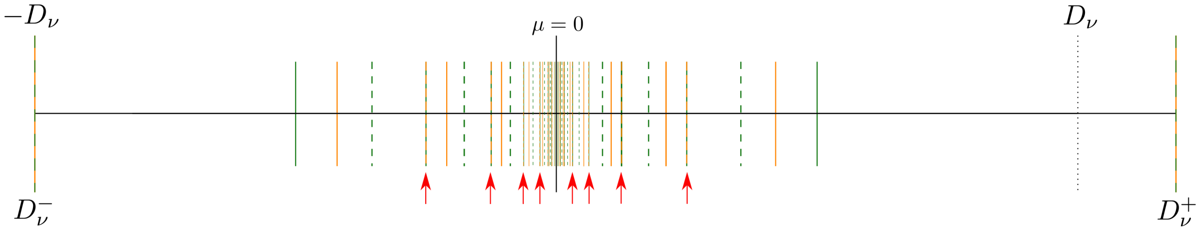

Figure 4.4.: Discretization grids for iNRG with $M_{iNRG} = 2$ and $n_z = 8$. The solid lines are grid points for $z = 0$, the dashed lines for $z = \frac{6}{8}$. The red arrows mark where the dashed orange grid ($z = \frac{6}{8}$, $z_{\alpha=2} = \frac{1}{4}$) is shifted onto the solid green grid ($z = 0$, $z_{\alpha=1} = 0$). It essentially replicates the solid green grid apart from the $n = 1$ grid points, giving it a bad resolution on the band edges. Colors are chosen as in figures 4.1 - 4.3.

example for $m = 2$ and $n_z = 8$, where the discretization of the $z_\alpha = 0$ iNRG sites and the $z_\alpha = \frac{1}{4}$ sites are shifted 7 times on each other. In section 7.2 the consequences of that are examined.

5. Using NRG as an impurity solver for DMFT

In this section the complications that arise when combining using (i)NRG as an impurity solver for DMFT will be discussed.

5.1. Self energy trick

The definition of the self energy,

$$\langle\langle [d, H^{int}]_-, d^\dagger \rangle\rangle_\omega = \Sigma(\omega) \, \langle\langle d, d^\dagger \rangle\rangle_\omega \tag{5.1}$$

with H^{int} the interaction part of the Hamiltonian, $d^{(\dagger)}$ the (creation) annihilation operators for particles in a certain state and $\Sigma(\omega)$ the self-energy corresponding to that state implies a simple way to calculate the self-energy if arbitrary Green's functions can be calculated:

$$\Sigma(\omega) = \frac{\langle\langle [d, H^{int}]_-, d^\dagger \rangle\rangle_\omega}{\langle\langle d, d^\dagger \rangle\rangle_\omega} \tag{5.2}$$

Within NRG it is possible to calculate spectral functions which are, up to a factor of $-\frac{1}{\pi}$, the imaginary parts of the corresponding Green's function. The real part of the Green's functions is then calculated via Kramers-Kronig relations and the whole complex Green's functions are then inserted into equation (5.2).

A second way to calculate the self-energy is to use the Dyson equation,

$$\Sigma(\omega) = \left(\langle\langle d, d^\dagger \rangle\rangle^0_\omega \right)^{-1} - \left(\langle\langle d, d^\dagger \rangle\rangle_\omega \right)^{-1} \tag{5.3}$$

with $\langle\langle d, d^\dagger \rangle\rangle^0_\omega$ the non-interacting Green's function, which can be calculated exactly. The reason the self-energy trick (equation (5.2)) is preferred over the Dyson equation is that in (5.2), the self-energy is expressed as a ratio of two quantities calculated with the same numerical concepts, thus avoiding systematic errors. Especially in DMFT it is crucial to avoid such systematic errors as the outcome of one iteration is the input for the next iteration and therefore the errors might increase during the DMFT self consistency procedure.

5.2. Logarithmic discretization within DMFT

When using NRG as an impurity solver for DMFT, the form and energy support of the hybridization function changes from one iteration to the next. This means that the band edges $D_\nu^{+/-}$ have to be adjusted to match the input hybridization. The problem with this is, as stated in [13] in section 4.2.1, that if $\gamma_n \ll \sqrt{\xi_n}$ a peak arises in the hopping matrix elements at a later site $\tilde{n}$, preventing truncation due to missing energy scale separation at this site. In the calculations for this thesis we use a rather heuristic method to get around this problem. We calculate the total weight of the hybridization on each side of the chemical potential by integrating over it from $-\infty$ to 0 respectively 0 to ∞. We then define $\omega_{+/-}$ in the following way:

$$\frac{\int_{\omega_{+/-}}^{\pm\infty} d\omega \Gamma(\omega)}{\int_{0}^{\pm\infty} d\omega \Gamma(\omega)} = F_{+/-} \tag{5.4}$$

With two arbitrary numbers $0 < F_{+/-} < 1$. The interval borders for the discretization are then set to $|D^{+/-}| = max\{|\omega_{+/-}|, D\}$ with the half band width of the non-interacting density of states D (see equation 2.26). In our calculations we chose $F_+ = F_- = \frac{1}{5}$. Another issue arises due to the ω dependence of the hybridization. If the hybridization varies a lot in energy regions far away from the chemical potential where the resolution of the logarithmic discretization grid is not that good, the γ_n do not fall off perfectly like $\sim \Lambda^{-\frac{n}{2}}$ for small n. Therefore the t_n also do not fall off like $\sim \Lambda^{-\frac{n}{2}}$ for the first Wilson chain sites. For some values of n, $t_n < t_{n+1}$ can be observed, casting doubt on truncation between those sites. Nevertheless the overall $\Lambda^{-\frac{n}{2}}$ dependence is adhered to and truncation is performed between all supersites for sNRG respectively all iNRG sites in iNRG calculations.

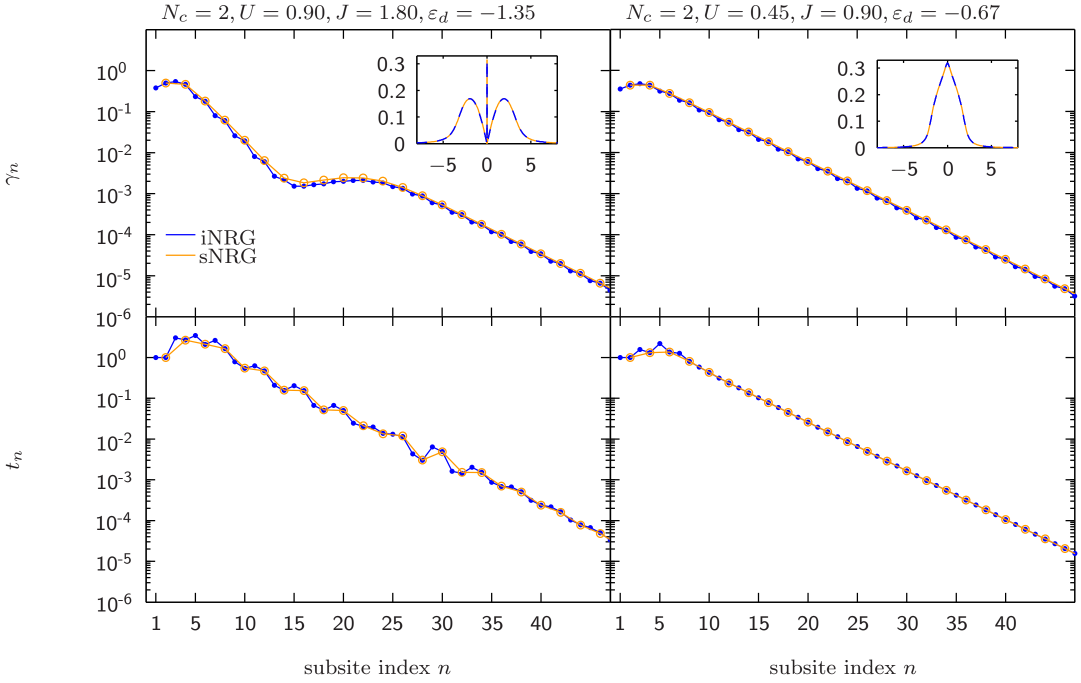

Figure 5.1.: γ_n and t_n for two different input hybridizations. The hybridization shown on the left hand side has a lot of weight far away from the chemical potential at 0. γ_n therefore shows no perfect $\sim \Lambda^{-\frac{z+n}{2}}$-dependence and t_n does not fall off perfectly like $\sim \Lambda^{-z-\frac{n}{2}}$ for up to about supersite 15. The hybridization on the right hand side on the other hand shows a lot of weight near the chemical potential, producing γ_n that fall off like $\sim \Lambda^{-\frac{z+n}{2}}$ almost immediately and therefore also the t_n perfectly fall off like $\sim \Lambda^{-z-\frac{n}{2}}$ after only 3 supersites.

6. Anderson-Hund model (AHM)

In this work I will use the Anderson-Hund model. This tight binding model, as defined in [12], exhibits on site Coulomb repulsion and Hund's rule coupling:

$$H = \sum_{\nu=1}^{N_c} \sum_{\sigma,i} (\varepsilon_{d,\nu} - \mu) n_{\nu,\sigma,i} + \sum_i H_i^{int} + \sum_{\nu=1}^{N_c} \sum_{\sigma} \sum_{\langle i,j \rangle} t_\nu d^\dagger_{\nu,\sigma,i} d_{\nu,\sigma,j} \tag{6.1}$$

$$H_i^{int} = \frac{3}{4} J N_i + \frac{1}{2}\left(U - \frac{1}{2}J\right) N_i(N_i - 1) - J\boldsymbol{S}_i^2 \tag{6.2}$$

In this Hamiltonian, $d^\dagger_{\nu,\sigma,i}$ creates electrons with spin $\sigma \in \{\uparrow, \downarrow\}$ in orbital (or channel) $\nu \in \{1, \dots N_c\}$ on site i. $n_{\nu,\sigma,i} = d^\dagger_{\nu,\sigma,i} d_{\nu,\sigma,i}$ is the corresponding number operator, $\varepsilon_{d,\nu}$ the on site binding energy of orbital ν and μ the chemical potential, which will be set to zero. The last term describes the nearest neighbor hopping with orbital specific hopping amplitude t_ν and $\sum_{\langle i,j \rangle}$ the sum over all (ordered) pairs of nearest neighbors.

H_i^{int} describes the on site electron-electron interaction of site i with total number operator

$$N_i = \sum_{\nu=1}^{N_c} \sum_{\sigma} n_{\nu,\sigma,i} \tag{6.3}$$

and total spin operator

$$\begin{aligned} \boldsymbol{S}_i &= (S_i^x, S_i^y, S_i^z) \\ S_i^\alpha &= \sum_{\nu=1}^{N_c} \sum_{\sigma,\sigma'} d^\dagger_{\nu,\sigma,i} \frac{1}{2} \sigma^\alpha_{\sigma,\sigma'} d_{\nu,\sigma',i} \end{aligned} \tag{6.4}$$

where σ^α are Pauli matrices.

$U > 0$ accounts for the Coulomb repulsion, penalizing multi occupancy while the term $-J\boldsymbol{S}_i^2$ with ferromagnetic coupling $J > 0$ accounts for Hunds second rule, favoring a large total spin per site.

Part II.

Results

7. One band Anderson Hund Model

First we will have a look on the quality of iNRG as an impurity solver for DMFT by solving the one band Anderson Hund Model (Eq. (6.1)), where corresponding sNRG calculations will be our reference. We will start with comparing two spectral functions without z-shifts, then turn to the performance of z-averaging and last but not least we will examine the one band Mott insulator transition. Comparisons will be based on the local spectral function $A(\omega)$, but Wilson chain couplings and computational efficiency will also be examined.

All models considered in this chapter will exhibit SU(2)-spin symmetry ($\varepsilon_{d,\uparrow} = \varepsilon_{d,\downarrow}$). When using iNRG we will interleave the spins ($M_{\mathrm{iNRG}} = 2$) and therefore artificially break the SU(2)-spin symmetry which should be treated with caution as symmetry breaking may lead to different fixed points. In iNRG calculations we will average over the results obtained for different spins in every DMFT iteration to use it as input for the next iteration.

The calculations presented in the following sections have all been performed on the Bethe lattice (see Sec. 2.6) and all energies are given in terms of the half-band width D of the non interacting density of states (see Eq. (2.26)). We define the energetic zero point via the chemical potential $\mu = 0$ and $\hbar$ and k_B are both set to 1. All spectral functions shown are calculated via Eq. (2.28) with the self energy obtained from the self-energy trick discussed in Sec. 5.1, Eq. (5.2). Spectral functions obtained directly from the FDM-NRG approach (see Sec. 3.8) are not shown. As a criteria for DMFT convergence we demand a maximum change of less than $5 \cdot 10^{-4}$ in the spectral functions compared to the preceding DMFT iteration. After convergence is reached, three more iterations to truly ensure convergence are performed. The DMFT procedure is initiated with a flat hybridization in the interval $\omega \in [-D, D]$ such that the result after the first DMFT iteration is metallic.

7.1. Basic results without z-shifting

Our first two calculations, shown in Fig. 7.1 and Fig. 7.3, exhibit moderate on site interactions ($U = 3, J = 1$), yielding metallic results and no z-averaging ($n_z = 1$) was applied.

For the results shown in Fig. 7.1 we choose a site specific filling $n_d = \sum_\sigma \langle d^\dagger_{i,\sigma} d_{i,\sigma} \rangle \overset{!}{=} 0.6$, with creation operators $d^\dagger_{i,\sigma}$ for electrons with spin σ on an arbitrary site i, and determine the corresponding binding energy ε_d via linear interpolation between DMFT iterations. Both iNRG and sNRG spectral functions shown in Fig. 7.1 are the final results from a converged DMFT procedure. Both iNRG and sNRG calculations took 6

DMFT iterations to reach convergence. As our considered filling is below half-filling we expect $A(\omega) \neq A(-\omega)$ with most of its weight in the $\omega > 0$ regime, which is the case as can be seen in Fig. 7.1. On a scale of $A(\omega)$ no difference between spectral functions from iNRG and sNRG calculations can be seen (left panel of Fig. 7.1, linear scale for ω), even at small frequencies, as can be seen in the right panel (logarithmic scale for ω) of Fig. 7.1. Only when $A(\omega)$ is enhanced (inset in the right panel of Fig. 7.1) relative deviations between sNRG and iNRG of order 0.01% can be seen at about $\omega \simeq 0.2$. The couplings leading to the converged DMFT results shown in Fig. 7.1 can be found in Fig. 7.2. Apart from the first three supersites (orange circles) they show the expected logarithmic decay due to their construction. In Fig. 7.2 can be seen that for iNRG sites (blue dots) 3 and 5 the Wilson chain couplings notably increase compared to sites 2 and 4, respectively, preventing truncation for these sites.

In Fig. 7.3 we show results where half-filling ($n_d = 1$) or in other terms particle-hole-symmetry was chosen. The binding energy ε_d is again adjusted by linear interpolation to reach the predetermined site-specific filling. Here it takes 8 DMFT iterations for iNRG and 9 DMFT iterations for sNRG calculations to reach convergence. As now half-filling is considered we expect $A(\omega) = A(-\omega)$ for our local spectral functions. This is the case as can be seen in the right panel of Fig. 7.3 where a logarithmic scale for ω is used. On a scale of $A(\omega)$ barely any difference between spectral functions obtained from iNRG and sNRG, respectively, can be seen, even close to $\omega \simeq 0$. When zoomed in at the quasi-particle peak at $\omega = 0$ (upper inset in the right panel of Fig. 7.3), one can observe that the iNRG spectral functions seem cut off at the top. This originates from setting positive values of the imaginary part of the retarded self-energy to 0 to ensure causality. In the lower inset in the right panel of figure Fig. 7.3 the largest difference between the spectral functions obtained from iNRG and sNRG is shown in an enhanced plot. The relative difference here is about 1.5%. The corresponding couplings leading to the converged DMFT results in Fig. 7.3 can be found in Fig. 7.4. Overall they show the expected logarithmic behavior due to their construction after about 3 supersites (orange circles). At iNRG sites (blue dots) 3, 5 and 9 we again see a considerable increase of the iNRG Wilson chain couplings compared to preceding sites which prevent truncation for these sites. Due to particle hole symmetry the Wilson site energies are zero and therefore not shown.

All in all the DMFT + iNRG results shown in Fig. 7.1 and Fig. 7.3 seem very promising due to their good match with corresponding DMFT + sNRG calculations. However, one DMFT iteration with sNRG took ~ 133 seconds on average while it took ~ 212 seconds on average for iNRG, showing that iNRG is actually computationally less efficient than sNRG in the one band case, which is rather surprising and is due to a slightly less efficient implementation.

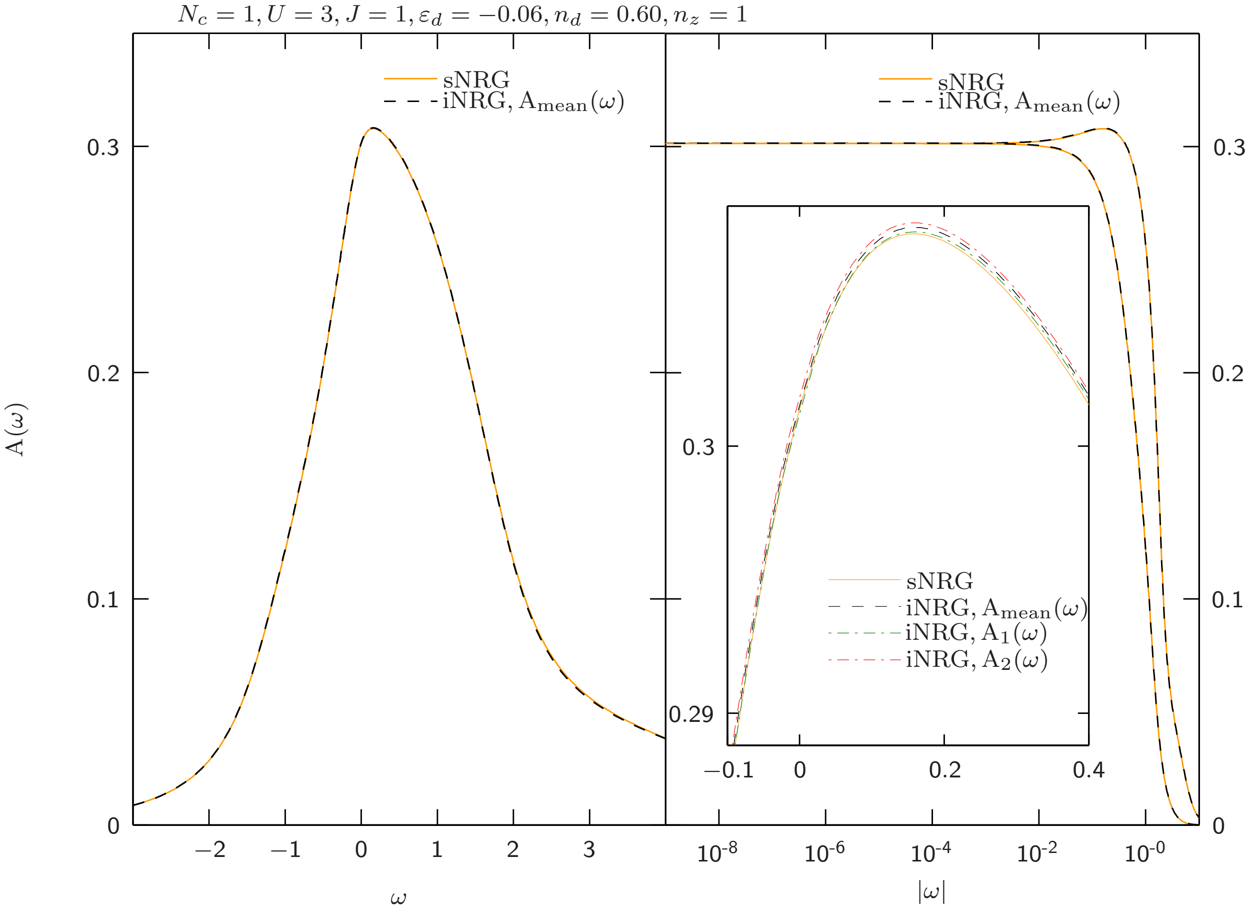

Figure 7.1.: Comparison of spectral functions for iNRG with interleaved spins ($M_{iNRG} = 2$) and sNRG for the last, converged DMFT iteration (iteration 11). The site-specific filling is chosen below half-filling ($n_d = 0.6$), the binding energy ε_d is adjusted accordingly during DMFT iterations. In this figure one can observe a perfect correspondence between sNRG and iNRG spectral functions. In the left panel a linear scale for ω has been used, as opposed to a logarithmic scale in the right panel. Small differences (maximum relative error of $5 \cdot 10^{-4}$) between iNRG and sNRG spectral functions are shown in the enhanced inset, where also spin-resolved iNRG spectral functions are shown. The couplings leading to the shown spectral functions can be found in figure Fig. 7.2. Parameters: $T = 10^{-8}$, $\Lambda = 2$, $E_{trunc} = 8$, $N_{keep}^{max} = 2500$, $\delta\rho_{\mathrm{disc}}^{\mathrm{iNRG}} = 2.87 \cdot 10^{-8}$, $\delta\rho_{\mathrm{disc}}^{\mathrm{sNRG}} = 3.25 \cdot 10^{-9}$

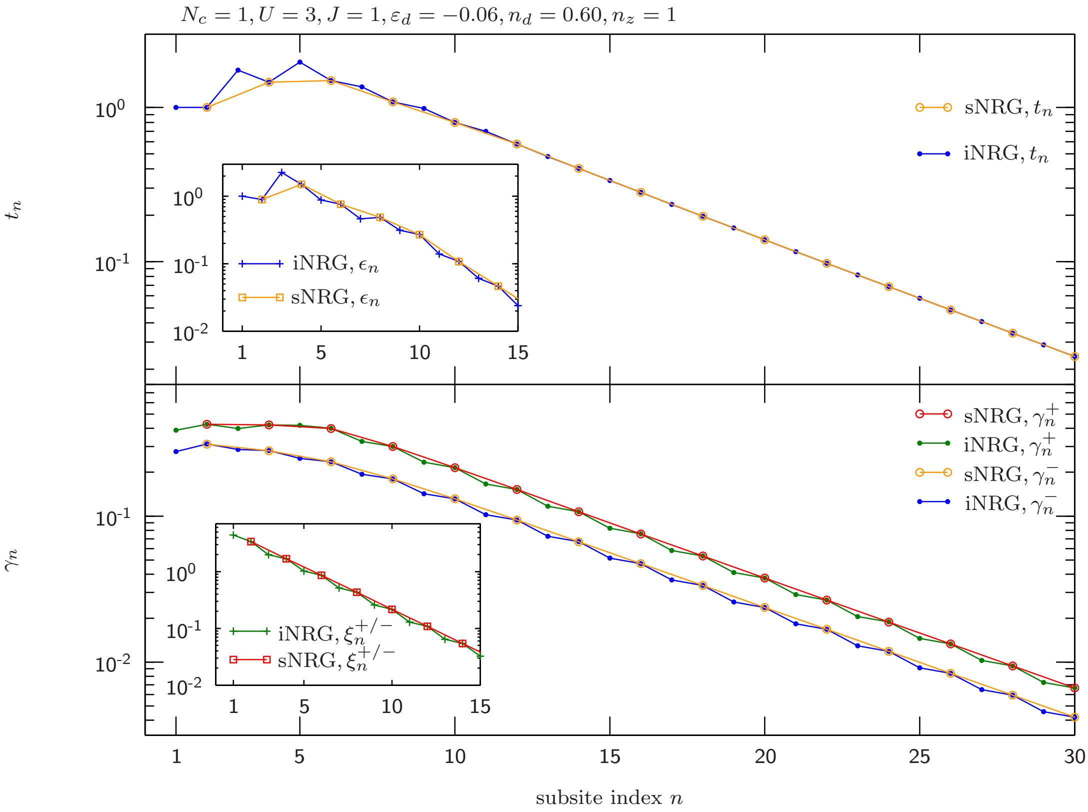

Figure 7.2.: Couplings leading to the converged results in figure 7.1. In the upper panel the Wilson chain couplings are shown, with the Wilson site energies shown in its inset. It can be observed that every second iNRG coupling (blue dots) coincides with the corresponding sNRG coupling (orange circles) due to their construction. At the first few sites a non-decaying behavior can be observed which implies that considerably large truncation energies have to be used there. The Wilson site energies ϵ_n fall off much faster than the couplings t_n and do therefore not set the bar for the energy scale of a specific site. In the lower panel the couplings for the star Hamiltonian can be seen. They fall off as expected due to their construction. The couplings for $\omega > 0$ (γ_n^+) are larger than those for $\omega < 0$ (γ_n^-) due to $A(\omega) \neq A(-\omega)$.

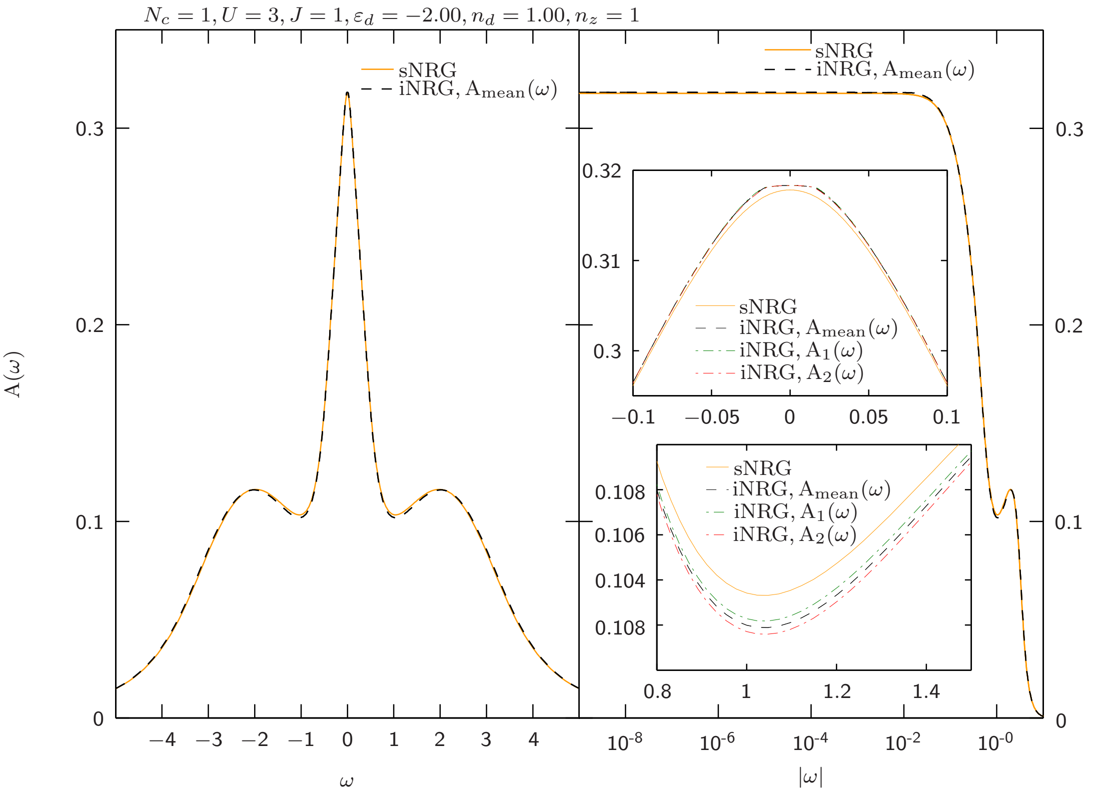

Figure 7.3.: Comparison of spectral functions for iNRG with interleaved spins ($M_{iNRG} = 2$) and sNRG for the last, converged DMFT iteration (iteration 11 for iNRG and 12 for sNRG). The site-specific filling is chosen at half-filling ($n_d = 1$), the binding energy ε_d is adjusted accordingly during DMFT iterations. In this figure one can observe a perfect correspondence between sNRG and iNRG spectral functions. In the left panel a linear scale for ω has been used, as opposed to a logarithmic scale in the right panel. Small differences (maximum relative error of $5 \cdot 10^{-4}$) between iNRG and sNRG spectral functions are shown in the enhanced insets, where also spin-resolved iNRG spectral functions are shown. The flattened tip of the iNRG spectral functions shown in the upper inset is a result of setting positive values of the imaginary part of the retarded self-energy to 0. The couplings leading to the shown spectral functions can be found in figure Fig. 7.4. Parameters: $T = 10^{-8}$, $\Lambda = 2$, $E_{trunc} = 8$, $N_{keep}^{max} = 2500$, $\delta\rho_{\text{disc}}^{\text{iNRG}} = 3.75 \cdot 10^{-8}$, $\delta\rho_{\text{disc}}^{\text{sNRG}} = 4.63 \cdot 10^{-9}$

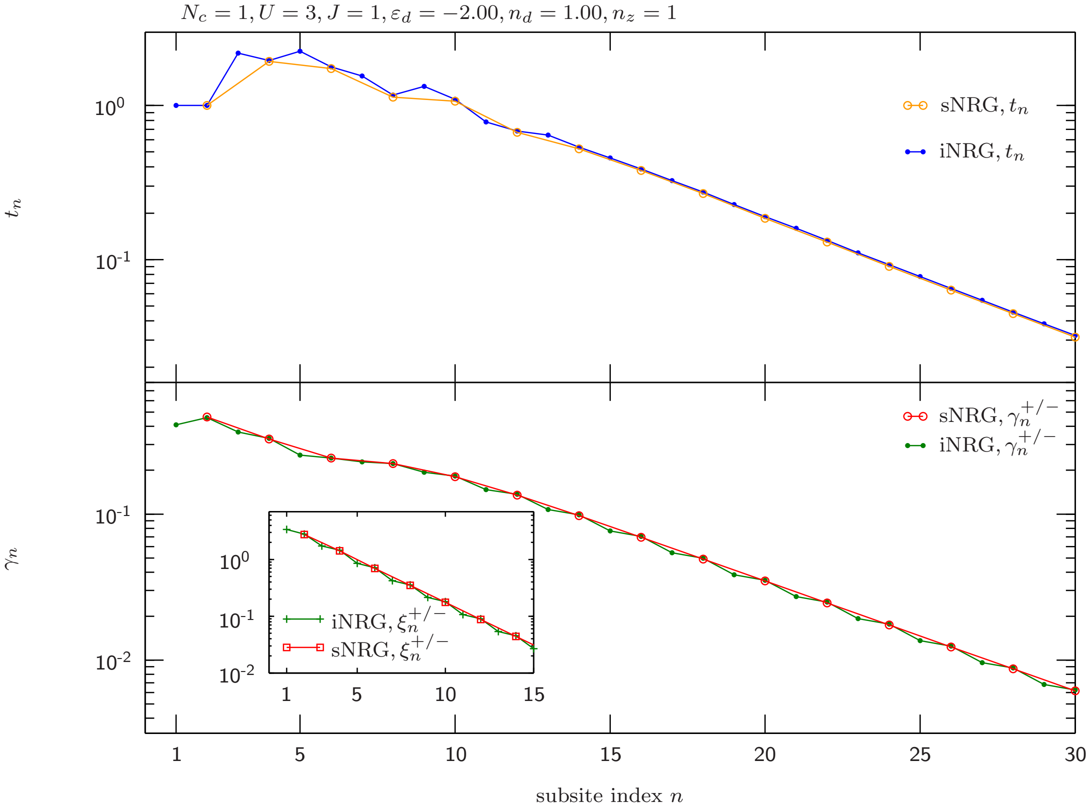

Figure 7.4.: Couplings leading to the converged results in figure 7.3. In the upper panel the Wilson chain couplings are shown. It can be observed that every second iNRG coupling (blue dots) coincides with the corresponding sNRG coupling (orange circles) due to their construction. At the first few sites a non-decaying behavior can be observed which implies that considerably large truncation energies have to be used there. The Wilson site energies ϵ_n are equal to 0 due to the SU(2)-charge-symmetry. In the lower panel the couplings for the star Hamiltonian can be seen. They fall off as expected due to their construction, despite a small bump at supersite (red circles) 3 which is caused by the frequency dependence of the input hybridization. Because of the particle-hole symmetry of our considered model $\gamma_n^+ = \gamma_n^-$.

7.2. Z-averaging for the one band model

We now use z-averaging paired with an appropriate reduction in the broadening parameter σ for the calculations with $U = 3$ and $J = 1$ in Sec. 7.1. For the calculations shown in this sections $n_z = 3$ with $\sigma = 0.63$ and $n_z = 8$ with $\sigma = 0.2$ was used to compare them with the results for $n_z = 1$ with $\sigma = 0.8$ from Sec. 7.1.

The outcome of these calculations is shown in Fig. 7.5 for half-filling ($n_d = 1$) and for less than half-filling ($n_d = 0.6$) in Fig. 7.6. In both cases the number of z-shifts n_z did not affect the number of DMFT iterations needed. Due to the decrease in σ considerably more structure can be observed for larger amounts of z-shifts.

The results shown in Fig. 7.5 correspond to those shown in Fig. 7.3 with half filling ($n_d = 1$), despite σ and n_z the same parameters were used and the same amount of DMFT iterations were needed. As we decrease σ while increasing n_z, the maximums at $|\omega| \simeq 3$ become much more distinctive, more structure in the spectral functions can be observed. For $n_z = 3$ with $\sigma = 0.63$ iNRG and sNRG spectral functions match best and even in the enlarged inset in the right panel of Fig. 7.5 no differences can be seen. However, for $n_z = 8$ and $\sigma = 0.2$ differences between iNRG and sNRG can even be observed at the scale of $A(\omega)$ at $|\omega| \simeq 3$ (relative difference of about 4%), which will be examined in this section in more detail.

Fig. 7.6 shows the results corresponding to the calculations in Fig. 7.1 with a site-specific filling below half-filling ($n_d = 0.6$). When decreasing σ while increasing n_z a small bump at $\omega \simeq 5.5$ becomes visible at $n_z = 8$, which cannot be seen at all in the $n_z = 1$ calculations but already shows up slightly in the $n_z = 3$ calculations. For the results in Fig. 7.6 no differences on the scale of $A(\omega)$ can be seen between iNRG and sNRG calculations. For the $n_z = 3$ results differences between iNRG and sNRG are not even visible in the enlarged plots (see insets in Fig. 7.6), while for $n_z = 8$ differences at $\omega \simeq 0.2$ are visible with a maximum relative deviation of $\sim 0.01\%$, which is about the same as that found for $n_z = 1$ (also $\sim 0.01\%$, see Sec. 7.1). For $n_z = 8$ wiggles are visible for iNRG results in the enhanced insets, which indicates that the used broadening parameter σ is not chosen large enough.

As we found for the results in Fig. 7.6 and Fig. 7.5 that the $n_z = 8$ results for iNRG show wiggles (Fig. 7.6) and considerably large differences to sNRG results (Fig. 7.5), we now want to examine this counterintuitive behavior more closely. To do that we show an enlarged version of the right inset in Fig. 7.6, that is shown in Fig. 7.7. As opposed to the right inset in Fig. 7.6, we do not plot the $n_z = 1$ results in Fig. 7.7 and the $n_z = 3$ results are broadened with the same broadening parameter as the $n_z = 8$ results ($\sigma = 0.2$) to compare the accuracy of $n_z = 3$ and $n_z = 8$ results. Note that only the averaged spectral functions are plotted for iNRG. In Fig. 7.7 it can clearly be seen that the $n_z = 8$ results for iNRG show the largest wiggles, even larger than the $n_z = 3$ results for both iNRG and sNRG. This can be explained with the discussion in Sec. 4.2, where we have found that the iNRG grids for $n_z = 8$ and $M_{iNRG} = 2$ essentially replicate each other 7 times with just enlarged outer intervals. The $n_z = 3$ results however show the same accuracy for both iNRG and sNRG, here the grids are not shifted on top of each other for iNRG.

All in all iNRG yields good results even with z-averaging when compared to corresponding sNRG calculations. However, as seen especially in Fig. 7.7 the iNRG results become worse of too many z-shifts are performed due to grids for different z-parameters replicating each other with enlarged outer intervals. With the results shown in this section z-averaging seems reasonable up to around $n_z \simeq 3$.

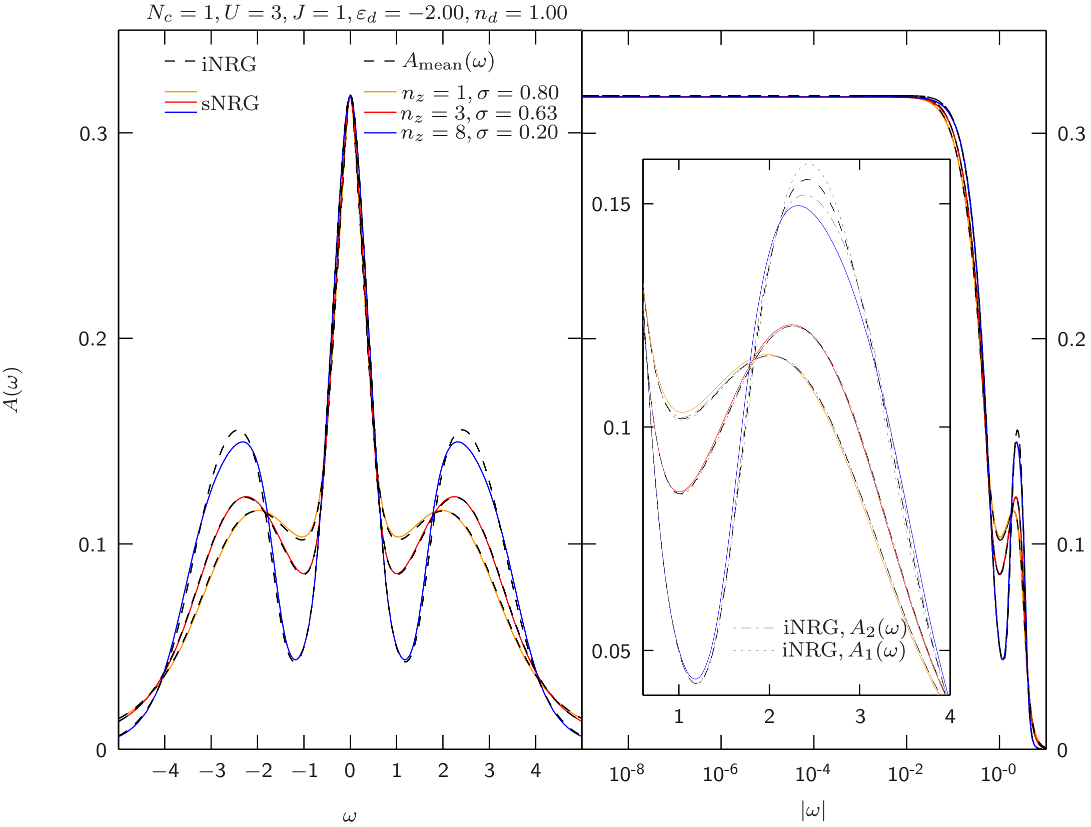

Figure 7.5.: Comparison of iNRG and sNRG for different n_z, corresponding to the spectral functions shown in figure 7.3. In the left panel a linear scale for ω was used, the right panel uses a logarithmic scale for ω. The increase in resolution of the spectral functions with increasing n_z can be clearly seen. sNRG and iNRG match best at $n_z = 3$, for $n_z = 8$ quite large differences (maximum relative difference of $\sim 4\%$) can be observed at $|\omega| \simeq 2.5$. In the inset of the right panel an enlarged plot of the spectral functions for $0.5 < \omega < 4$ on a linear scale can be seen with flavor-resolved results for iNRG. General parameters: $T = 10^{-8}$, $\Lambda = 2$, $E_{\mathrm{trunc}} = 8$, $N_{\mathrm{keep}}^{\mathrm{max}} = 2500$, $\delta\rho_{\mathrm{disc}}^{\mathrm{sNRG}} \simeq 5 \cdot 10^{-9}$, $\delta\rho_{\mathrm{disc}}^{\mathrm{iNRG}} \simeq 4 \cdot 10^{-8}$

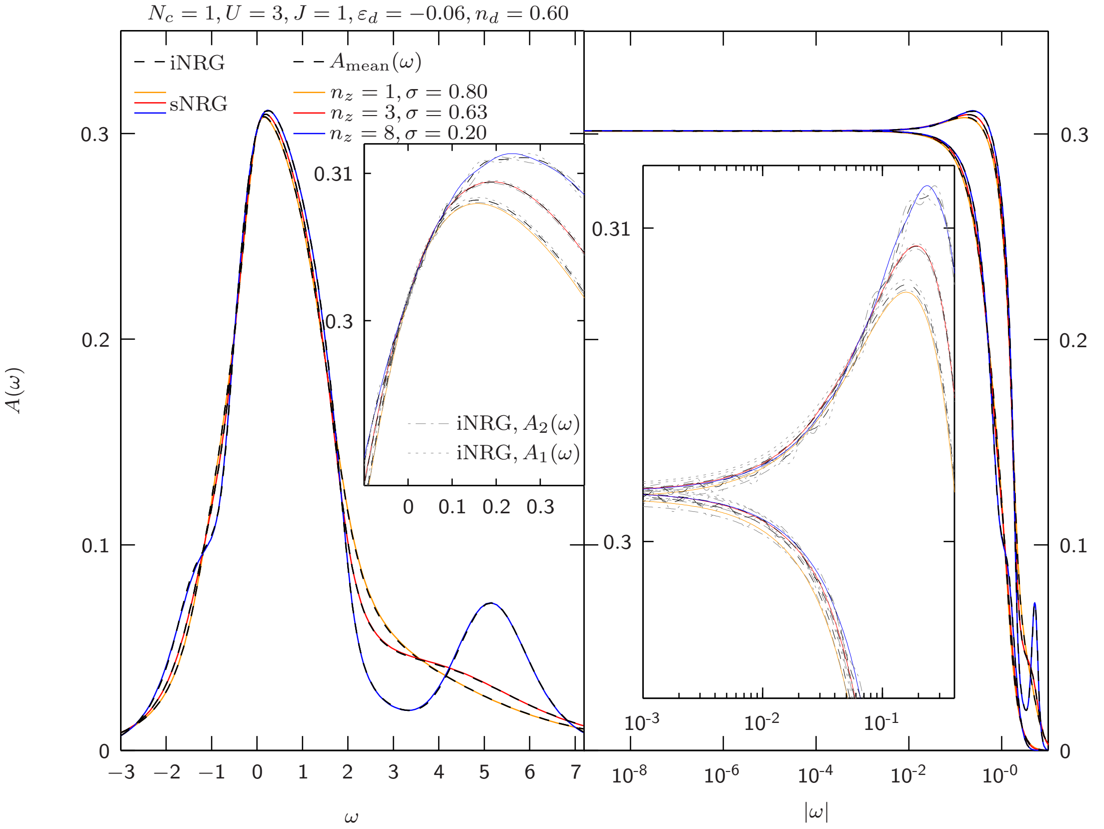

Figure 7.6.: Comparison of iNRG and sNRG for different n_z, corresponding to the spectral functions shown in figure 7.1. For the left panel a linear scale for ω has been used, while for the right panel the ω-scale is logarithmic. The resolution of $A(\omega)$ increases clearly with n_z and the best correspondence between iNRG and sNRG can be observed at $n_z = 3$. Unlike in Fig. 7.5, there is no differences on the scale of $A(\omega)$ can be observed between iNRG and sNRG at $n_z = 8$, but in the $n_z = 8$ iNRG spectral functions wiggles can clearly be seen. To examine those wiggles further an enhanced plot on a logarithmic scale can be found in figure 7.7. Parameters: $T = 10^{-8}$, $\Lambda = 2$, $E_{\mathrm{trunc}} = 8$, $N_{\mathrm{keep}}^{\mathrm{max}} = 2500$, $\delta\rho_{\mathrm{disc}}^{\mathrm{sNRG}} \simeq 6 \cdot 10^{-9}$, $\delta\rho_{\mathrm{disc}}^{\mathrm{iNRG}} \simeq 6 \cdot 10^{-8}$

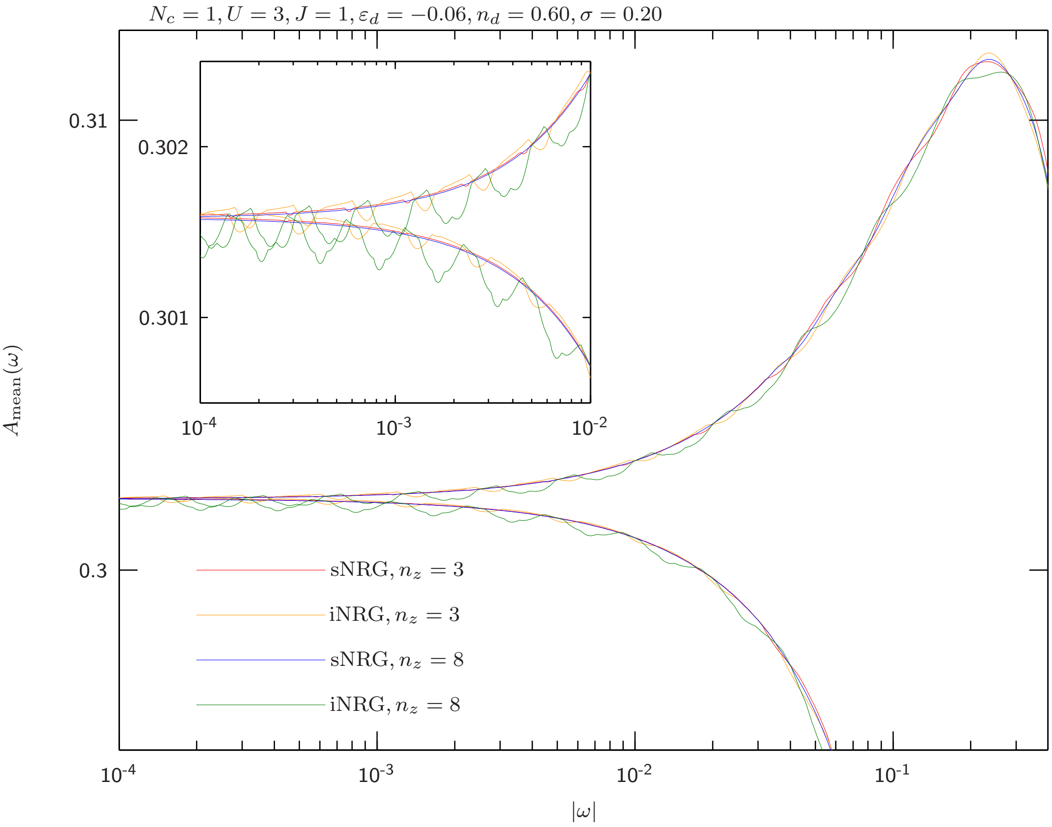

Figure 7.7.: Enhanced plot of the spectral functions for $n_z = 3$ and $n_z = 8$ shown in Fig. 7.6 on a logarithmic scale for ω between $10^{-4} < |\omega| < 1$. Note that, as opposed to the results shown in Fig. 7.6, the $n_z = 3$ spectral functions are broadened with the same broadening parameter ($\sigma = 0.2$) as the $n_z = 8$ spectral functions to compare their accuracy. Also, only the flavor-averaged spectral functions are shown for iNRG. It can clearly bee observed that the largest wiggles occur for the $n_z = 8$ iNRG spectral function. This indicates that both iNRG and sNRG yield more accurate results with $n_z = 3$ than iNRG with $n_z = 8$ does. For $n_z = 8$, the discretization grids for different flavors and shift parameters z are shifted on top of each other, effectively replicating each other with enlarged outer intervals, which happens 7 times for $n_z = 8$. For a more detailed explanation of that see the text written for this section and especially Sec. 4.2.

7.3. One-band Mott insulator transition (MIT)

Last but not least we test the quality of DMFT + iNRG by means of the one-band Mott insulator transition (MIT) and compare the obtained results to corresponding sNRG calculations. As the MIT only occurs at integer filling, we choose $\varepsilon_d = -\frac{3}{4}J$, $U = \frac{J}{2}$ with an arbitrary Hund's coupling J, which leads to half-filling ($n_d = 1$). It should be noted here that the only remaining on-site interaction for the AHM (see Eq. (6)) with the parameters chosen here is $H^{int} = -J\boldsymbol{S}^2$, which puts the artificial SU(2)-spin symmetry breaking in iNRG into question. We initialize the iterative DMFT procedure with a metallic input hybridization. Four different DMFT + NRG calculations were performed with J varying from $J = 1$ to $J = 5.5$. Based on our observations in Sec. 7.2, we choose $n_z = 3$ z-shifts.

The results for the one-band MIT can be found in Fig. 7.8. First of all, in the metallic phase ($J = 1 - 4$), we observe a perfect correspondence between iNRG and sNRG with no deviations visible. However, in the insulating phase ($J = 5.5$), the average spectral function obtained from iNRG matches the sNRG one very bad, with only the same general tendency. The flavor-resolved spectral functions for iNRG in the insulating phase do not match at all.

As the on site interaction is only dependent on the total spin $\boldsymbol{S}^2$, putting artificial SU(2)-spin symmetry breaking into question, we test the MIT also for the AHM with $J = 0$, $\varepsilon_d = -\frac{U}{2}$ and arbitrary U, which also leads to half filling ($n_d = 1$). With $U \hat{=} 1.5 \cdot J$ the exact same on site interaction energies are reproduced as for the previously discussed case. However, the results from the $J = 0$ calculations come out exactly the same as those shown in Fig. 7.8 for both iNRG and sNRG and are therefore not plotted.

Presumably iNRG fails at the MIT because the underlying physics is not stable when breaking the SU(2)-spin symmetry. This could for example be tested by using iNRG Wilson chain couplings for a sNRG calculation in the insulating phase, but this was not done here.

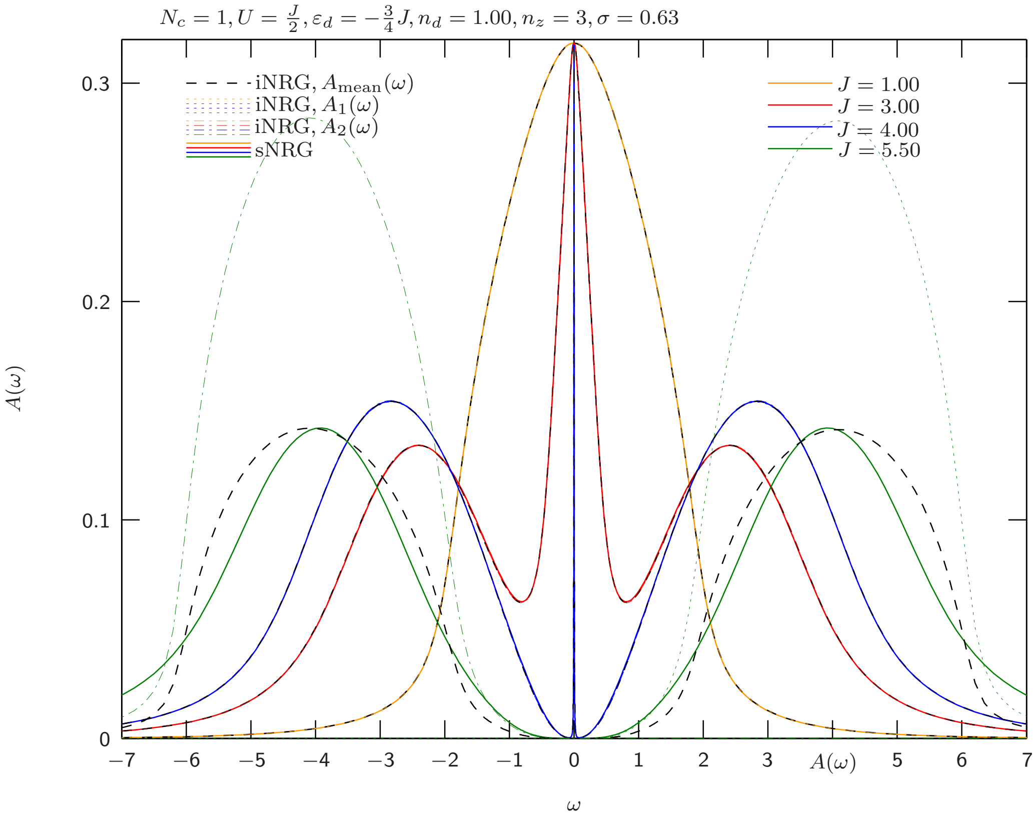

Figure 7.8.: One band Mott insulator transition. The critical value of J is found to be $J_c \simeq 4$. If $J = 0$, $\varepsilon_d = -\frac{U}{2}$ and arbitrary U is chosen, one gets the exact same results for $U \hat{=} 1.5 \cdot J$. In this case we find a critical U of $U_c \simeq 6$, which is in good accordance to the results in [13]. Parameters: $T = 10^{-8}$, $\Lambda = 2$, $E_{\text{trunc}} = 8$, $N_{\text{keep}}^{\text{max}} = 2500$

8. Two band Anderson Hund Model

In this chapter we test DMFT+iNRG by means of the two-band Anderson Hund Model. For the band-symmetric two-band model we will start by comparing two results without z-averaging, then test the performance of z-averaging and finally turn to the Mott insulator transition. After that the two band Anderson Hund model without band symmetry will be examined.

As in chapter 7, the main goal will be to determine the quality and performance of iNRG by comparing spectral functions from converged DMFT loops, Wilson chain couplings and computation time to corresponding sNRG calculations. The basis for our comparisons will again be the local spectral functions $A(\omega)$.

In Sec. 8.1, Sec. 8.2 and Sec. 8.3 we will consider the band-symmetric two-band AHM (Eq. 6.1), which means $\varepsilon_{d,1} = \varepsilon_{d,2} \equiv \varepsilon_d$. In iNRG calculations we will interleave the bands, but not the spins ($M_{\text{iNRG}} = 2$) and therefore artificially break the band-symmetry, which should be treated with caution. In every DMFT iteration we will take the average over the iNRG results from different bands and use it as input for the next iteration. Band-asymmetric ($\varepsilon_{d,1} \neq \varepsilon_{d,2}$) two band results will be treated in Sec. 8.4.

All calculations presented in the following sections have all been performed on the Bethe lattice (see Sec. 2.6) and all energies are given in terms of the half-band width D of the non interacting density of states (see Eq. (2.26)). The chemical potential $\mu = 0$ will be set to zero and $\hbar$ and k_B are both set to 1. All spectral functions shown are calculated via Eq. (2.28) with the self energy obtained from the self-energy trick discussed in Sec. 5.1, Eq. (5.2). Spectral functions obtained directly from the FDM-NRG approach (see Sec. 3.8) are not shown. The criteria for DMFT convergence is a maximum change of less than 10^{-3} in the spectral functions compared to the preceding DMFT iteration. After convergence is reached, three more iterations to truly ensure DMFT convergence are performed. We initiate the DMFT procedure with a flat hybridization in the interval $\omega \in [-D, D]$ that leads to a metallic result after the first iteration.

8.1. Band symmetric results without z-averaging

First we discuss our NRG + DMFT results obtained for band symmetric ($\varepsilon_{d,1} = \varepsilon_{d,2} \equiv \varepsilon_d$) models. In the iNRG calculations the bands have been interleaved, breaking the band symmetry, but not the spins, therefore $M_{iNRG} = 2$.

To begin with, the difference between iNRG and sNRG spectral functions are much more notable than for the one band results which is probably due to $\Lambda_{N_c=1} = 2 < 3 = \Lambda_{N_c=3}$. But at least for the metallic spectral functions shown in figure 8.1, iNRG and sNRG fit together very well. For both iNRG and sNRG, no wiggles are visible, so the same minimum broadening parameter σ can be used, which means they are both equally accurate for $n_z = 1$.

The insulating spectral function in figure 8.2 though shows the same disagreement between the spectral functions for channel 1 and channel 2 that already occurred in the one band Mott insulator transition (see section 7.3). The spectral functions are only acceptable if one averages over them. For now it seems that iNRG has problems if we approach insulating states. This is not generally the case as we will see in section 8.3 and chapter 9, where insulating spectral functions, calculated with iNRG, will be presented that show no such problems. It is not completely clear why this instability in the results in figure 8.2 shows up. The most natural reason would be that the underlying physics are just unstable under symmetry breaking, which could for example be tested by running an sNRG calculation with the same parameters but slightly broken band symmetry. An other reason might be the bad resolution of the logarithmic discretization grid far away from the chemical potential, as the iNRG spectral functions are treated there with a considerable large asymmetry.

For band-symmetric two band calculations iNRG is already faster than sNRG, taking 680 seconds per DMFT iteration as opposed to 770 seconds, despite the exploited band symmetry in sNRG and its more efficient implementation.

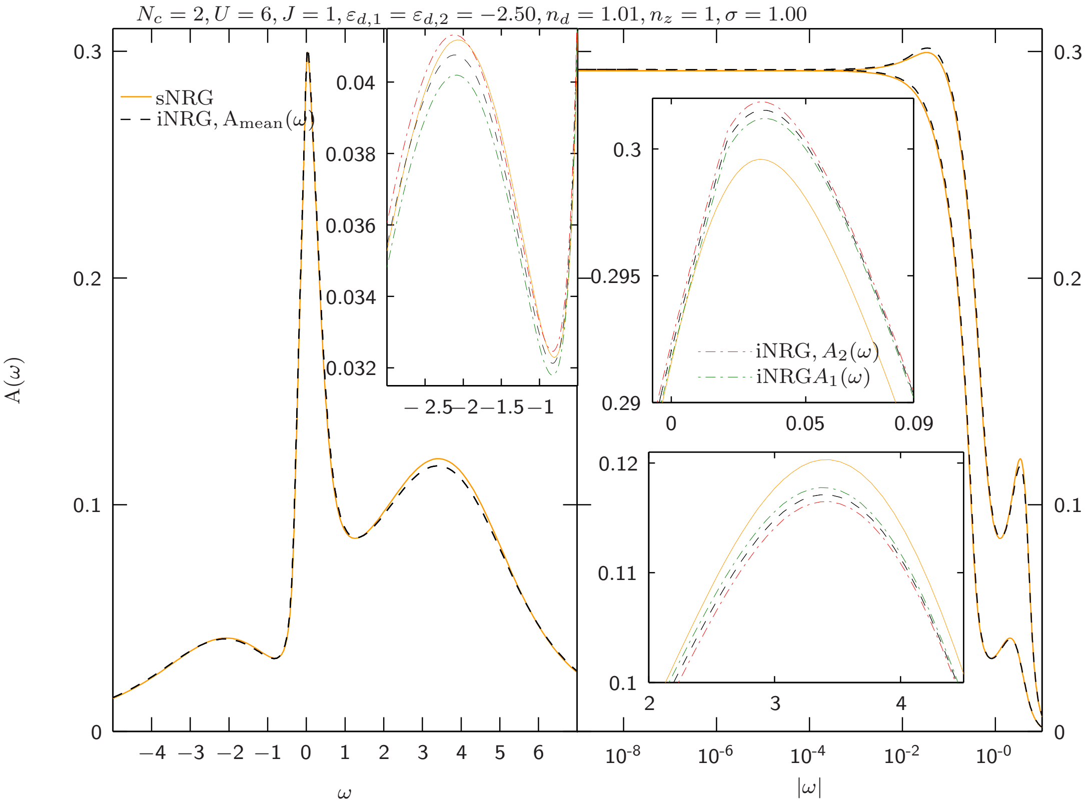

Figure 8.1.: Comparison of spectral functions for both iNRG and sNRG for the last, converged DMFT iteration (iteration 10). In iNRG calculations the bands were interleaved ($M_{\mathrm{iNRG}} = 2$). As opposed to the one band results shown in Sec. 7.1, deviations (maximum relative error of $\sim 3\%$) between iNRG and sNRG can be seen in the scale of the spectral functions. The iNRG spectral functions for different channels match well and cannot be distinguished on a scale of $A(\omega)$. In the left panel a linear scale for ω is used, in the right panel the scale for ω is logarithmic. The insets show enhanced details with flavor resolved iNRG data on a linear scale for ω. Parameters: $T = 10^{-8}$, $\Lambda = 3$, $E_{trunc} = 7.5$, $N_{keep}^{max} = 3000$, $\delta\rho_{\mathrm{disc}}^{\mathrm{iNRG}} = 2.1 \cdot 10^{-6}$, $\delta\rho_{\mathrm{disc}}^{\mathrm{sNRG}} = 2.7 \cdot 10^{-7}$

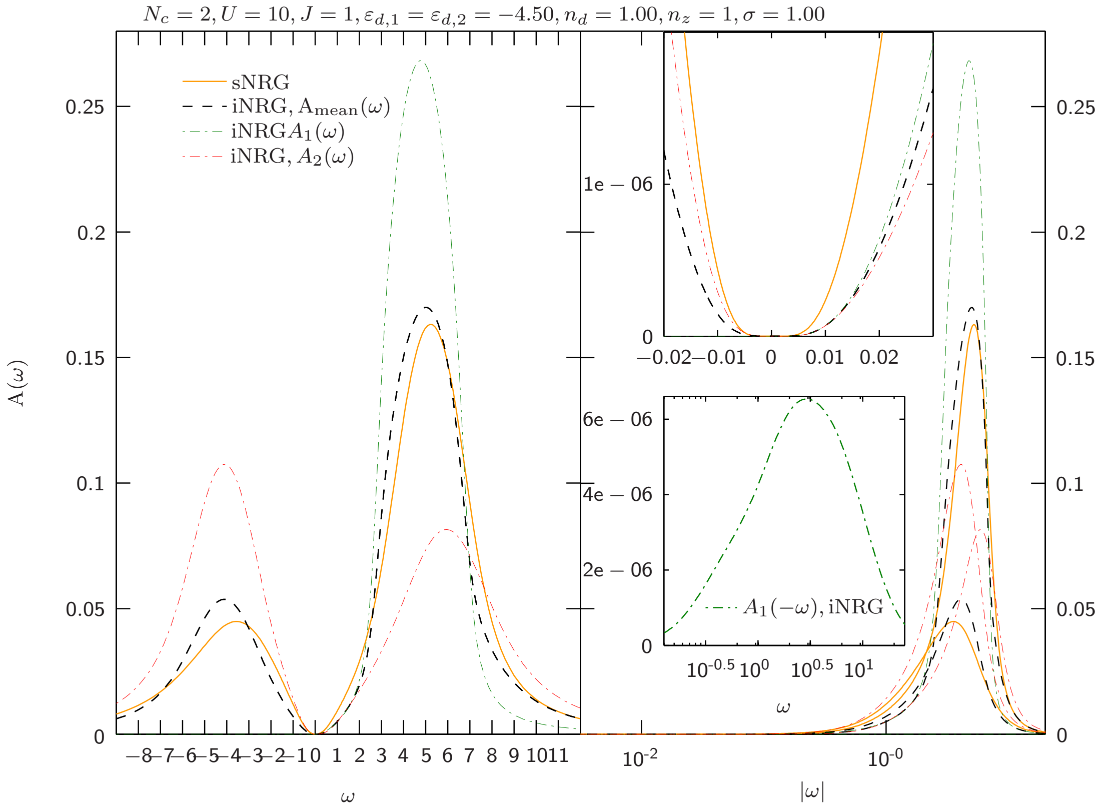

Figure 8.2.: Comparison between iNRG and sNRG converged spectral functions (DMFT iteration 17 for iNRG, 23 for sNRG) for a band-symmetric AHM in the insulating state. In iNRG calculations the bands were interleaved ($M_{\mathrm{iNRG}} = 2$). The site-specific filling is chosen below half-filling ($n_d = 1$). In contrast to the results shown in figure 8.1, the iNRG spectral functions for band 1 and band 2 do not match at all, although the mean value of both iNRG spectral functions is acceptable. For the left panel a linear scale for ω is used, for the right panel the scale is logarithmic. Note that the green $A_1(\omega)$ curve for $\omega < 0$ is slightly larger than 0. It can be found in the lower inset featuring the green curve only, where a logarithmic scale for ω was used. In the upper inset details of the spectral features at around $\omega \simeq 0$ are shown on a linear scale. Parameters: $T = 10^{-8}$, $\Lambda = 3$, $E_{trunc} = 7.5$, $N_{keep}^{max} = 3000$, $\delta\rho_{\mathrm{disc}}$ has not been calculated

8.2. Bandsymmetric results with z-averaging

We now z-average the results obtained in section 8.1. We use $n_z = 4$ and adjust σ accordingly to match the gain in accuracy.

In general the $n_z = 4$ spectral functions for sNRG and iNRG match better than the $n_z = 1$ ones, and due to the decrease in σ, more structure can be seen. Also, the iNRG spectral functions for channel 1 and channel 2 match significantly better.

The insulating iNRG spectral functions for $n_z = 4$ shown in figure 8.5 match the sNRG spectral function for $n_z = 4$ notably better than in the $n_z = 1$ case. In the alignment of the iNRG spectral functions for the different channels there can also be observed an improvement. Surprisingly the mean iNRG spectral functions for $n_z = 4$ and $n_z = 1$ are very similar and the $n_z = 4$ results for sNRG and iNRG after averaging actually match in an acceptable way. As the iNRG spectral functions for the different channels are significantly better aligned after z-averaging, it can be assumed that for some values of z these spectral functions might actually almost completely match. Unfortunately, the data of the individual z-shifts has not been saved due to limited amount of disk memory and could therefore not be checked. At $\omega \simeq 0$ the iNRG $n_z = 4$ spectral functions show an unusual behavior with unknown origin.

In figure 8.4 the Wilson chain couplings that led to the results in figure 8.3 are given for two different values of the shift parameter z. While for $z = 0$ the sNRG and iNRG couplings match almost perfectly, this is not the case for $z = \frac{3}{4}$ where the sNRG couplings are systematically larger than the iNRG couplings. At $z = \frac{3}{4}$ the iNRG couplings, as opposed to the sNRG ones, show values very similar the couplings at $z = 0$. An explanation for this is that the iNRG grid points for $z = \frac{3}{4}$ are shifted exactly on the sNRG grid points for $z = 0$, as discussed in section 4.2. Nevertheless, both iNRG and sNRG couplings show an almost perfect logarithmic decay which explains the good quality of the results in figure 8.3.

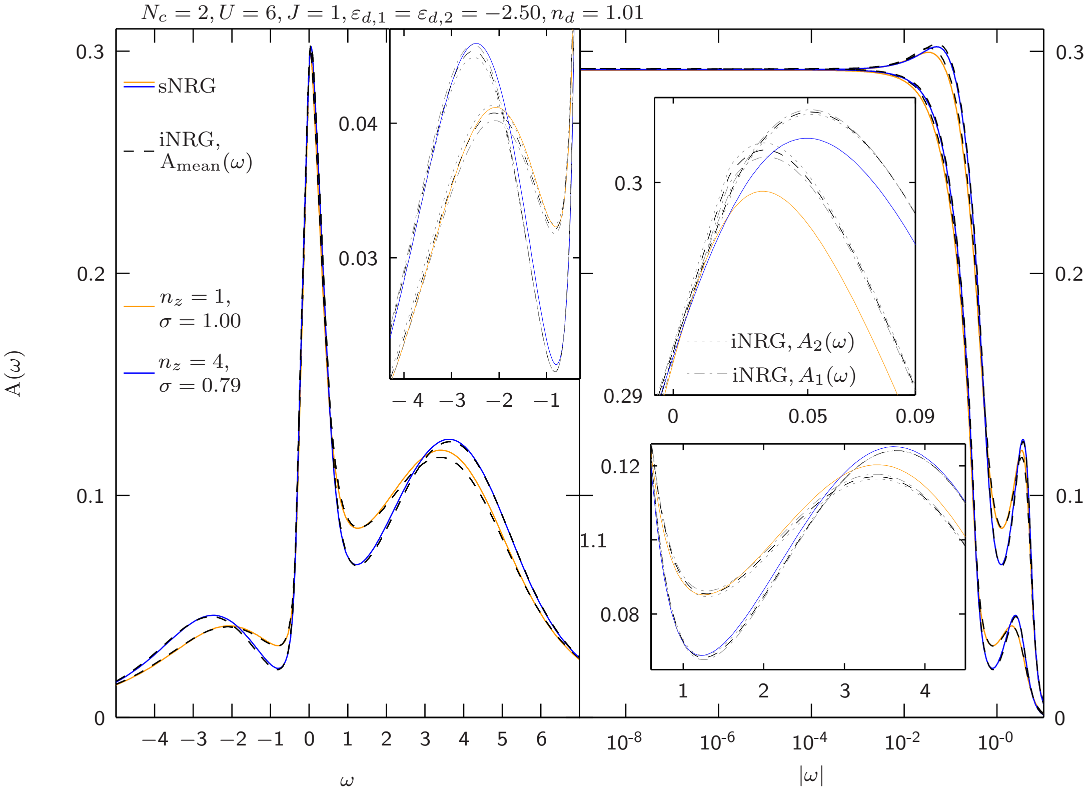

Figure 8.3.: Comparison of iNRG and sNRG calculations performed with different amounts of z-shifts and accordingly adjusted broadening parameter ($n_z = 1, \sigma = 1$ and $n_z = 4, \sigma = 0.79$). All other parameters are chosen as for the results shown in Fig. 8.1. In iNRG calculations the bands have been interleaved ($M_{\text{iNRG}} = 2$). The spectral function for $n_z = 4$ is notably improved by the z-averaging and more structure is visible due to the decrease in σ. The maximum relative error in the spectral functions for $n_z = 4$ is $\sim 1\%$. In figure 8.4 corresponding Wilson chain couplings can be found. Parameters: $T = 10^{-8}$, $\Lambda = 3$, $E_{trunc} = 7.5$, $N_{keep}^{max} = 3000$, $\delta\rho_{\text{disc}}^{\text{iNRG}} \simeq 2.5 \cdot 10^{-6}$, $\delta\rho_{\text{disc}}^{\text{sNRG}} \simeq 3 \cdot 10^{-7}$

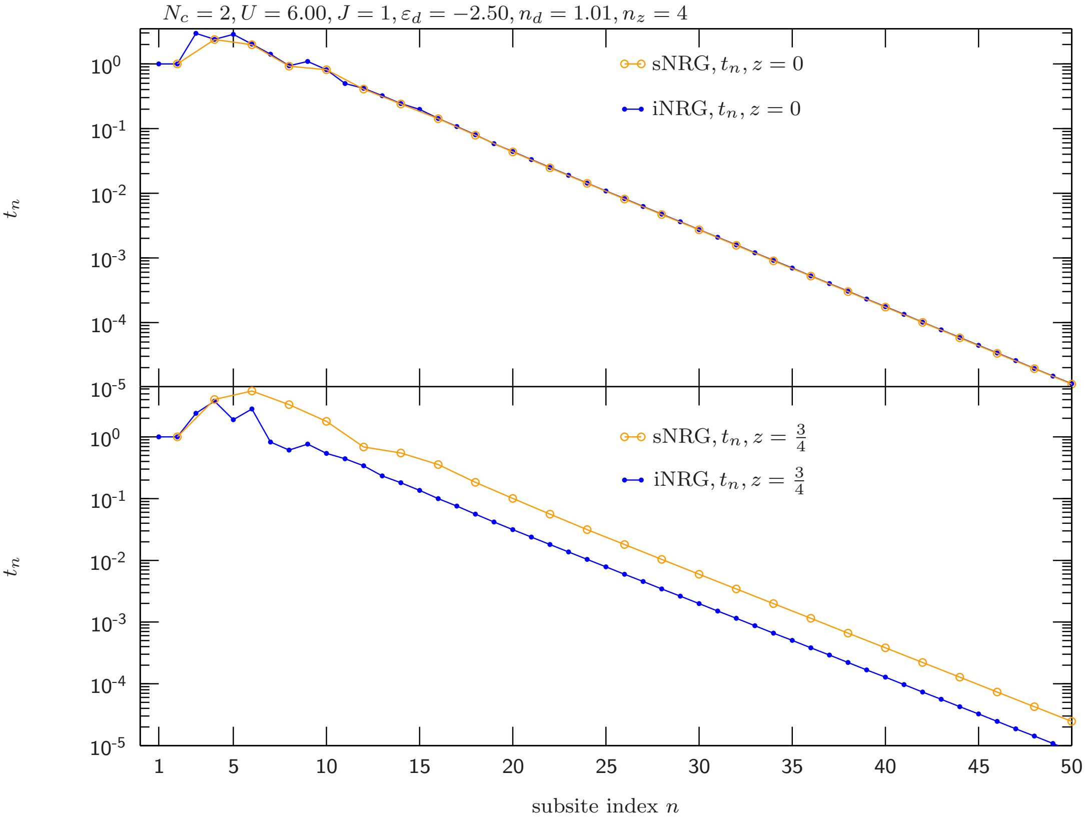

Figure 8.4.: Wilson chain couplings that led to the converged spectral functions shown in Fig. 8.3. For both shift parameters $z = 0$ and $z = \frac{3}{4}$ an almost perfect logarithmic decay can be observed for both iNRG and sNRG. As opposed to the $z = 0$ couplings, the $z = \frac{3}{4}$-couplings for iNRG and sNRG do not match. Especially for the first few iNRG sites an increase of the couplings compared to preceding couplings can be observed, preventing truncation for these sites.

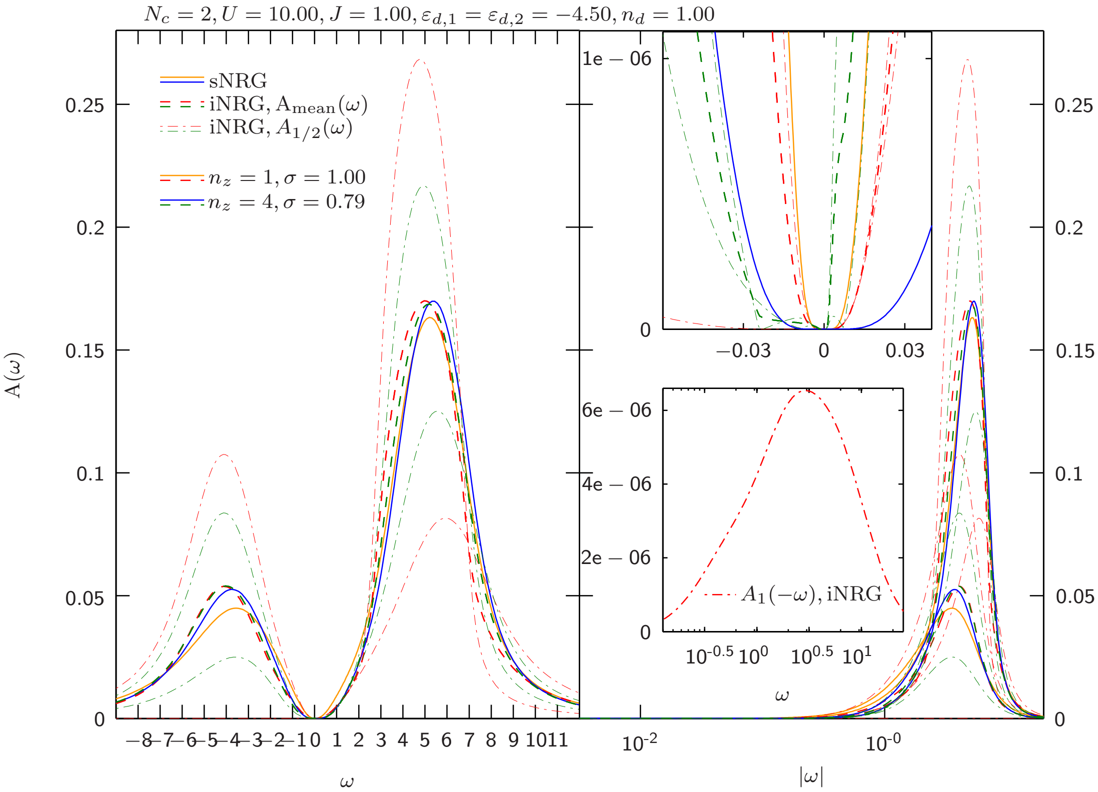

Figure 8.5.: Comparison of iNRG and sNRG spectral functions for different amounts of z-shifts and accordingly adjusted broadening parameter ($n_z = 1, \sigma = 1$ and $n_z = 4, \sigma = 0.79$). All other parameters are chosen as for the results in figure 8.2. The result for $n_z = 4$ is improved compared to $n_z = 1$, but still barely acceptable. Note the uncommon behavior of the $n_z = 4$ spectral function at $\omega \simeq 0$. Corresponding Wilson chain couplings can be found in figure 8.6. Parameters: $T = 10^{-8}$, $\Lambda = 3$, $E_{trunc} = 7.5$, $N_{keep}^{max} = 3000$, $\delta\rho_{\mathrm{disc}}$ has not been calculated

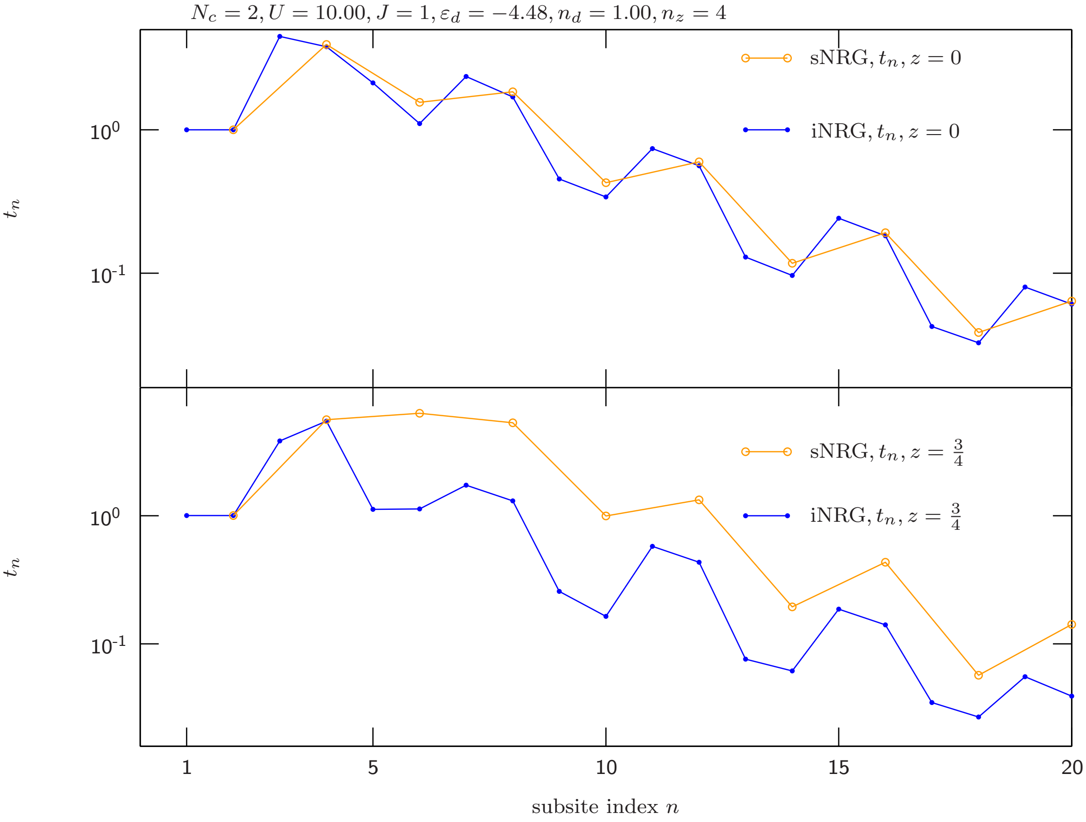

Figure 8.6.: Wilson chain couplings leading to the converged spectral functions in figure 8.5. Due to the large weight of the spectral functions far away from the Fermi-level, the couplings do not show a perfect logarithmic decay, although the overall tendency is adhered to.

8.3. Bandsymmetric two band Mott insulator transition

In this section we turn to the band symmetric two band Mott insulator transition. In our first Mott insulator calculation we obtain integer filling by choosing the particle hole symmetric form of the Anderson Hund model with $U = \frac{J}{2}$, $\varepsilon_d = -\frac{3}{4}J$ and arbitrary J, which yields half filling ($n_d = 2$). Our calculations yield a critical J of $J_c \simeq 1.8$, which is considerably smaller than $J_c^{N_c=1} \simeq 4.0$ obtained for the one band Mott insulator transition in section 7.3.
We get consistent iNRG results that agree almost perfectly with the sNRG results. Slight, but notable differences between sNRG and iNRG only occur from $J = 1.5$ to $J = 2.4$.

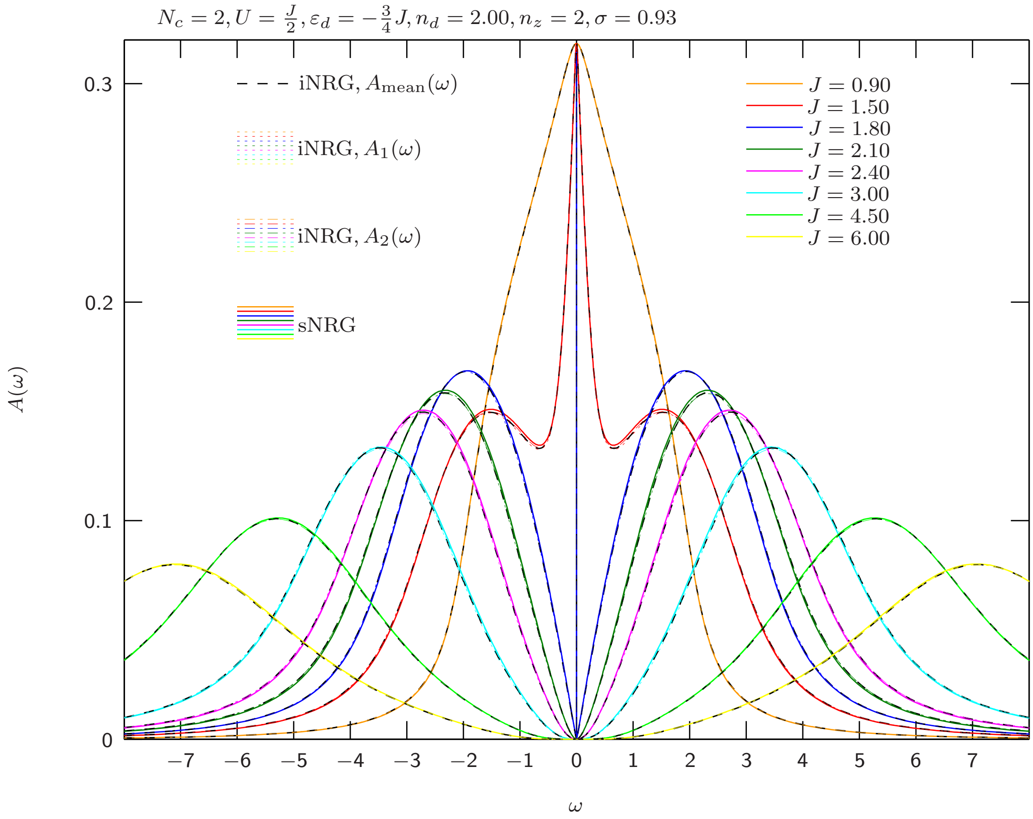

Figure 8.7.: Particle hole symmetric two band Mott insulator transition. The spectral functions for iNRG and sNRG match very well. The pointed behavior of the spectral functions at $\omega \simeq 0$ near the Mott insulator transition is no discontinuity of $\frac{\partial A(\omega)}{\partial \omega}$, the curve is smooth there. The spectral functions for $J = 1.8$ are not fully converged with an error of $\simeq 10^{-2}$. Parameters: $T = 10^{-8}$, $\Lambda = 3$, $E_{trunc} = 7.5$, $N_{keep}^{max} = 3000$

In our next two calculations we examine the dependence of the Hunds coupling J on the Mott insulator transition at half filling $n_d = 2$. For that we choose a constant J and increase U to induce the transition. ε_d is chosen by the formula

$$\varepsilon_d = -\frac{3}{4}J - \frac{1}{2}(U - \frac{1}{2}J)(2N_c - 1) \tag{8.1}$$

which is acquired by demanding the same on site energies for sites with filling $2N_c$ and 0. We further adjust ε_d by linear interpolation to fine tune it. The Mott insulator transition with half filling is then calculated for constant $J = 1$ and $J = \frac{1}{2}$.

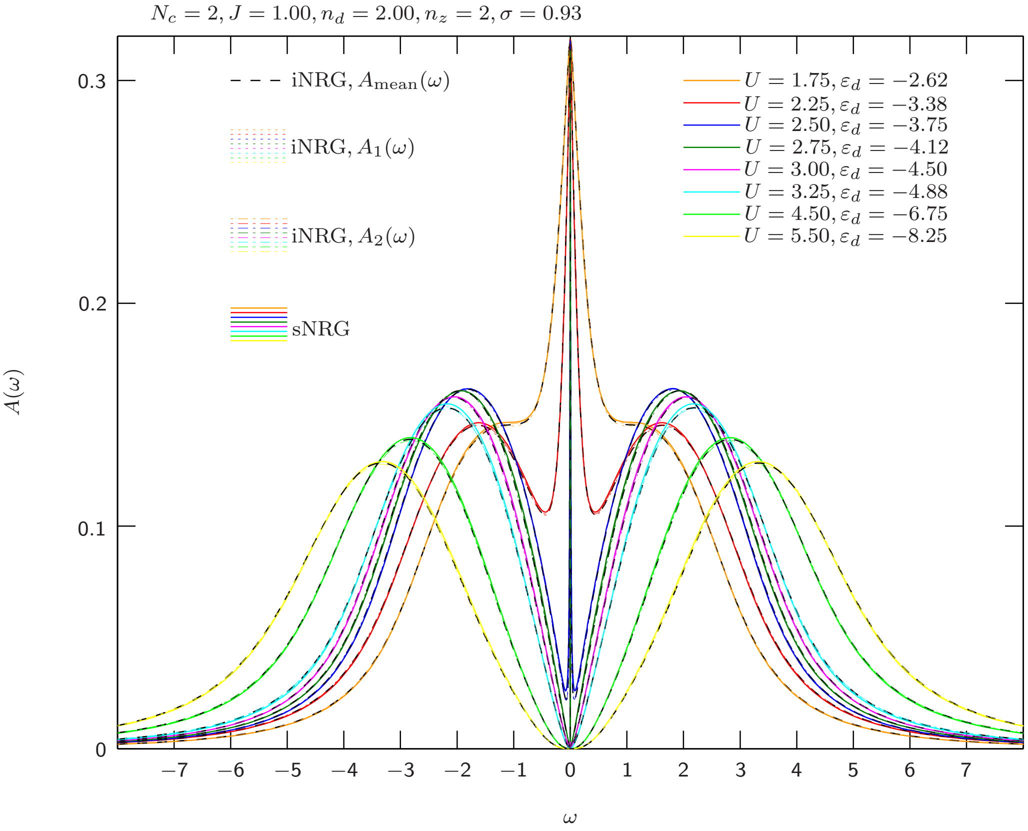

Figure 8.8.: Two band, U-driven Mott insulator transition at half-filling ($n_d = 2$) with constant $J = 1$ and band symmetry. For the critical Coulomb interaction $U_c = 2.75$ was found in both iNRG and sNRG calculations. Corresponding iNRG and sNRG results match quite well, only small differences can be observed. Note that the sharp features at $\omega \simeq 0$ in the spectral functions close to the Mott transition are no discontinuities of $\frac{\partial A(\omega)}{\partial \omega}$. The spectral functions for $U = 2.5$ and $U = 2.75$ are not fully converged (error $\simeq 10^{-2}$). Parameters: $T = 10^{-8}$, $\Lambda = 3$, $E_{trunc} = 7.5$, $N_{keep}^{max} = 3000$

First of all we find that the critical Coulomb interaction energy for the transition with $J = 1$ is $U_c \simeq 2.75$ while we get $U_c \simeq 4.25$ for the $J = \frac{1}{2}$ case. This means that a larger Hunds coupling J clearly decreases U_c for the Anderson Hund Model at half filling and

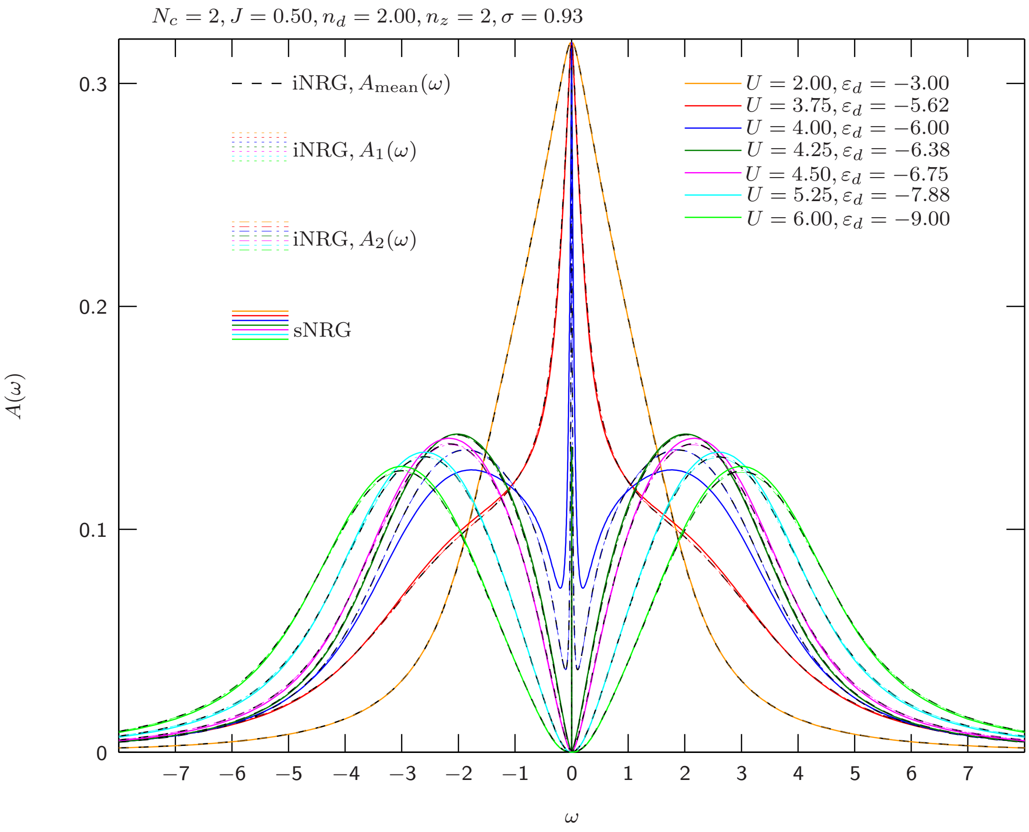

Figure 8.9.: Two band, U-driven Mott insulator transition with $n_d = 2$, constant $J = \frac{1}{2}$ and band symmetry. For both iNRG and sNRG calculations $U_c \simeq 4.25$ was found. iNRG and sNRG spectral functions mostly coincide. The sNRG spectral function for $U = 4.0$ is not fully converged (error of $\simeq 10^{-2}$). The sharp features of the spectral functions occurring at $\omega \simeq 0$ are no $\frac{\partial A(\omega)}{\partial \omega}$ discontinuities. Parameters: $T = 10^{-8}$, $\Lambda = 3$, $E_{trunc} = 7.5$, $N_{keep}^{max} = 3000$

was also found in [4] and [13].
iNRG and sNRG results coincide very well for most parts. But especially for $J = \frac{1}{2}$ and $U = 4.0$ respectively $J = 1$ and $U = 2.5$, close to the Mott transition while still in the metallic regime, quite large differences can be observed. Nevertheless, both iNRG and sNRG calculations produce the same critical U_c. Most importantly, the iNRG results are self consistent.
Last but not least we take a look at the Mott insulator transition for with filling $n_d = N_c - 1 = 1$ and its dependence on J. We again choose a constant J and increase U do induce the Mott transition. ε_d is acquired by the formula

$$\varepsilon_d = -\frac{2 \cdot (NC - 1) + 1}{2} \cdot (U - J) \quad , \tag{8.2}$$

which can be found in [1] and are additionally fine tuned during DMFT iterations by linear interpolation. We again calculate the Mott insulator transition for both $J = \frac{1}{2}$ and $J = 1$ with iNRG and sNRG. While in the half filling case U_c calculated with iNRG and sNRG agreed, this is unfortunately not the case for $n_d = 1$. But as the results very close to the Mott transition are not fully converged, comparisons are difficult. The $J = 1$ case yields for iNRG $U_c^{iNRG} \simeq 8.0$ while for sNRG the transition occurs at a considerably larger $U_c^{sNRG} \simeq 9.0$.

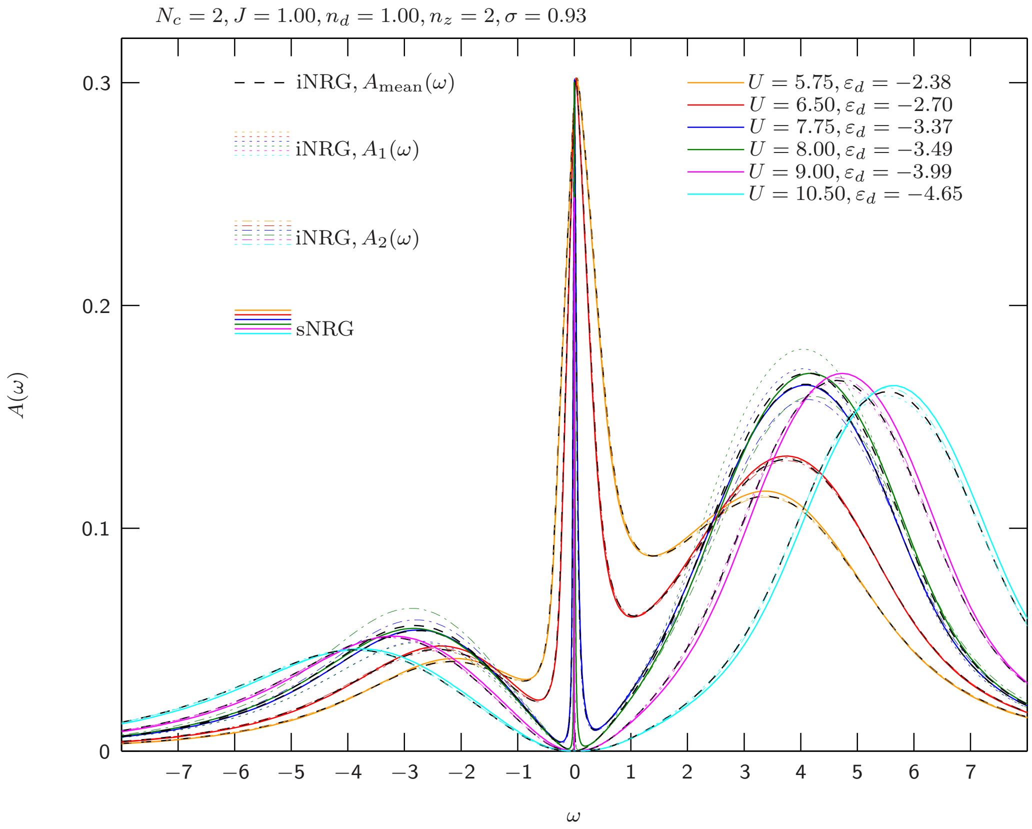

Figure 8.10.: Two band, U-driven Mott insulator transition for filling $n_d = 1$, constant $J = 1$ and band symmetry. We find a critical Coulomb interaction of $U_c^{\text{sNRG}} \simeq 9.0$ for sNRG and $U_c^{\text{iNRG}} \simeq 8.0$ for iNRG. However, the results for $U = 8$ and $U = 9.25$ are not fully converged (error: $\simeq 10^{-2}$), making comparisons difficult. iNRG and sNRG results coincide well, near the Mott transition larger deviations in the iNRG spectral functions for different bands can be observed. Parameters: $T = 10^{-8}$, $\Lambda = 3$, $E_{trunc} = 7.5$, $N_{keep}^{max} = 3000$

The values for $J = \frac{1}{2}$ are slightly smaller with $U_c^{iNRG} \simeq 7.75$ and $U_c^{sNRG} \simeq 8.75$, which would mean that and increase in J leads to a slightly larger U_c, as opposed to the $n_d = 2$ case where we found the opposite. This also coincides with the findings in [4] and [13]. One can also observe that near the Mott transition the iNRG results not only differ from the sNRG ones but are also not totally self consistent by showing considerable differences in the spectral functions for the different bands. With the results shown in 8.2 this could already be expected.

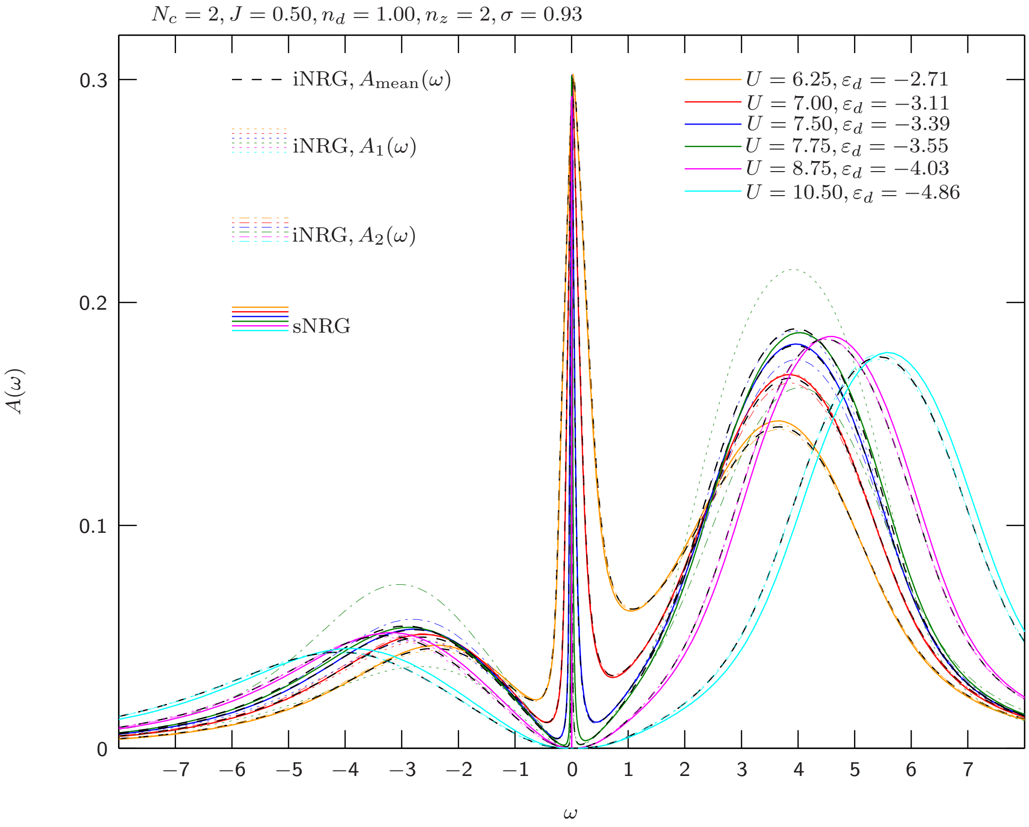

Figure 8.11.: Two band, U-driven Mott insulator transition for filling $n_d = 1$ with constant $J = 0.5$ and band-symmetry. We find $U_c^{\mathrm{iNRG}} \simeq 7.75$ and $U_c^{\mathrm{sNRG}} \simeq 8.75$, but as the results for $U = 7.75$ and $U = 8$ are not converged comparisons are merely possible. Near the Mott insulator transition discrepancies in the iNRG spectral functions for different bands can be observed. Parameters: $T = 10^{-8}$, $\Lambda = 3$, $E_{trunc} = 7.5$, $N_{keep}^{max} = 3000$

8.4. Band asymmetric two band results

Last but not least the two band Anderson Hund Model with asymmetric bands has been examined. Here, $\varepsilon_{d,1/2}$ were predetermined rather than n_d. Indications for good values for $\varepsilon_{d,1/2}$ were taken from band symmetric calculations.
For the results shown in figure 8.12, two different DMFT + NRG calculations with reversed band order have been performed for iNRG. The shown iNRG results are then obtained by averaging over the results of the two calculations. It should be emphasized

here that the averaging was performed only after DMFT convergence for the final results, not for every DMFT iteration.

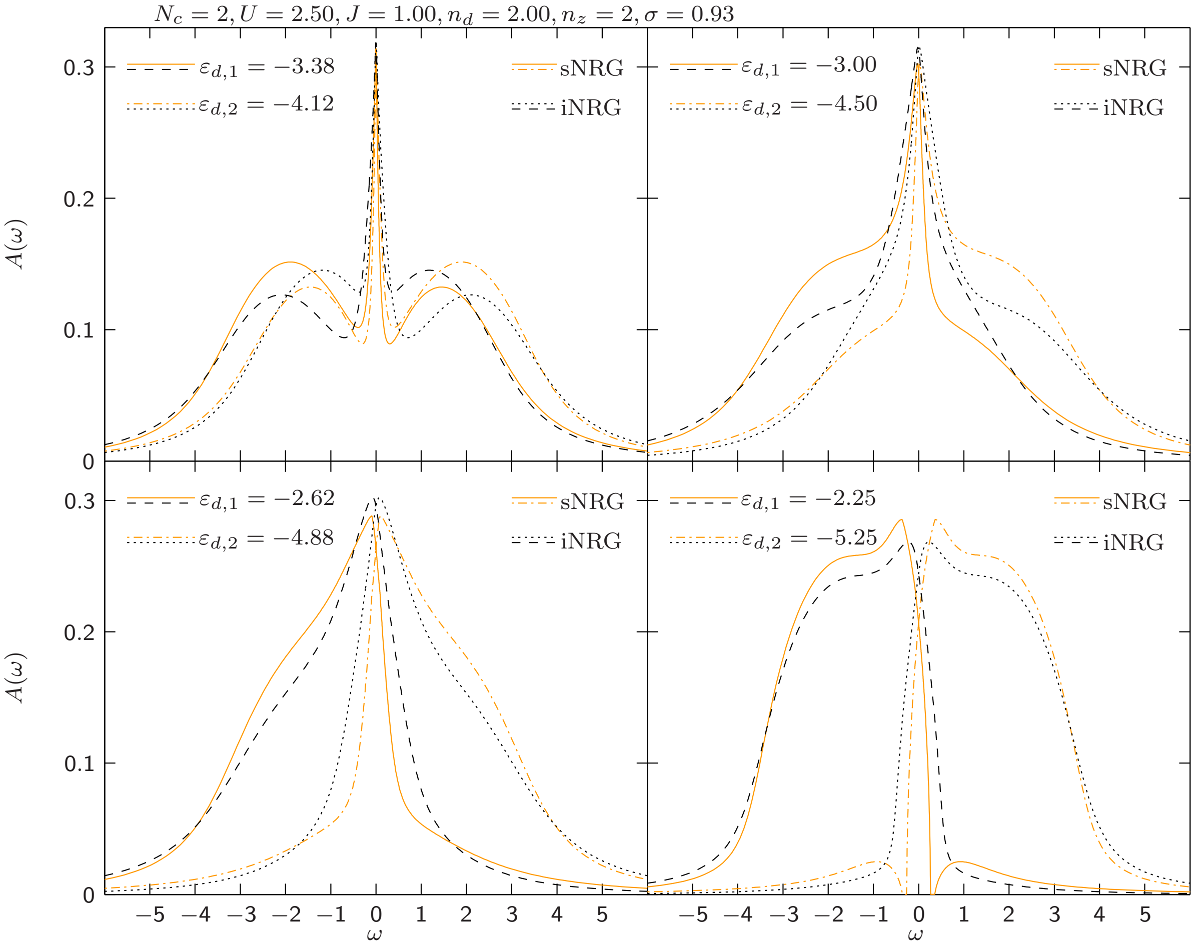

Figure 8.12.: Spectral functions for two band Anderson Hund Model without band symmetry. sNRG and iNRG yield reasonable results but differ clearly, even though two iNRG calculations with reversed band order have been performed and averaged over for the iNRG result. In this figure only the averaged iNRG spectral functions are shown, as the spectral functions from different iNRG calculations with reversed band order match almost perfectly and cannot be distinguished on the shown scale. The spectral functions for sNRG and iNRG in the first subplot look interchanged, but this is not the case. The sNRG spectral functions in the last subplot get negative at $|\omega| \simeq 0.25$ and are therefore cut off. Parameters: $T = 10^{-8}$, $\Lambda = 3$, $E_{trunc} = 7.5$, $N_{keep}^{max} = 3000$, $\delta\rho_{\text{disc}}$ has not been calculated

The iNRG and sNRG spectral funtions show the same tendency, but are quite different and do not match very well, although both results look reasonable. With more z-shifts applied the results might coincide better. In figure 8.13 the Wilson chain couplings for the last iteration and $z = \frac{1}{2}$ are shown. They show a very good logarithmic decay, the couplings for the different iNRG calculations match perfectly. With these results it is hard to say whether iNRG or sNRG deliver the better results. The only indication are the cut off sNRG spectral functions shown in the last subplot in figure 8.12 and the fact that for a large $|\varepsilon d, 1 - \varepsilon_{d,2}|$ the iNRG calculations yield unreasonable results for a yet unknown reason.

In figure 8.14 a band asymmetric Mott insulator transition is shown. It is successful for both iNRG and sNRG, and shows the same properties, mainly that $J_c = 1.8$ for both iNRG and sNRG. Nevertheless, the iNRG and sNRG spectral functions differ clearly and yield definitely not the same results.

In the band-asymmetric case where no channel symmetry can be exploited in sNRG calculations, serious computation time differences between iNRG and sNRG could be observed. In iNRG calculations one DMFT iteration took about 16 minutes (with $n_z = 2$ as opposed to $n_z = 1$ in section Sec. 8.1), while sNRG calculations took 70 minutes per DMFT iteration.

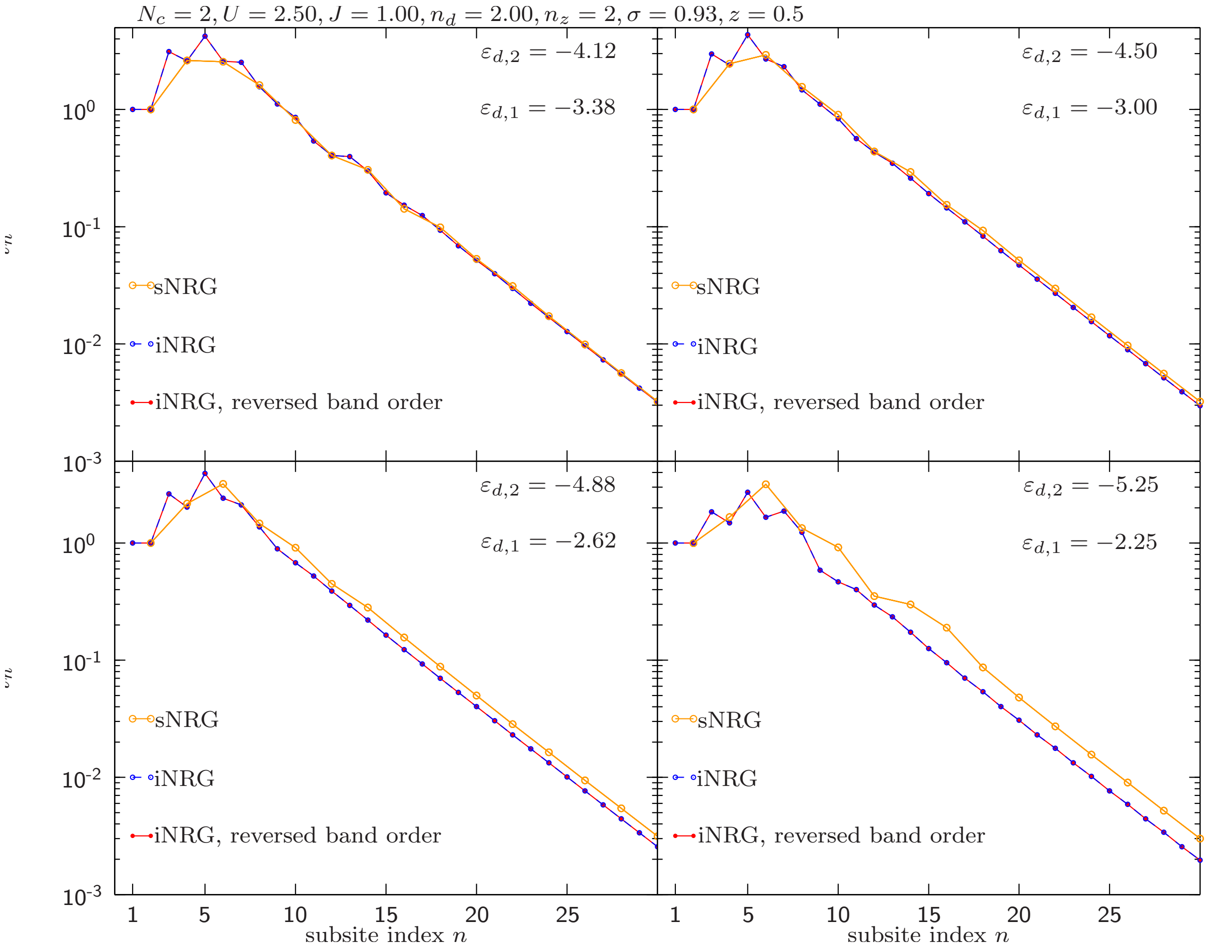

Figure 8.13.: Wilson chain couplings corresponding to the results shown in figure 8.12. Both iNRG and sNRG couplings show an almost perfect logarithmic decay after about 3 supersites. The couplings for iNRG calculations with reversed band orders are almost identical.

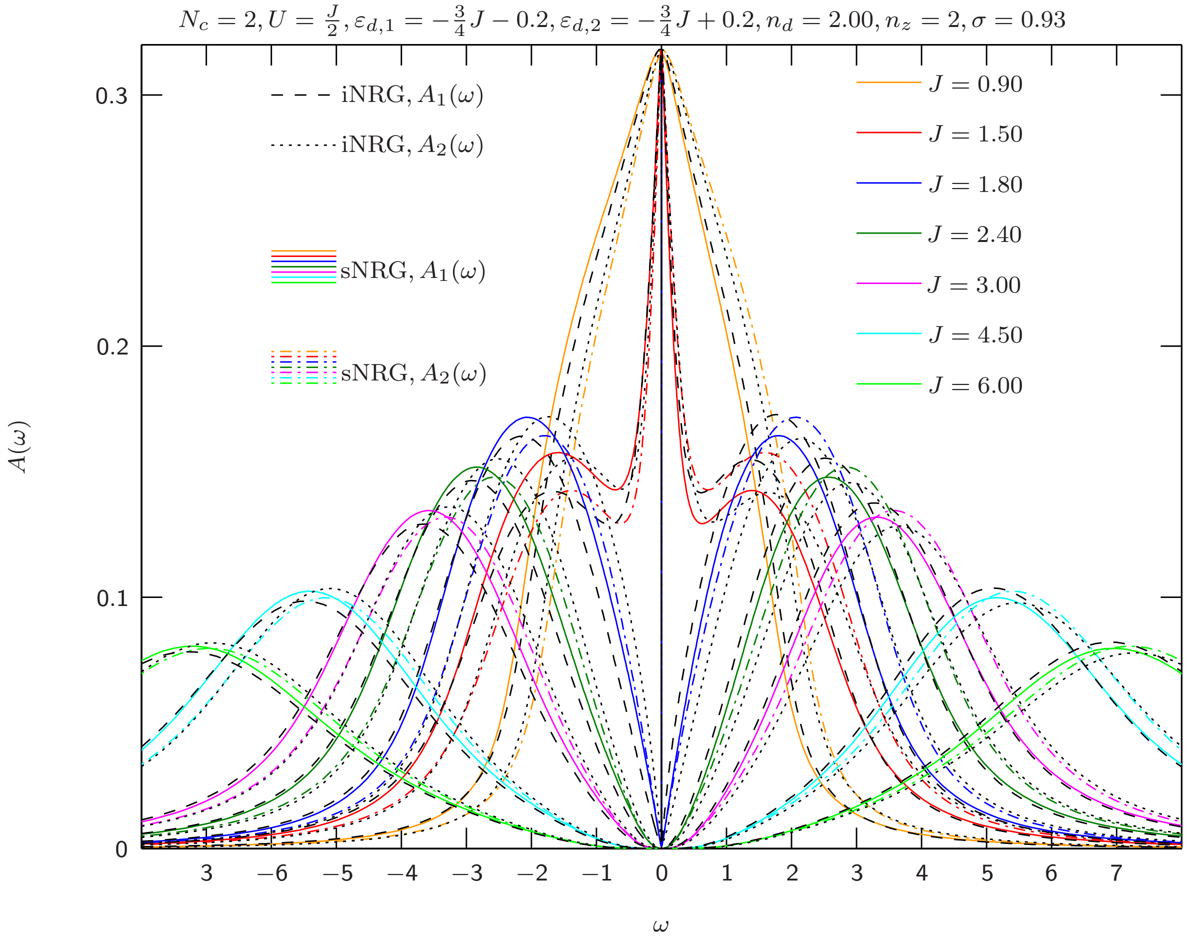

Figure 8.14.: Band asymmetric two band Mott insulator transition. The results for both iNRG and sNRG look reasonable, but do clearly differ. Nevertheless, the spectral functions obtained from both methods show the same overall properties. In contrast to the iNRG results seen in figure 8.12, no averaging with reversed band order has been performed for the iNRG results. For $J = 1.5$, either the iNRG or the sNRG spectral functions seem interchanged, but as in figure 8.12 this is not the case. As for the symmetric two band Mott insulator transition shown in figure 8.7, no discontinuity of $\frac{\partial A(\omega)}{\partial \omega}$ occurs. The spectral functions at $J = 1.8$ are not fully converged (error of $\simeq 10^{-2}$). Parameters: $T = 10^{-8}$, $\Lambda = 3$, $E_{trunc} = 7.5$, $N_{keep}^{max} = 3000$

9. Three band Anderson Hund Model

This chapter will treat the three-band Anderson Hund Model with the DMFT+iNRG approach. In Sec. 9.1 we will start by comparing calculations that exhibit band-symmetry ($\varepsilon_{d,1} = \varepsilon_{d,2} = \varepsilon_{d,3} \equiv \varepsilon_d$) with corresponding sNRG calculations, where we will also see to the computational efficiency of iNRG and sNRG. We then turn to examining the performance of z-averaging for band-symmetric models in Sec. 9.2, where also sNRG results will be our reference. The basis for our comparisons will again be the local spectral function $A(\omega)$, but Wilson chain couplings will also be studied. In Sec. 9.4, we will treat three-band models with non-degenerated bands($\varepsilon_{d,1} \neq \varepsilon_{d,2} = \varepsilon_{d,3}$ and $\varepsilon_{d,1} \neq \varepsilon_{d,2} \neq \varepsilon_{d,3}$). Here, no sNRG calculations as a reference are available, as sNRG is computationally too costly if it is not possible to exploit full band-symmetry.
In iNRG calculations we will interleave the bands, but not the spins ($M_{\text{iNRG}} = 3$). For models with degenerated bands ($\varepsilon_{d,1} = \varepsilon_{d,2} = \varepsilon_{d,3}$ or $\varepsilon_{d,1} \neq \varepsilon_{d,2} = \varepsilon_{d,3}$), the band symmetry is therefore artificially broken in iNRG calculations, which may lead to problems if the symmetry is crucial for the underlying physics and should therefore be avoided. When iNRG is used we will average over the results for degenerated bands in every DMFT iteration and use it as input for the next iteration.
All calculations presented in the following sections have all been performed on the Bethe lattice (see Sec. 2.6) and all energies are given in terms of the half-band width D of the non interacting density of states (see Eq. (2.26)). We set the chemical potential $\mu = 0$ to zero and $\hbar$ and k_B are both set to 1. All spectral functions shown are calculated via Eq. (2.28) with the self energy obtained from the self-energy trick discussed in Sec. 5.1, Eq. (5.2). Spectral functions obtained directly from the FDM-NRG approach (see Sec. 3.8) are not shown. The criteria for DMFT convergence is a maximum change of less than $5 \cdot 10^{-3}$ in the spectral functions compared to the preceding DMFT iteration. After convergence is reached, three more iterations to truly ensure DMFT convergence are performed. The DMFT procedure is initiated with a flat hybridization in the interval $\omega \in [-D, D]$ that yields a metallic result after the first DMFT iteration.

9.1. Band symmetric three band results without z-averaging

We now turn to the band symmetric three band Anderson Hund Model for which we compare our sNRG to our iNRG results. In the iNRG calculations the band symmetry is broken by interleaving the bands, the spins are not interleaved.
The alignment of iNRG and sNRG spectral functions is comparable to that of the two band results but visibly worse than for the one band results. Both iNRG and sNRG

calculations took about 10 DMFT iteration to reach convergence.

The iNRG spectral functions for different bands match quite well, even in the case of an insulator, which was different for the two band results. Note however that in the two band case $n_d = N_c - 1$ was considered, while in the three band case we consider $n_d = N_c$. In the $n_d = N_c$ case for $N_c = 2$, a very good alignment of iNRG and sNRG could be observed when considering the particle hole symmetric Mott insulator transition (see figure 8.7).

As for the accuracy of iNRG compared to sNRG, small swerves can be observed in the iNRG spectral functions shown in figure 9.2, as opposed to the sNRG result, where no such thing happens. These swerves might be a result of the transition from a log Gaussian to a normal Gaussian as a broadening kernel for the discrete spectral function, as this transition happens at $|\omega| = 10^{-7}$.

Even though band-symmetry was be exploited in sNRG calculations, iNRG took considerable less computation time (about 19 minutes per DMFT iteration) compared to sNRG (about 170 minutes per DMFT iteration).

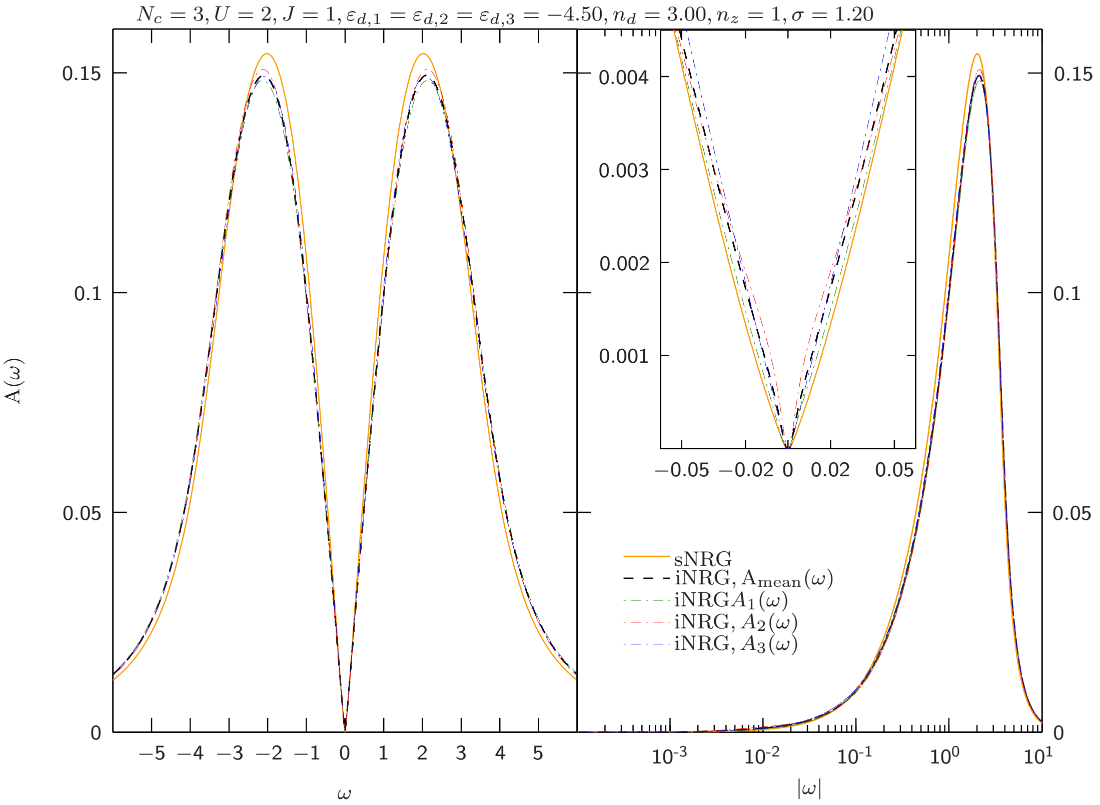

Figure 9.1.: Spectral function for an insulating three band Anderson Hund model with band symmetry. For the site-specific filling half-filling is chosen ($n_d = 3$). The iNRG and sNRG spectral functions match quite well, relative errors of $\simeq 6\%$ occur at $|\omega| \simeq 3$. The spectral funtions show no $\frac{\partial A(\omega)}{\partial \omega}$ discontinuity at $\omega \simeq 0$. Parameters: $T = 10^{-8}$, $\Lambda = 4$, $E_{trunc} = 7$, $N_{keep}^{max} = 3000$, $\delta\rho_{\mathrm{disc}}$ has not been calculated

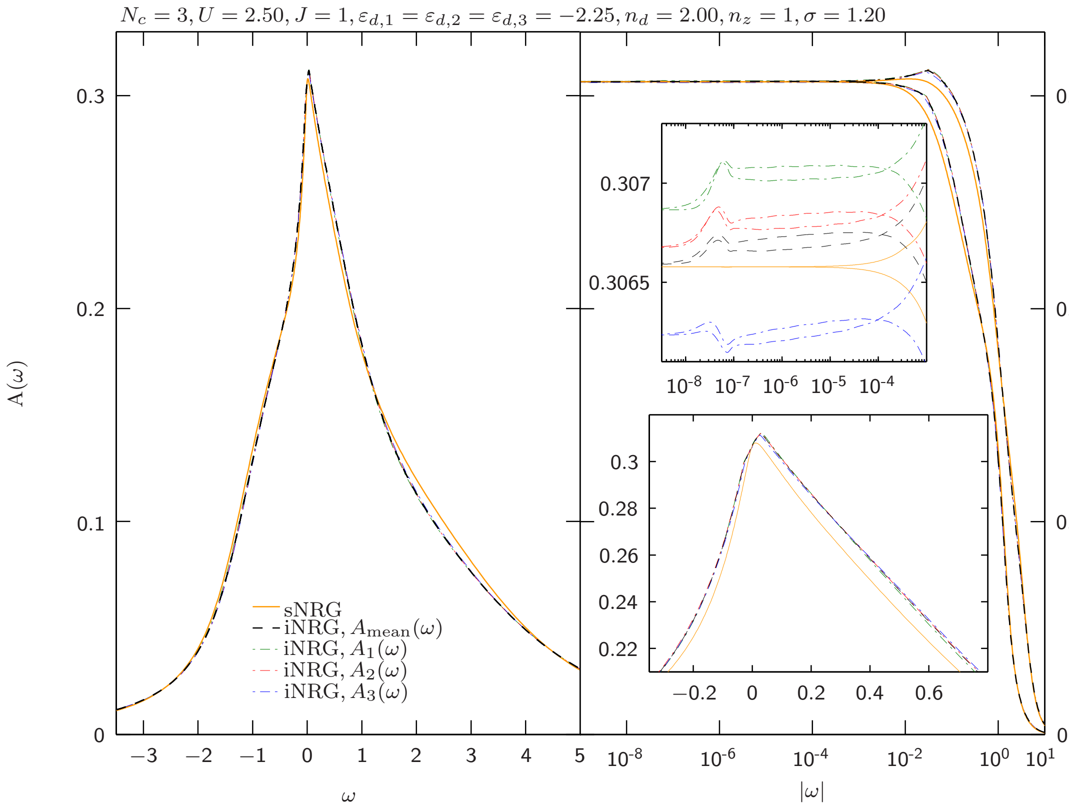

Figure 9.2.: Spectral function for the metallic three band Anderson Hund model with band symmetry. The results for sNRG and iNRG match well. The site-specific filling is chosen below half-filling ($n_d = 2$). We find a maximum relative error of $\simeq 9\%$ between iNRG and sNRG at $\omega \simeq 2.5$. The origin of the swerves between $10^{-8} < |\omega| < 10^{-7}$ are presumably caused by the transition from a log-Gaussian to a regular Gaussian as a broadening kernel in these regions. Parameters: $T = 10^{-8}$, $\Lambda = 4$, $E_{trunc} = 7$, $N_{keep}^{max} = 3000$, $\delta\rho_{\text{disc}}$ has not been calculated

9.2. Band symmetric results with z-averaging

In this section we will examine the effect of z-averaging for three band models. To do that results with $n_z = 1$ and $n_z = 3$ and an appropriate choice of σ are compared for both iNRG and sNRG.

iNRG and sNRG still coincide quite well if z-averaging is used, although they a little worse than for one and two band calculations, which can be explained by the usage of a larger discretization parameter Λ. As opposed to z-averaging in one or two band calculations the benefits of z-averaging are quite small for our three band calculations, probably because we used a smaller amount of z-shifts and therefore cannot lower σ by much.

For the insulating result shown in figure 9.3, the main difference to be observed is a slight broadening of the very sharp minimum at $\omega \simeq 0$ for smaller σ. The iNRG spectral functions for $n_z = 1$ and $n_z = 3$ do not differ by much at all, while for the sNRG spectral functions the broadening is much more distinct and they show an increase in the height of the maximums at $|\omega| \simeq 3$. The corresponding couplings are shown in figure 9.4. Because of the large spectral weight in regions where the logarithmic discretization is very coarse they show no perfect logarithmic decay. For $z = 0$ though the non-logarithmic behavior occurs only between supersites, the iNRG sites within a specific supersite show the intended logarithmic decay. The non-logarithmic behavior for the $z = \frac{2}{3}$ couplings is much more severe, especially for iNRG. Here, the couplings for $\alpha = 1$ iNRG sites lie energetically far lower than the corresponding $\alpha = 2$ and 3 sites.
The metallic results shown in figure 9.5 show a better match of iNRG and sNRG results than the insulating results. Between $n_z = 1$ and $n_z = 3$ no real difference can be observed other that the iNRG results for $n_z = 3$ show small wiggles, indicating a slightly too small broadening parameter σ for these calculations. The corresponding couplings in figure 9.6 show an almost perfect logarithmic decay for $z = 0$, while for $z = \frac{2}{3}$ the couplings for the $\alpha = 1$ iNRG sites lie energetically lower than the $\alpha = 2$ and 3 ones, as has already been observed for the couplings in figure 9.4.

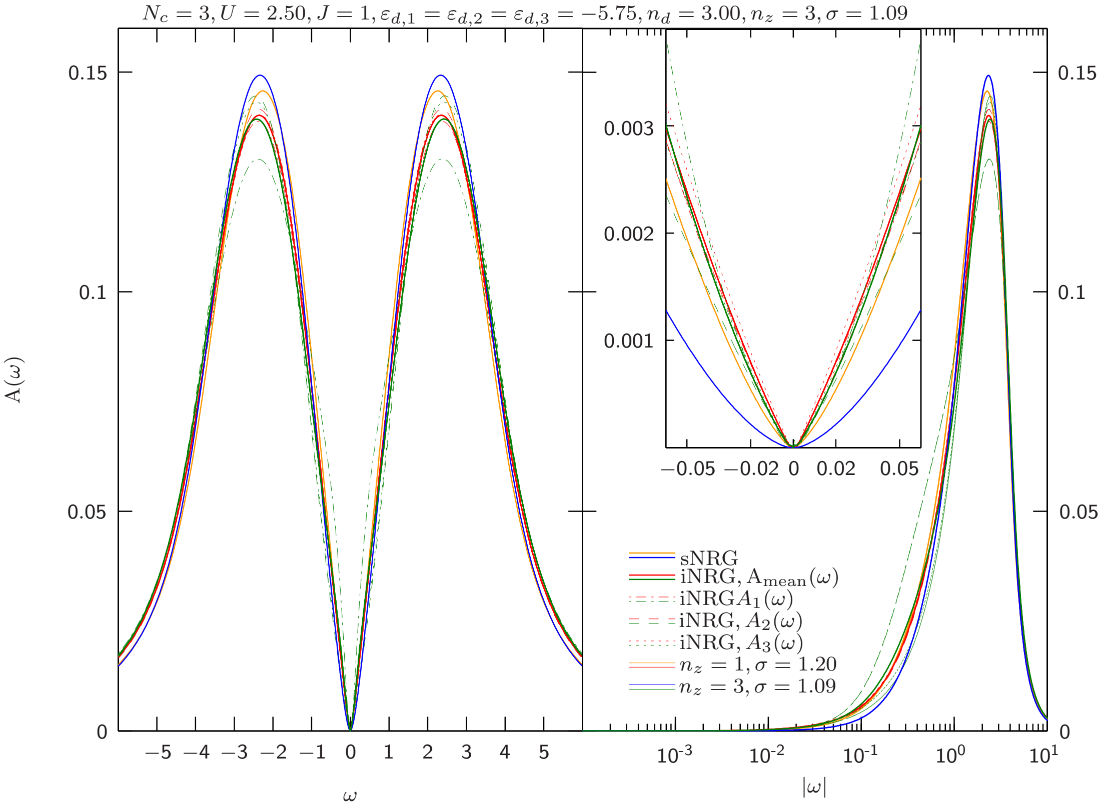

Figure 9.3.: Comparison of spectral functions for a different amount of z-shifts and accordingly adjusted broadening σ ($n_z = 1, \sigma = 1.2$ and $n_z = 3, \sigma = 1.09$). Both iNRG and sNRG results match well, but no meaningful benefit of z-averaging can be found. Between the $n_z = 4$ iNRG and sNRG spectral functions a maximum relative difference of $\sim 10\%$ can be found, being larger than the maximum relative difference for $n_z = 1$ with $\simeq 6\%$. The corresponding Wilson chain couplings can be found in figure 9.4. Parameters: $T = 10^{-8}$, $\Lambda = 4$, $E_{trunc} = 7$, $N_{keep}^{max} = 3000$, $\delta\rho_{\mathrm{disc}}$ has not been calculated

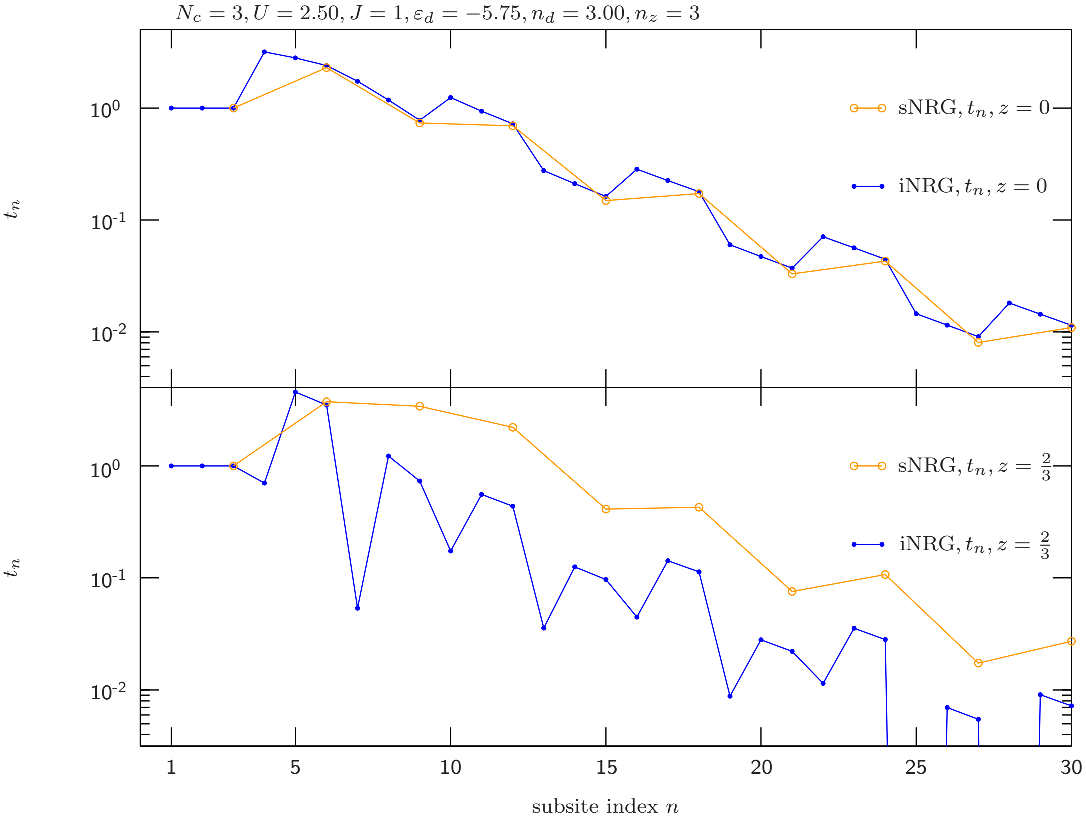

Figure 9.4.: Wilson chain couplings leading to the spectral functions shown in figure 9.3. Especially for $z = \frac{2}{3}$, the couplings for every third iNRG site are energetically considerably lower than the other iNRG couplings, becoming even 0 at site 25 and 27.

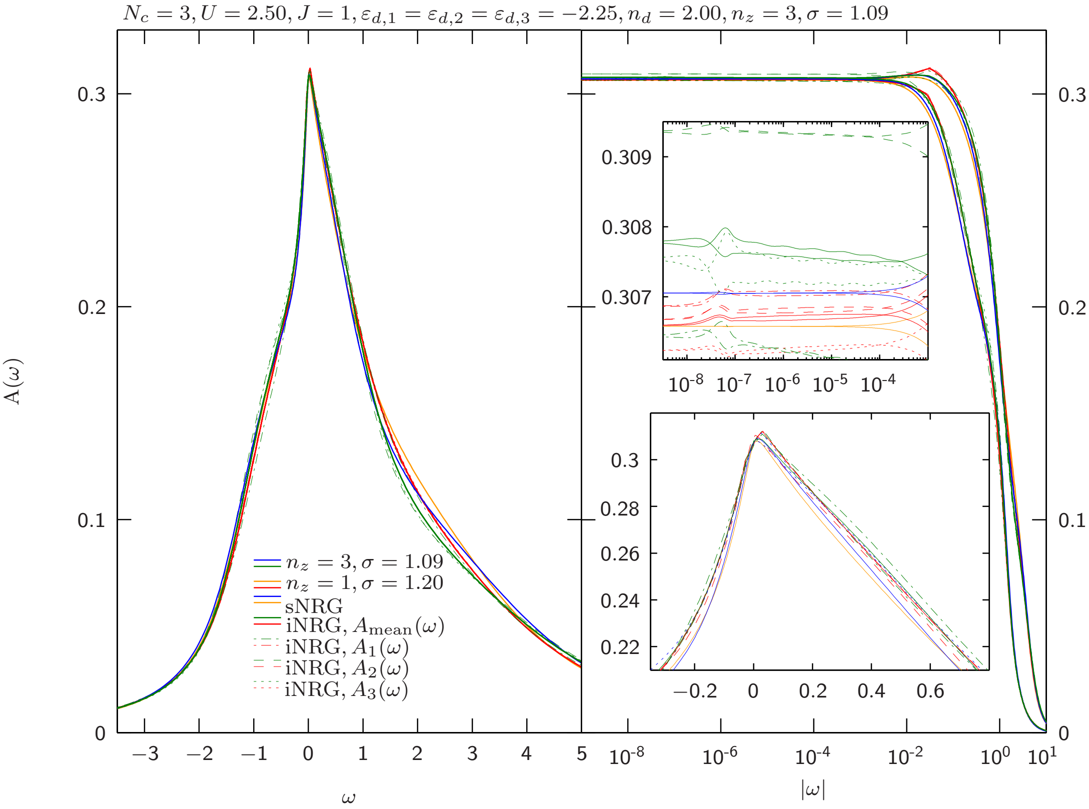

Figure 9.5.: Comparison of spectral functions for $n_z = 1$ and $n_z = 3$. Both iNRG and sNRG spectral functions match quite well, but the benefit gained from z-averaging is very small. Between $n_z = 4$ calculations a maximum relative error of $\simeq 7\%$ can be found. The wiggles in the iNRG $n_z = 4$ spectral functions on a logarithmic ω-scale indicate that σ is not chosen large enough. The Wilson chain couplings leading to these spectral functions can be found in figure 9.6. Parameters: $T = 10^{-8}$, $\Lambda = 4$, $E_{trunc} = 7$, $N_{keep}^{max} = 3000$, $\delta\rho_{\mathrm{disc}}$ has not been calculated

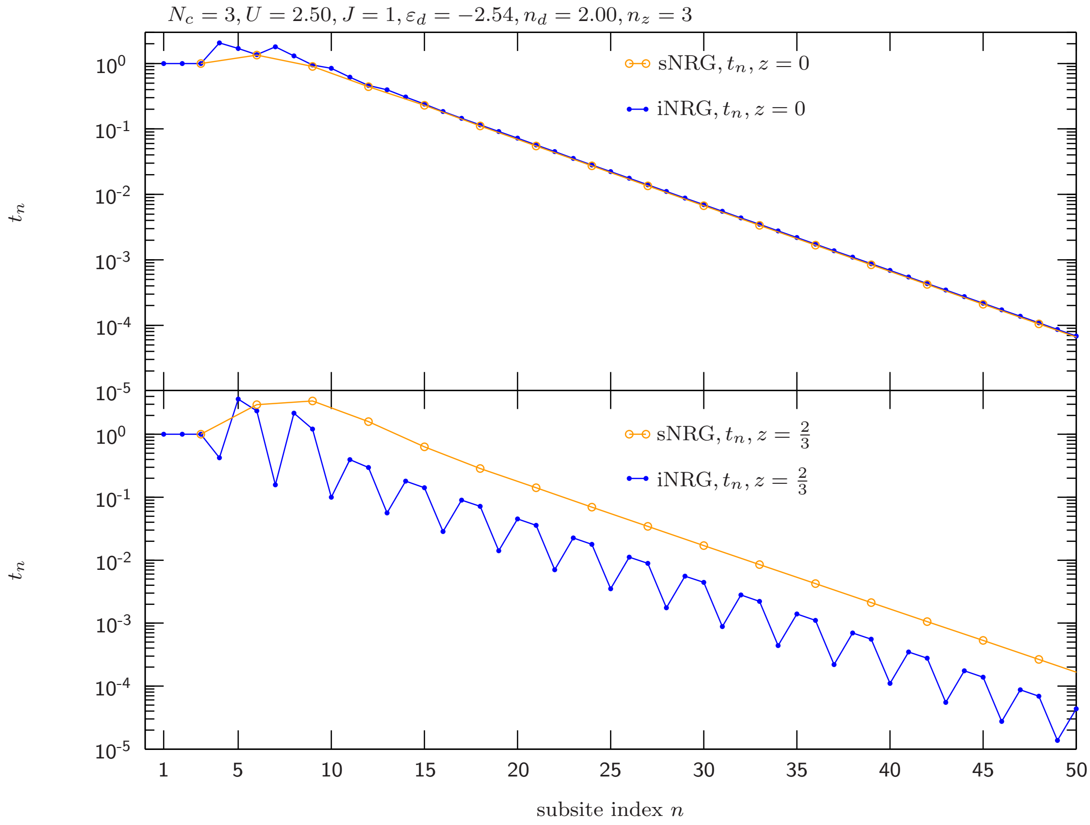

Figure 9.6.: Wilson chain couplings that leading to the spectral functions shown in figure 9.5. As for the couplings in figure 9.4 every third iNRG coupling for $z = \frac{2}{3}$ lies energetically considerably lower than the rest of the couplings.

9.3. Band symmetric three band Mott insulator transition (MIT)

We now turn to the band-symmetric MIT for a three band AHM. We choose the particle hole symmetric form of the AHM with $\varepsilon_d = -\frac{3}{4}J$, $U = \frac{J}{2}$ and arbitrary J, leading to half filling ($n_d = N_c = 3$). The results, shown in figure 9.7, show a that iNRG and sNRG match quite well here, although clearly larger differences than for the two band MIT with particle hole symmetry (see section 8.3) can be observed. But most importantly the iNRG spectral functions for different bands match very well. sNRG results for $J = 1.2$ and $J = 1.5$ are not available as unfortunately the calculations took too much time. For the iNRG results we find a critical J for the transition of $J_c^{iNRG} \simeq 1.2 \simeq \frac{2}{3}J_c^{N_c=2} \simeq \frac{1}{3}J_c^{N_c=1}$. J_c^{sNRG} is of the same magnitude but could not be determined due to the timeout the sNRG calculations.

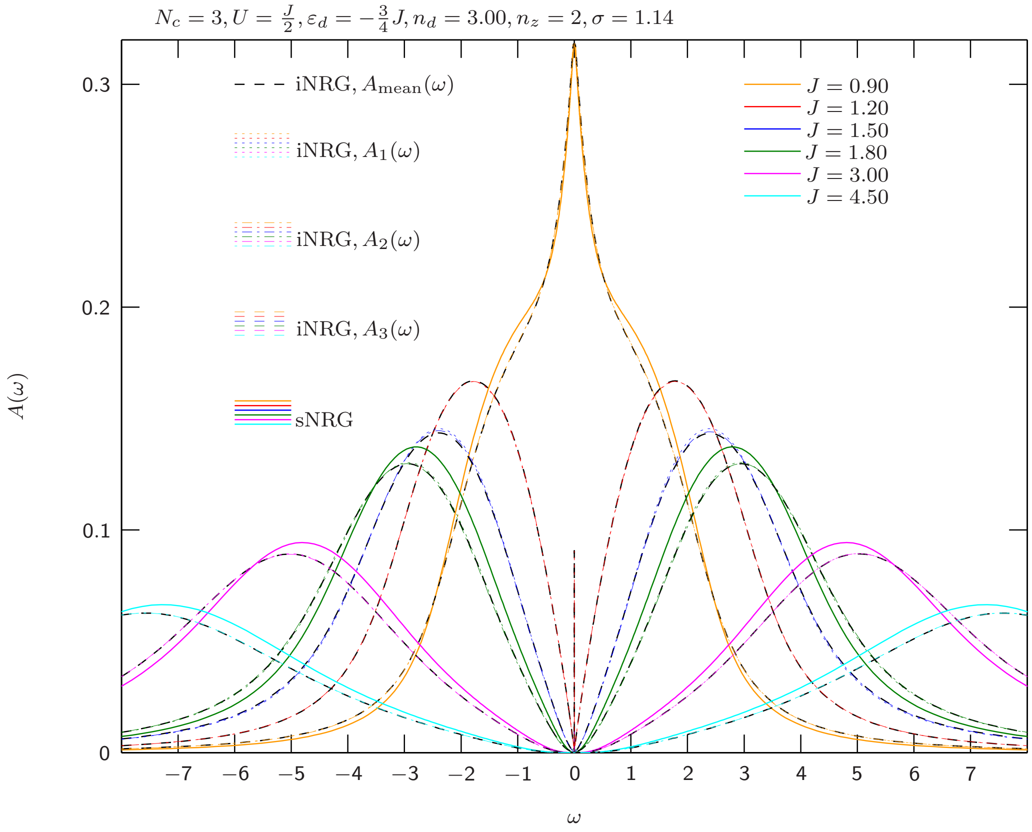

Figure 9.7.: Three band MIT with band- and particle-hole-symmetry. iNRG and sNRG results show the same tendencies, but also show clear differences. The iNRG spectral functions for different bands match very well. Unfortunately, the sNRG calculations for $J = 1.2$ and $J = 1.5$ took too much time and are therefore not available. The spectral functions for $J = 1.2$ are not fully converged. $J_c = 1.2$ can be found. Parameters: $T = 10^{-8}$, $\Lambda = 4$, $E_{trunc} = 7$, $N_{keep}^{max} = 3000$

9.4. Band-asymmetric three band results

In this section the three band Anderson Hund Model without band symmetry is examined. As for the two band calculations without band symmetry, $\varepsilon_{d,1/2/3}$ is not changed during DMFT iterations, unlike for the symmetric case. Good values for $\varepsilon_{d,1/2/3}$ are obtained by slightly varying the ε_d resulting from band symmetric calculations. We did not perform any sNRG calculations in the band asymmetric case, because the computational effort for sNRG is too big with no band symmetry to exploit in the diagonalization process.

For our first calculation, shown in figure 9.8, we take ε_d^{sym} from a band-symmetric calculation with half filling (n_d^{sym}=3), which has a symmetric spectral function. We then define $\delta\varepsilon_d \equiv 0.3 \cdot \varepsilon_d^{sym}$ and chose the band-asymmetric binding energies as $\varepsilon_{d,1} = \varepsilon_d^{sym} + \delta\varepsilon_d$, $\varepsilon_{d,2} = \varepsilon_d^{sym}$, $\varepsilon_{d,3} = \varepsilon_d^{sym} - \delta\varepsilon_d$. For the results we expect that $A_1(\omega) = A_3(-\omega)$ and $A_2(\omega) = A_2(-\omega)$ and $n_d = 3$. As shown in figure 9.8, the relations between the spectral functions are fulfilled only approximately, which is due to the unequal treatment of the spectral functions in terms of discretization in iNRG. $n_d = 2.99 \simeq 3$ is also only fulfilled approximately, but all in all the result seems quite reasonable. A second calculation with reversed band order with following averaging, as was done for the results in figure 8.12, might have yielded the expected filling n_d and the expected relations between the spectral functions of different bands, but was not performed. Between $10^{-8} < |\omega| < 10^{-7}$, we observe small swerves that may originate from the transition from a log-Gaussian to a regular Gaussian as broadening kernel, as already discussed for the results shown in figure 9.2. The DMFT convergence loop is initialized with a constant hybridization in the interval $[-1, 1]$, convergence is reached after 7 iterations with a maximum error in the spectral functions of 10^{-3}. After convergence 3 more iterations have been performed to ensure that convergence has indeed been reached. In figure 9.9, the results from different DMFT iterations are given, with the final result shown in figure 9.8 plotted in gray as a reference. Figure 9.10 shows the Wilson chain couplings that led to the spectral functions shown in figure 9.9, while the input for the Wilson chain couplings are of course the spectral functions obtained in the preceding DMFT iteration. For the first iteration an almost perfect logarithmic decay of the couplings can be observed, which are obtained from a constant hybridization. The couplings for all other DMFT iterations jump around between iNRG sites (different colors), calling truncation between the iNRG sites with $\alpha = 1$ and $\alpha = 2$ (green and red) into question. An overall logarithmic decay between supersites is still ensured though. The reason for the jumps between $\alpha = 1$ and $\alpha = 2$ sites is probably the small weight of $A_1(\omega)$ in the $\omega > 0$ regime respectively the small weight of $A_3(\omega)$ in the $\omega < 0$ regime. A modification in the discretization scheme used for frequency dependent hybridization functions (see section 5.2) might be able to generate logarithmic decay between iNRG sites, for example by altering $D_{1/3}^{+/-}$.

Our second band-asymmetric calculation is a Mott insulator transition, shown in figure 9.11. For the $\varepsilon_{d,1/2/3}$, a particle hole symmetric and band-symmetric Hamiltonian has been taken ($U = \frac{J}{2}, \varepsilon_d = -\frac{3}{4}J$). The band-symmetry was then broken by changing $\varepsilon_{d,1} = -\frac{3}{4}J - 0.1$ and $\varepsilon_{d,3} = -\frac{3}{4}J + 0.1$ but leaving $\varepsilon_{d,3} = -\frac{3}{4}J$, meaning the ε_d where changed symmetrically from the band-symmetric case. As discussed for the calculation shown in figure 9.8 before, the total filling n_d should then remain $n_d = 3$, as for the particle hole and band-symmetric case, while the spectral functions satisfy $A_1(\omega) = A_3(-\omega)$ and $A_3(\omega) = A_3(-\omega)$. As can be seen in figure 9.11, this is the case for our band-asymmetric Mott insulator transition, up to the height of the peak in the $J = 1.2$ case. All in all the band-asymmetric three band Mott insulator transition was very successful and looks very promising. The critical J is found to be $J_c \simeq 1.2$, which is about $\frac{2}{3}$ of the critical J found for the band-asymmetric Mott insulator transition for the two band model (see figure 8.14).

Our last band-asymmetric calculation performed has two degenerated bands with the same $\varepsilon_{d,2} = \varepsilon_{d,3}$, while for the first band an other $\varepsilon_{d,1} \neq \varepsilon_{d,2/3}$ is chosen. In principle, one could treat the first band as one iNRG site and the second together with the third band as a second iNRG site ($M_{iNRG} = 2$), allowing to implement and exploit the band symmetry of the degenerated bands rather than artificially breaking it with iNRG. As this scheme was not implemented yet in our program, this was not done and we interleaved all three bands ($M_{iNRG} = 3$), but took the average of the degenerated bands as input for the next DMFT iteration. The converged results of these calculations can be found in figure 9.12, where $\varepsilon_{d,2} = \varepsilon_{d,3} = -2.54$ remained constant and $\varepsilon_{d,1}$ was shifted from -1.02 in the first calculation to -4.07 in the last calculation. The results seem reasonable, and no big difference between $A_2(\omega)$ and $A_3(\omega)$ can be noticed. the non-degenerated spectral function $A_1(\omega)$ is forced almost completely into the $\omega > 0$ regime for $\varepsilon_{d,1} \gg \varepsilon_{d,2/3}$, while for $\varepsilon_{d,1} \ll \varepsilon_{d,2/3}$ the difference between the $\varepsilon_{d,1} \simeq \varepsilon_{d,2/3}$ spectral functions is not very big. Generally, one can observe that the spectral functions of the two degenerated band vary by much less than that of the non-degenerated band. One can also observe that the smaller $\varepsilon_{d,1}$ becomes, the larger its maximum value gets and the pointier it becomes.

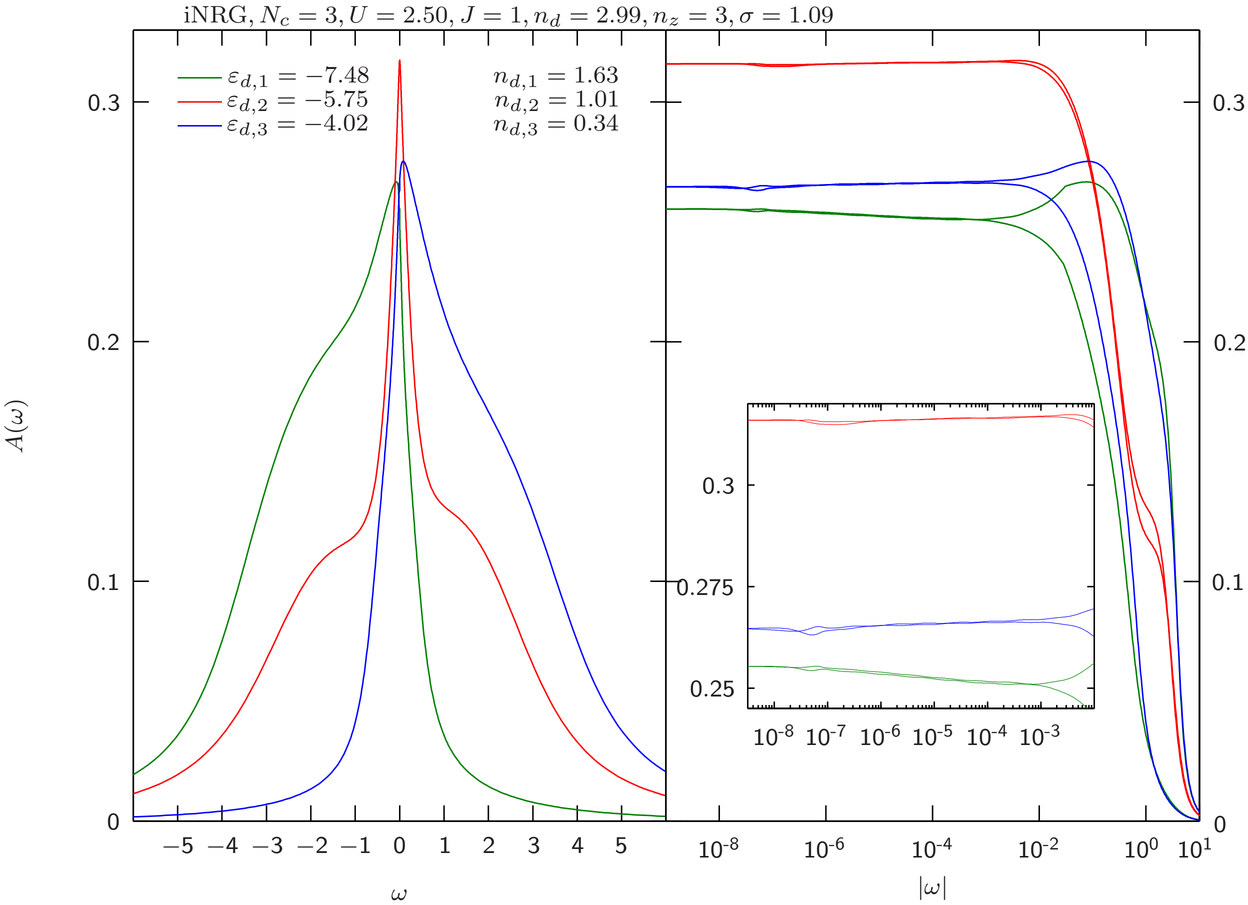

Figure 9.8.: Band-asymmetric three band iNRG + DMFT calculation. The small swerves at $10^{-8} < |\omega| < 10^{-7}$ probably arise from the transition from a log-Gaussian to a regular Gaussian as broadening kernel. As discussed in the text, $A_2(\omega) = A_2(-\omega)$, $A_1(\omega) = A_3(-\omega)$ and $n_d = 3$ should be preserved due to the construction of the $\varepsilon_{d,1/2/3}$, which is only approximately the case. Other than that the result looks very reasonable and promising. The corresponding couplings can be found in figure 9.10 and the course of the DMFT-convergence can be found in figure 9.9. Parameters: $T = 10^{-8}$, $\Lambda = 4$, $E_{trunc} = 7$, $N_{keep}^{max} = 3000$, $\delta\rho_{\text{disc}}^{\text{iNRG}} = 1.16 \cdot 10^{-4}$

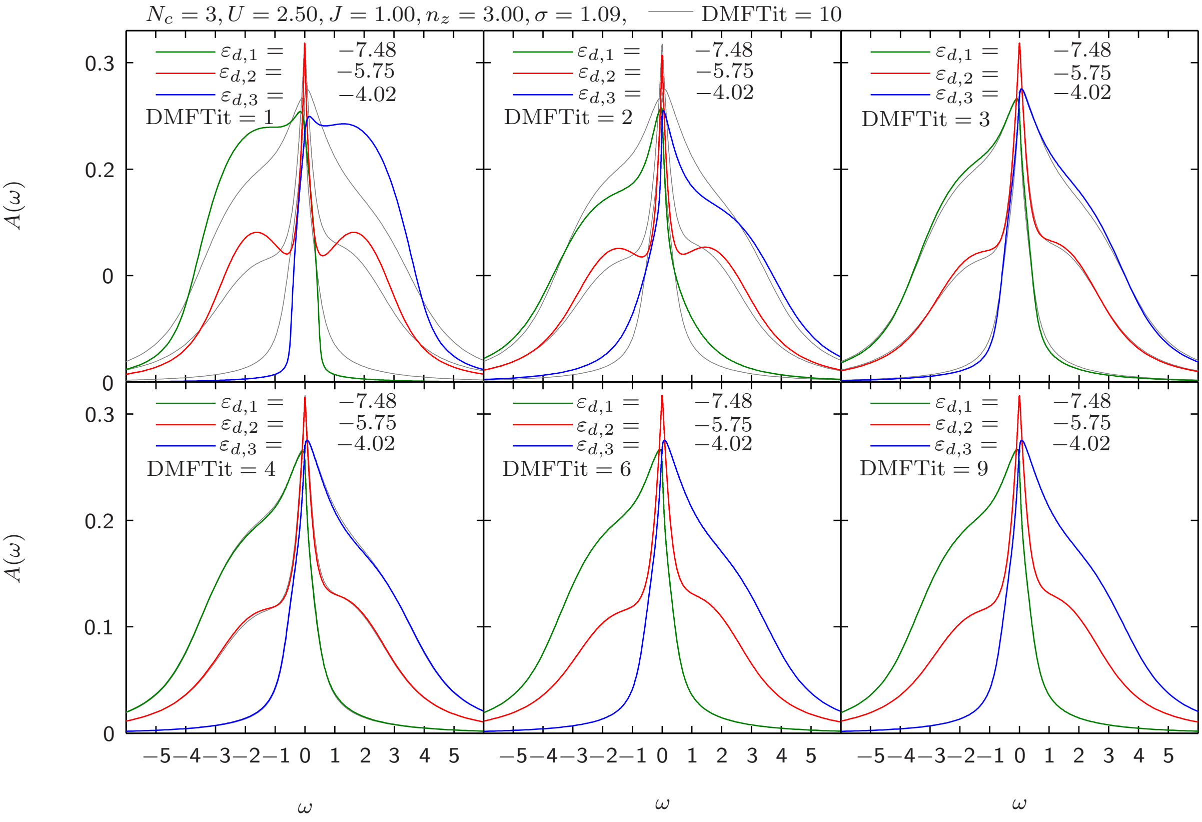

Figure 9.9.: DMFT-convergence corresponding to the final result shown in figure 9.8. The Wilson chain couplings that led to the presented spectral functions are shown in figure 9.10. DMFT-convergence is reached after 7 iterations for a maximum error in the spectral functions of less than $5 \cdot 10^{-3}$. After convergence 3 more iterations are performed to ensure the final result is truly converged.

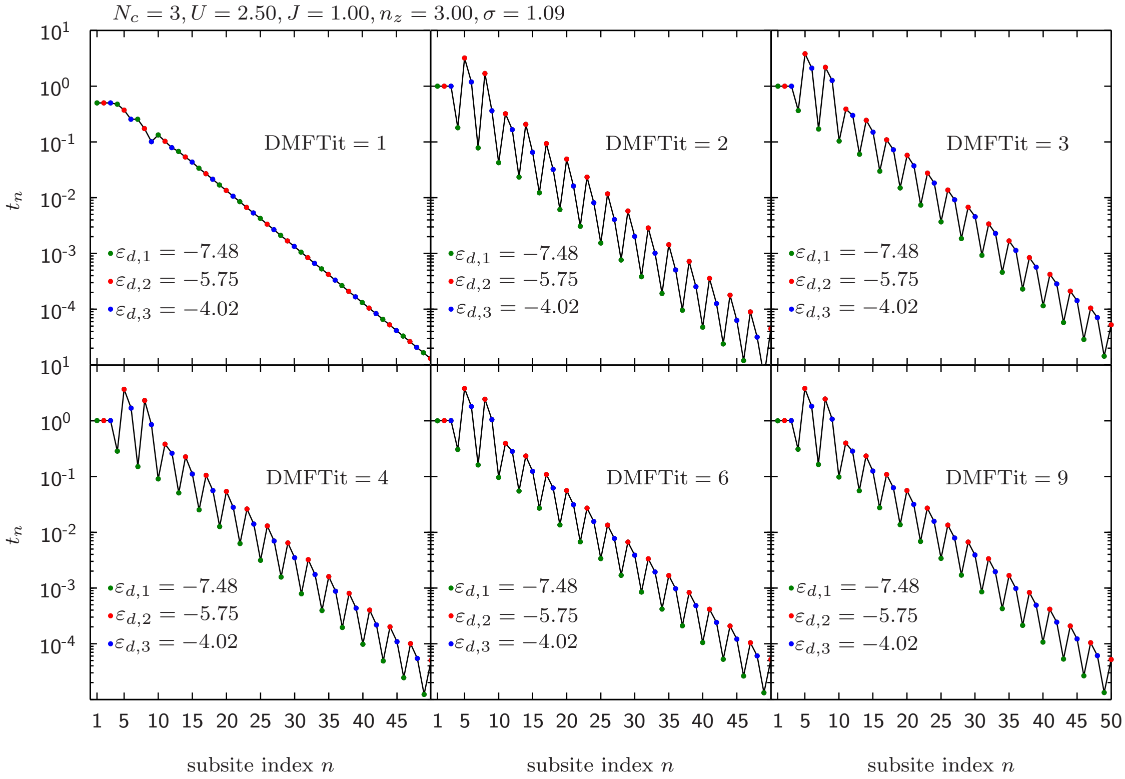

Figure 9.10.: Wilson chain couplings leading to the spectral functions shown in figure 9.9. The shift parameters z for these couplings was $\frac{2}{3}$. The couplings for the green sites lie energetically considerably lower than the other couplings, which was also observed for the couplings in figures 9.6 and 9.4. The couplings for DMFT iteration 1 are obtained from a constant hybridization and show the intended behavior.

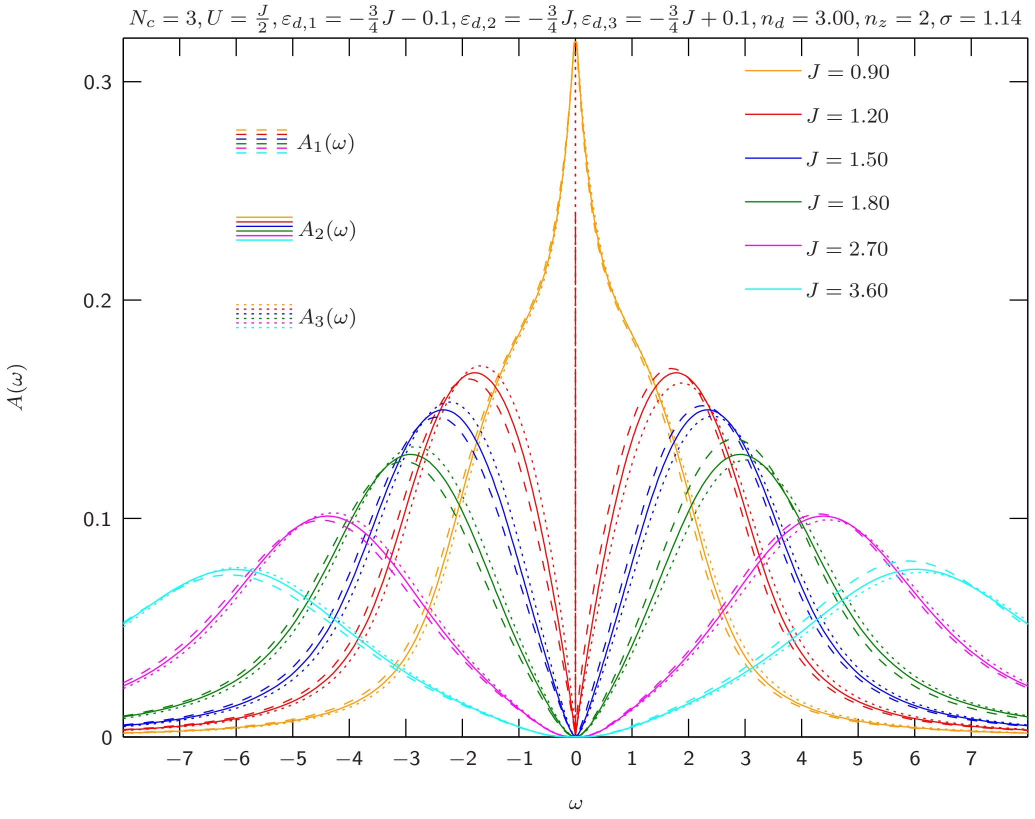

Figure 9.11.: Three band MIT without band-symmetry, calculated with iNRG. The results seem reasonable and are similar to the band-symmetric three band MIT results shown in figure 9.7. The spectral functions at $J = 1.2$ are not fully converged. Parameters: $T = 10^{-8}$, $\Lambda = 4$, $E_{trunc} = 7$, $N_{keep}^{max} = 3000$

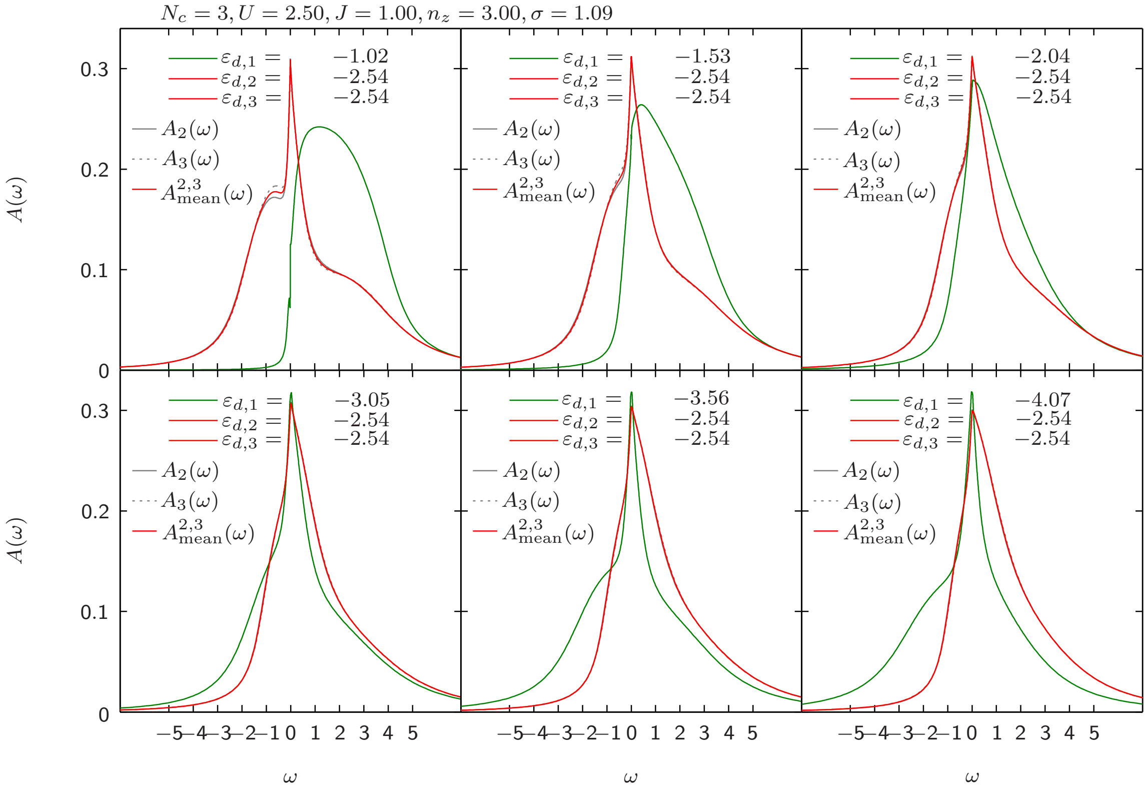

Figure 9.12.: Three band AHM results with two degenerated bands, calculated with iNRG. Degenerated bands were interleaved but averaged over in between DMFT iterations. The results seem reasonable, the spectral functions for different degenerated bands do not differ by much. For the non-degenerated band an increasing peak can be observed when lowering its binding energy $\varepsilon_{d,1}$. The Wilson chain couplings leading to these results can be found in figure 9.13 Parameters: $T = 10^{-8}$, $\Lambda = 4$, $E_{trunc} = 7$, $N^{max}_{keep} = 3000$, $\delta\rho^{\text{iNRG}}_{\text{disc}} \simeq 7 \cdot 10^{-5}$

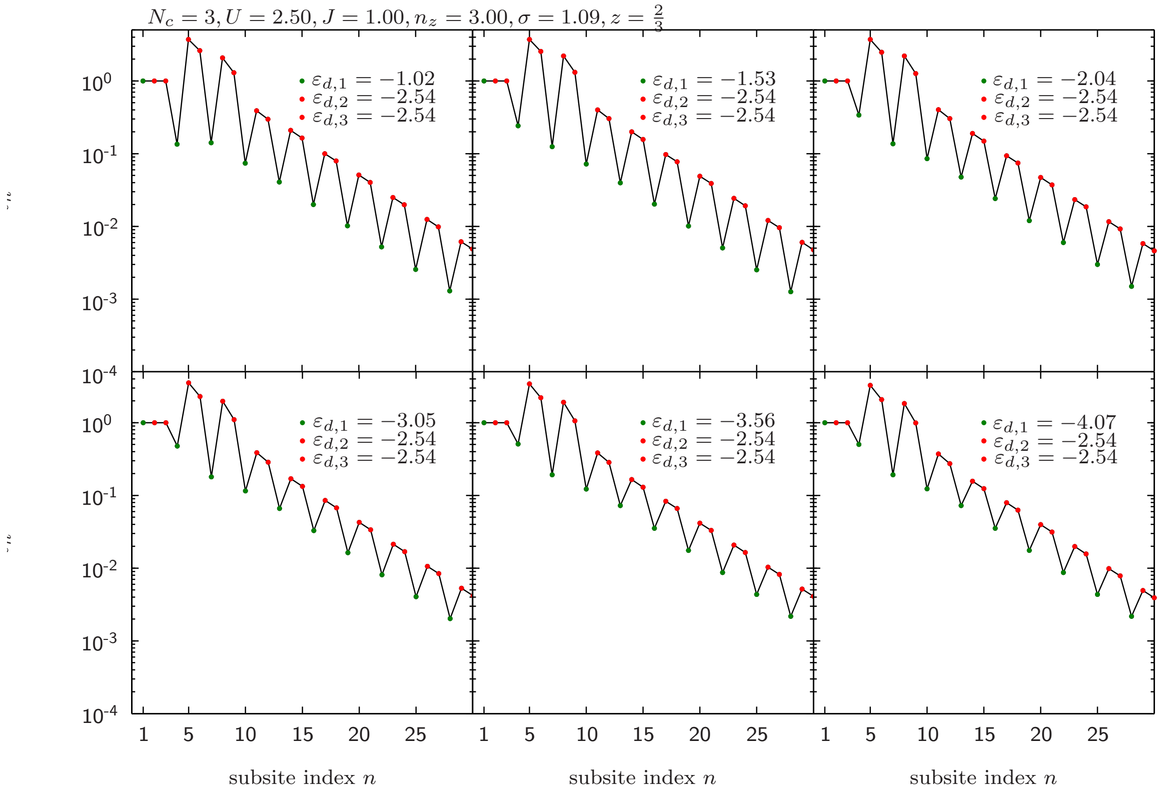

Figure 9.13.: Wilson chain couplings for $z = \frac{2}{3}$ leading to the spectral functions in figure 9.12. The couplings show an overall logarithmic decay but the green couplings lie energetically lower than the other couplings, as could already been observed for other couplings with $z = \frac{2}{3}$.

10. Conclusion and outlook

In this thesis we tested the interleaved Numerical Renormalization Group as an impurity solver for the Dynamical Mean Field Theory. As a reference for the quality and efficiency of our iNRG calculations we compared them to corresponding sNRG calculations.
For a first quality check we used a one-band Anderson Hund Model. Here, iNRG yielded very good results. Especially when $n_z = 3$ z-shifts were used, no differenced between iNRG and sNRG calculations could be observed. However, when the number of z-shifts was further increased to $n_z = 8$, a worsening of the iNRG results compared to calculations with a lesser amount of z-shifts could be observed. This means that the z-averaging procedure in iNRG has to be further improved to allow more accurate iNRG calculations. The one-band Mott insulator transition revealed first problems when using iNRG. In the insulating state no acceptable iNRG results could be obtained. In this case the artificial SU(2)-spin symmetry breaking might be problematic.
For a second test the two-band Anderson Hund model was used. Presumably due to an increase in the discretization factor Λ, deviations between sNRG and iNRG were larger than for the one band model, but most of the iNRG results were still quite good. Here, too, iNRG showed problems in some calculations yielding insulating results, which might be either due to the artificial breaking of the band-symmetry in these iNRG calculations or problems with the discretization scheme. Our results for two- and three-band models indicate that iNRG might have general problems if the hybridization function has a lot of weight far away from the Fermi-level where the logarithmic discretization yields a very bad resolution. This should be further examined and modifications to the logarithmic discretization scheme might be needed to further improve the outcome of iNRG calculations. It should be emphasized that this was not generally the case as also insulating iNRG results with almost perfect accordance to corresponding sNRG results could be achieved. In band-asymmetric calculations iNRG and sNRG showed rather large discrepancies. It can be assumed that these discrepancies arise from an unequal treatment of the bands in terms of the discretization, a larger amount of z-shifts might reduce these differences. Further improvements in the discretization scheme and the z-averaging process might help here. From an efficiency point of few, iNRG was superior to sNRG in two-band calculations, as it was up to 4.5 times faster.
Last but not least the three-band Anderson Hund model was used to test iNRG as an impurity solver for multi-band DMFT calculations. We first tested band-symmetric models which are also accessible for sNRG. Probably due to the further increase in Λ, discrepancies grew even larger than for two-band calculations but where still promising. Here, problems with the iNRG Wilson chain couplings when z-shifting is applied were revealed. The Wilson chain couplings for every third iNRG sites were systematically smaller than the rest of the couplings. An altered, more systematic scheme to determine

the band edges might help here. For iNRG major benefits in the computation time could be observed, as it took only 16 minutes for iNRG per DMFT iteration as opposed to 170 minutes for sNRG. The band-asymmetric three band calculations were only calculated with iNRG as sNRG calculations are too costly here without being able to exploit full channel symmetry. iNRG yielded converged results here.

To conclude, iNRG seems a very promising method for multi-band DMFT applications, especially for low symmetry models which are computationally very costly when calculated with sNRG. However, further improvements have to be made in the discretization process and the z-averaging procedure to get more accurate results. With this in mind four- or even five-band models seem to accessible with iNRG + DMFT in the near future, yielding accurate results at low temperatures and high resolution at the Fermi-level.

Part III.

Appendix

A. Basics of quantum many-particle theory

In this appendix a short overview of the most important relations of quantum many-particle theory used in this thesis is given. For a more detailed discussion I refer to [2] and [9].
In this thesis only retarded Green's functions are used. When Green's functions appear or are referred to we always mean the retarded Green's function, defined as

$$\langle\langle A, B\rangle\rangle_t = -i\Theta(t)\,\langle[A(t), B]_+\rangle_T\,, \tag{A.1}$$

where Θ is the step function, $[\dots]_+$ is the anticommutator and $\langle\dots\rangle_T$ is the thermal average in the grand canonical ensemble. $A(t) = e^{iHt}Ae^{-iHt}$ is the operator A time evolved in the Heisenberg picture, with Hamilton operator H. The equation of motion for the operator A in the Heisenberg picture is

$$\frac{dA(t)}{dt} = i[H, A(t)]_- \tag{A.2}$$

with commutator $[\dots]_-$. An equation of motion for $\langle\langle A, B\rangle\rangle_t$ is obtained by simply taking the time derivative:

$$\begin{aligned}\frac{d}{dt}\langle\langle A, B\rangle\rangle_t &= -i\delta(t)\,\langle[A, B]_+\rangle_T - \Theta(t)\,\langle[[A(t), H]_-, B]_+\rangle_T \\ &= -i\delta(t)\,\langle[A, B]_+\rangle_T - i\,\langle\langle[A, H]_-, B\rangle\rangle_t\end{aligned} \tag{A.3}$$

The equation of motion can be fourier transformed into frequency space where it becomes an algebraic equation. With the fourier transformation of the Green's function defined as

$$\begin{aligned}\langle\langle A, B\rangle\rangle_\omega &= \int_{-\infty}^{\infty} dt \quad \langle\langle A, B\rangle\rangle_t\, e^{i\omega t} \\ \langle\langle A, B\rangle\rangle_t &= \int_{-\infty}^{\infty} \frac{d\omega}{2\pi} \quad \langle\langle A, B\rangle\rangle_\omega\, e^{-i\omega t}\end{aligned} \tag{A.4}$$

the equation of motion in frequency space becomes

$$\omega\,\langle\langle A, B\rangle\rangle_\omega = \langle[A, B]_+\rangle_T + \langle\langle[A, H]_-, B\rangle\rangle_\omega \quad . \tag{A.5}$$

The spectral function is defined as

$$A_{A,B}(t) = \frac{1}{2\pi}\,\langle[A(t), B]_+\rangle \quad . \tag{A.6}$$

It is usually also transformed in frequency space and is basically the imaginary part of the Green's function:

$$A_{A,B}(\omega) = -\frac{1}{\pi}\mathrm{Im}(\langle\langle A, B\rangle\rangle_{\omega}) \tag{A.7}$$

B. Calculation of the Lattice Green's Function

Here we derive the frequency dependent lattice Green's function $\langle\langle c_k, c_k^\dagger \rangle\rangle_\omega$ for the lattice model in section 2.3, equation (2.12):

$$H_{latt} = \sum_{k \in 1.BZ} (\varepsilon_k - \mu) c_k^\dagger c_k + \sum_i H_i^{int} \equiv \sum_{k \in 1.BZ} (\varepsilon_k - \mu) c_k^\dagger c_k + H_{int} \tag{B.1}$$

We use the equation of motion in frequency space,

$$\omega \langle\langle c_k, c_k^\dagger \rangle\rangle_\omega = \langle [c_k, c_k^\dagger]_+ \rangle_T + \langle\langle [c_k, H_{latt}]_-, c_k^\dagger \rangle\rangle_\omega \tag{B.2}$$

Where $\langle \ldots \rangle_T$ is the thermal average in the grand canonical ensemble and $[\ldots]_{+/-}$ is the anticommutator/commutator. The term $\langle [c_k, c_k^\dagger]_+ \rangle_T = 1$ is easily seen while for $\langle\langle [c_k, H_{latt}]_-, c_k^\dagger \rangle\rangle_\omega$ we need an expression for $[c_k, H_{latt}]_-$:

$$[c_k, H_{latt}]_- = \sum_{\tilde{k}} \varepsilon_{\tilde{k}} [c_k, c_{\tilde{k}}^\dagger c_{\tilde{k}}]_- + [c_k, H_{int}]_- = \varepsilon_k c_k + [c_k, H_{int}]_- \quad , \tag{B.3}$$

which is obtained by inserting the following expression:

$$\begin{aligned} [c_k, c_{\tilde{k}}^\dagger c_{\tilde{k}}]_- &= c_k c_{\tilde{k}}^\dagger c_{\tilde{k}} - c_{\tilde{k}}^\dagger c_{\tilde{k}} c_k \\ &= c_k c_{\tilde{k}}^\dagger c_{\tilde{k}} - c_{\tilde{k}}^\dagger c_{\tilde{k}} c_k + c_{\tilde{k}}^\dagger c_k c_{\tilde{k}} - c_{\tilde{k}}^\dagger c_k c_{\tilde{k}} \\ &= [c_{\tilde{k}}^\dagger, c_k]_+ c_{\tilde{k}} - c_{\tilde{k}}^\dagger [c_{\tilde{k}}, c_k]_+ = \delta_{k,\tilde{k}} c_k \end{aligned} \tag{B.4}$$

We therefore get

$$\begin{aligned} \langle\langle [c_k, H_{latt}]_-, c_k^\dagger \rangle\rangle_\omega &= \varepsilon_k \langle\langle c_k, c_k^\dagger \rangle\rangle_\omega + \langle\langle [c_k, H_{int}]_-, c_k^\dagger \rangle\rangle_\omega \\ &= \varepsilon_k \langle\langle c_k, c_k^\dagger \rangle\rangle_\omega + \Sigma_{latt}(k,\omega) \langle\langle c_k, c_k^\dagger \rangle\rangle_\omega \quad , \end{aligned} \tag{B.5}$$

where we have inserted the definition for the self-energy for the interacting part of the Green's function. When we insert this into equation (B.2), we get

$$\langle\langle c_k, c_k^\dagger \rangle\rangle_\omega = \frac{1}{\omega - \varepsilon_k + \mu - \Sigma_{latt}(k,\omega)} \tag{B.6}$$

C. Calculation of the Impurity Green's Function

In this appendix we derive an expression for the impurity Green's function $\langle\langle d, d^\dagger\rangle\rangle_\omega$ for the impurity model in equation (2.19),

$$\begin{aligned} H_{imp} &= (\varepsilon_d - \mu)d^\dagger d + H_{int}^{imp} \\ H_{bath} &= \sum_{k\in 1.BZ} (\varepsilon_k - \mu)c_k^\dagger c_k \\ H_{hyb} &= \sum_{k\in 1.BZ} V_k(d^\dagger c_k + c_k^\dagger d) \\ H &= H_{imp} + H_{bath} + H_{hyb} \end{aligned} \tag{C.1}$$

We use the equation of motion for the Green's function in frequency space,

$$\begin{aligned} \omega\,\langle\langle d, d^\dagger\rangle\rangle_\omega &= \langle[d, d^\dagger]_+\rangle_T + \langle\langle[d, H]_-, d^\dagger\rangle\rangle_\omega \\ &= 1 + \langle\langle[d, H_{imp}]_-, d^\dagger\rangle\rangle_\omega + \langle\langle[d, H_{bath}]_-, d^\dagger\rangle\rangle_\omega + \langle\langle[d, H_{hyb}]_-, d^\dagger\rangle\rangle_\omega \quad , \end{aligned} \tag{C.2}$$

where we need the following commutator relations to calculate $\langle\langle[d, H]_-, d^\dagger\rangle\rangle_\omega$:

$$[d, d^\dagger d]_- = [d, d^\dagger]_+ d - d^\dagger[d, d]_+ = d \tag{C.3}$$

$$[d, c_k^\dagger c_k]_- = [d, c_k^\dagger]_+ c_k - c_k^\dagger[d, c_k]_+ = 0 \tag{C.4}$$

$$[d, c_k^\dagger d]_- = [d, c_k^\dagger]_+ d - d_k^\dagger[d, d]_+ = 0 \tag{C.5}$$

$$[d, d^\dagger c_k]_- = [d, d^\dagger]_+ c_k - d^\dagger[d, c_k]_+ = c_k \tag{C.6}$$

We now get expressions for the Green's functions in equation (C.2) $\langle\langle[d, H]_-, d^\dagger\rangle\rangle_\omega$ is built from:

$$\begin{aligned} \langle\langle[d, H_{imp}]_-, d^\dagger\rangle\rangle_\omega &= \varepsilon_d\,\langle\langle[d, d^\dagger d]_-, d^\dagger\rangle\rangle_\omega + \langle\langle[d, H_{int}^{imp}]_-, d^\dagger\rangle\rangle_\omega \\ &= \varepsilon_d\,\langle\langle d, d^\dagger\rangle\rangle_\omega + \Sigma_{imp}(\omega)\,\langle\langle d, d^\dagger\rangle\rangle_\omega \end{aligned} \tag{C.7}$$

$$\langle\langle[d, H_{bath}]_-, d^\dagger\rangle\rangle_\omega = 0 \tag{C.8}$$

$$\begin{aligned} \langle\langle[d, H_{hyb}]_-, d^\dagger\rangle\rangle_\omega &= \sum_{k\in 1.BZ} V_k\bigg(\langle\langle[d, d^\dagger c_k]_-, d^\dagger\rangle\rangle_\omega + \langle\langle[d, c_k^\dagger d]_-, d^\dagger\rangle\rangle_\omega\bigg) \\ &= \sum_{k\in 1.BZ} V_k\,\langle\langle c_k, d^\dagger\rangle\rangle_\omega \end{aligned} \tag{C.9}$$

The Green's function $\langle\langle c_k, d^\dagger\rangle\rangle_\omega$ can be expressed in terms of $\langle\langle d, d^\dagger\rangle\rangle_\omega$ via the equation of motion:

$$\begin{aligned}\omega\,\langle\langle c_k, d^\dagger\rangle\rangle_\omega &= \langle[c_k, d^\dagger]_+\rangle_T + \langle\langle[c_k, H]_-, d^\dagger\rangle\rangle_\omega \\ &= \langle\langle[c_k, H]_-, d^\dagger\rangle\rangle_\omega\end{aligned} \tag{C.10}$$

We need to calculate the commutator $[c_k, H]_-$:

$$[c_k, H]_- = [c_k, H_{imp}]_- + [c_k, H_{bath}]_- + [c_k, H_{hyb}]_- \tag{C.11}$$

It can easily be seen that

$$[c_k, H_{imp}]_- = 0 \tag{C.12}$$

as $[c_k, H_{imp}]_-$ can be expressed in terms of anticommutators of c_k and $d^{(\dagger)}$. As c_k and $d^{(\dagger)}$ annticommute, equation (C.12) follows. The other two commutators in equation (C.11) are also easily obtained:

$$[c_k, H_{bath}]_- = \sum_{\tilde{k}\in 1.BZ} \varepsilon_{\tilde{k}}[c_k, c^\dagger_{\tilde{k}} c_{\tilde{k}}]_- \overset{Eq.(\mathrm{B.4})}{=} \varepsilon_k c_k \tag{C.13}$$

$$\begin{aligned}[c_k, H_{hyb}]_- &= \sum_{\tilde{k}\in 1.BZ} V_{\tilde{k}}\Big([c_k, d^\dagger c_{\tilde{k}}]_- + [c_k, c^\dagger_{\tilde{k}} d]_-\Big) \\ &= \sum_{\tilde{k}\in 1.BZ} V_{\tilde{k}}\delta_{k,\tilde{k}} d = V_k d\end{aligned} \tag{C.14}$$

We can now insert those expressions into equation (C.10),

$$\omega\,\langle\langle c_k, d^\dagger\rangle\rangle_\omega = \varepsilon_k\,\langle\langle c_k, d^\dagger\rangle\rangle_\omega + V_k\,\langle\langle d, d^\dagger\rangle\rangle_\omega \tag{C.15}$$

$$\langle\langle c_k, d^\dagger\rangle\rangle_\omega = \frac{V_k}{\omega - \varepsilon_k}\,\langle\langle d, d^\dagger\rangle\rangle_\omega \tag{C.16}$$

and insert the expression for $\langle\langle c_k, d^\dagger\rangle\rangle_\omega$ into equation (C.9).

$$\langle\langle[d, H_{hyb}]_-, d^\dagger\rangle\rangle_\omega = \sum_{k\in 1.BZ} \frac{V_k^2}{\omega - \varepsilon_k}\,\langle\langle d, d^\dagger\rangle\rangle_\omega \tag{C.17}$$

By inserting equations (C.7), (C.8) and (C.17) into equation (C.2), we arrive at an expression for $\langle\langle d, d^\dagger\rangle\rangle_\omega$:

$$\begin{aligned}\langle\langle d, d^\dagger\rangle\rangle_\omega &= \frac{1}{\omega - \varepsilon_d + \mu - \sum_k \frac{V_k^2}{\omega-\varepsilon_k} - \Sigma_{imp}(\omega)} \\ &= \frac{1}{\omega - \varepsilon_d + \mu - \Delta(\omega) - \Sigma_{imp}(\omega)}\quad,\end{aligned} \tag{C.18}$$

where $\Delta(\omega)$ is the hybridization function defined as

$$\Delta(\omega) \equiv \sum_{k\in 1.BZ} \frac{V_k^2}{\omega - \varepsilon_k}. \tag{C.19}$$

D. NRG transformation

D.1. Hamiltonian

$$H = H_{imp} + H_{bath} + H_{hyb}$$

H_{imp}: Impurity Hamiltonian, small dimension, must be exactly diagonalizable. $d_i^{(\dagger)}$ are the annihilation (creation) operators of impurity states $|i\rangle$. The exact form of H_{imp} is arbitrary.
H_{bath}: bath Hamiltonian, must be non-interacting and can thus be written as:

$$H_{bath} = \sum_{\substack{k\in 1.BZ\\ \nu}} \varepsilon_{k,\nu} c^\dagger_{k,\nu} c_{k,\nu}$$

$c_{k,\nu}^{(\dagger)}$ are annihilation (creation) operators of bath electron states $|k,\nu\rangle$ with momentum k and of type ν , which is a combination of bath and spin index. $\varepsilon_{k,\nu}$ is the dispersion relation of bath electrons of type ν. $\varepsilon_{k,\nu} \in [D_\nu^-, D_\nu^+]$, $D_\nu^- < 0$ and $D_\nu^+ > 0$, the chemical potential is set to 0.
H_{hyb}: Hybridization of bath and impurity, describes hopping from bath to impurity and vice versa:

$$H_{hyb} = \sum_{\substack{k\in 1.BZ\\ \nu,i}} V_k^{\nu,i} \Big(d_i^\dagger c_{k,\nu} + c_{k,\nu}^\dagger d_i \Big)$$

$V_k^{\nu,i}$ is the hopping amplitude between impurity states $|i\rangle$ and bath states $|k,\nu\rangle$.

D.2. Logarithmic Discretization

The energy-axis of each band ν is now discretized with exponentially increasing resolution near the chemical potential. For that we first define: $D_\nu = min\{|D_\nu^-|, |D_\nu^+|\}$ and a discretization factor $\Lambda > 1$. We now define energy intervals $I_{n,\nu}^\lambda$ with $\lambda \in \{+,-\}$ and $n \in \mathbb{N}$:

$$I_{1,\nu}^- = [D_\nu^-, -D_\nu \Lambda^{-1}); \quad n > 1: \quad I_{n,\nu}^- = [-D_\nu \Lambda^{-n+1}, -D_\nu \Lambda^{-n})$$

$$I_{1,\nu}^+ = (D_\nu \Lambda^{-1}, D_\nu^+]; \quad n > 1: \quad I_{n,\nu}^+ = (D_\nu \Lambda^{-n}, D_\nu \Lambda^{-n+1}]$$

For n>1 one has $|I_{n,\nu}^\lambda| = D_\nu \Lambda^{-n}(\Lambda - 1) \sim \Lambda^{-n}$.
The Hamiltonian has now the following form:

$$H = H_{imp} + \sum_{n,\lambda} \sum_{\nu} \sum_{\substack{k\in 1.BZ\\ \varepsilon_{k,\nu}\in I_{n,\nu}^\lambda}} \varepsilon_{k,\nu} c^\dagger_{k,\nu} c_{k,\nu} + \sum_{n,\lambda} \sum_{\nu,i} \sum_{\substack{k\in 1.BZ\\ \varepsilon_{k,\nu}\in I_{n,\nu}^\lambda}} V_k^{\nu,i} \Big(d_i^\dagger c_{k,\nu} + c_{k,\nu}^\dagger d_i \Big)$$

D.3. First Transformation

As we are interested in the effect of the impurity, we do not want to approximate the Hybridization term. We will now search for a basis of the bath states in which only one bath state per interval $I^{\lambda}_{n,\nu}$ couples to the impurity. For that we construct an orthogonal transformation $O^{n,\lambda,\nu}_{k,p,i}$ with $p \in \mathbb{Z}$ and the following properties:

$$\sum_{p,i} O^{n,\lambda,\nu}_{k,p,i} O^{n,\lambda,\nu}_{\tilde{k},p,i} = \delta_{k,\tilde{k}}$$

$$\sum_{\substack{k \in 1.BZ \\ \varepsilon_{k,\nu} \in I^{\lambda}_{n,\nu}}} O^{n,\lambda,\nu}_{k,p,i} O^{n,\lambda,\nu}_{k,\tilde{p},\tilde{i}} = \delta_{p,\tilde{p}} \delta_{i,\tilde{i}}$$

We now define a new basis with annihilation operators $a^{n,\lambda,\nu}_{p,i}$:

$$a^{n,\lambda,\nu}_{p,i} = \sum_{\substack{k \in 1.BZ \\ \varepsilon_{k,\nu} \in I^{\lambda}_{n,\nu}}} O^{n,\lambda,\nu}_{k,p,i} c_{k,\nu}$$

If the impurity should couple only to one of those states, i.e. the state with p=0, one has $V^{\nu,i}_k = \gamma^{\nu,i}_{n,\lambda} O^{n,\lambda,\nu}_{k,0,i}$ with $(\gamma^{\nu,i}_{n,\lambda})^2 = \sum_{\substack{k \in 1.BZ \\ \varepsilon_{k,\nu} \in I^{\lambda}_{n,\nu}}} |V^{\nu,i}_k|^2$. As the length of the intervals $I^{\lambda}_{n,\nu}$ is $\sim \Lambda^{-n}$, $\gamma^{\nu,i}_{n,\lambda} \sim \Lambda^{-\frac{n}{2}}$, if $V^{\nu,i}_k$ is of the same scale for all intervals. The Hybridization then has the following form:

$$\begin{aligned}
H_{hyb} &= \sum_{n,\lambda} \sum_{\nu,i} \sum_{\substack{k \in 1.BZ \\ \varepsilon_{k,\nu} \in I^{\lambda}_{n,\nu}}} V^{\nu,i}_k \Big(d^{\dagger}_i \sum_{p,\tilde{i}} O^{n,\lambda,\nu}_{k,p,\tilde{i}} a^{n,\lambda,\nu}_{p,\tilde{i}} + h.c. \Big) \\
&= \sum_{n,\lambda} \sum_{\nu,i} \sum_{p,\tilde{i}} \gamma^{\nu,i}_{n,\lambda} \Big(d^{\dagger}_i \delta_{p,0} \delta_{i,\tilde{i}} a^{n,\lambda,\nu}_{p,\tilde{i}} + h.c. \Big) \\
&= \sum_{n,\lambda} \sum_{\nu,i} \gamma^{\nu,i}_{n,\lambda} \Big(d^{\dagger}_i a^{n,\lambda,\nu}_{0,i} + h.c. \Big) \\
&= \sum_{n,\lambda} \sum_{\nu,i} \gamma^{\nu,i}_{n,\lambda} \Big(d^{\dagger}_i a^{n,\lambda,\nu}_{i} + h.c. \Big)
\end{aligned}$$

with $a^{n,\lambda,\nu}_{0,i} \equiv a^{n,\lambda,\nu}_{i}$.
The bath Hamiltonian transforms as follows:

$$\begin{aligned}
H_{bath} &= \sum_{n,\lambda} \sum_{\nu} \sum_{\substack{k \in 1.BZ \\ \varepsilon_{k,\nu} \in I^{\lambda}_{n,\nu}}} \varepsilon_{k,\nu} \sum_{p,i} O^{n,\lambda,\nu}_{k,p,i} (a^{n,\lambda,\nu}_{p,i})^{\dagger} \sum_{\tilde{p},\tilde{i}} O^{n,\lambda,\nu}_{k,\tilde{p},\tilde{i}} a^{n,\lambda,\nu}_{\tilde{p},\tilde{i}} \\
&= \underbrace{\sum_{n,\lambda} \sum_{\nu} \sum_{\substack{k \in 1.BZ \\ \varepsilon_{k,\nu} \in I^{\lambda}_{n,\nu}}} \sum_{i} \varepsilon_{k,\nu} |O^{n,\lambda,\nu}_{k,0,i}|^2 (a^{n,\lambda,\nu}_{0,i})^{\dagger} a^{n,\lambda,\nu}_{0,i}}_{(1)}
\end{aligned}$$

$$\underbrace{+\sum_{n,\lambda}\sum_{\nu}\sum_{\substack{k\in 1.BZ\\ \varepsilon_{k,\nu}\in I^{\lambda}_{n,\nu}}}\sum_{\substack{p\\ p\neq 0}}\sum_{i}\varepsilon_{k,\nu}|O^{n,\lambda,\nu}_{k,p,i}|^2(a^{n,\lambda,\nu}_{p,i})^\dagger a^{n,\lambda,\nu}_{p,i}}_{(2)}$$

$$\underbrace{+\sum_{n,\lambda}\sum_{\nu}\sum_{\substack{k\in 1.BZ\\ \varepsilon_{k,\nu}\in I^{\lambda}_{n,\nu}}}\sum_{\substack{p,\tilde p\\ p\neq \tilde p}}\sum_{\substack{i,\tilde i\\ i\neq \tilde i}}\varepsilon_{k,\nu}O^{n,\lambda,\nu}_{k,p,i}O^{n,\lambda,\nu}_{k,\tilde p,\tilde i}(a^{n,\lambda,\nu}_{p,i})^\dagger a^{n,\lambda,\nu}_{\tilde p,\tilde i}}_{(3)}$$

(1) contains all states that interact directly with the impurity. The states in (2) only interact indirectly with the impurity via (3). If the intervals $I^{\lambda}_{n,\nu}$ are not too big, one gets $\varepsilon_{k,\nu} \simeq \varepsilon_\nu \equiv const.$ and therefore:

$$\sum_{\substack{k\in 1.BZ\\ \varepsilon_{k,\nu}\in I^{\lambda}_{n,\nu}}}\sum_{\substack{p,\tilde p\\ p\neq \tilde p}}\sum_{\substack{i,\tilde i\\ i\neq \tilde i}}\varepsilon_{k,\nu}O^{n,\lambda,\nu}_{k,p,i}O^{n,\lambda,\nu}_{k,\tilde p,\tilde i}(a^{n,\lambda,\nu}_{p,i})^\dagger a^{n,\lambda,\nu}_{\tilde p,\tilde i}$$

$$\simeq \varepsilon_\nu \sum_{\substack{k\in 1.BZ\\ \varepsilon_{k,\nu}\in I^{\lambda}_{n,\nu}}}\sum_{\substack{p,\tilde p\\ p\neq \tilde p}}\sum_{\substack{i,\tilde i\\ i\neq \tilde i}}O^{n,\lambda,\nu}_{k,p,i}O^{n,\lambda,\nu}_{k,\tilde p,\tilde i}(a^{n,\lambda,\nu}_{p,i})^\dagger a^{n,\lambda,\nu}_{\tilde p,\tilde i}$$

$$= \varepsilon_\nu \sum_{\substack{p,\tilde p\\ p\neq \tilde p}}\sum_{\substack{i,\tilde i\\ i\neq \tilde i}}\delta_{p,\tilde p}\delta_{i,\tilde i}(a^{n,\lambda,\nu}_{p,i})^\dagger a^{n,\lambda,\nu}_{\tilde p,\tilde i} = 0$$

Because of that we will neglect (3) and as (2) then does not couple to the impurity at all we will also neglect (2). With the definition: $\xi^{n,\lambda}_{i,\nu} = \sum_{\substack{k\in 1.BZ\\ \varepsilon_{k,\nu}\in I^{\lambda}_{n,\nu}}} \varepsilon_{k,\nu}|O^{n,\lambda,\nu}_{k,0,i}|^2 = \sum_{\substack{k\in 1.BZ\\ \varepsilon_{k,\nu}\in I^{\lambda}_{n,\nu}}} \varepsilon_{k,\nu}\frac{|V^{\nu,i}_k|^2}{|\gamma^{\nu,i}_{n,\lambda}|^2} \sim \Lambda^{-n}$, one gets for the Hamiltonian:

$$H = H_{imp} + \sum_{n,\lambda}\sum_{\nu,i}\xi^{n,\lambda}_{i,\nu}(a^{n,\lambda,\nu}_i)^\dagger a^{n,\lambda,\nu}_i + \sum_{n,\lambda}\sum_{\nu,i}\gamma^{\nu,i}_{n,\lambda}\left(d^\dagger_i a^{n,\lambda,\nu}_i + h.c.\right)$$

D.4. Second Transformation (mapping on semi-infinite tight-binding-chain)

In a second transformation the Hamiltonian will be transformed to a semi-infinite tight-binding-chain for iterative diagonalization. To do that, an orthogonal transformation $U^{\nu,i}_{m,(n,\lambda)}$ is defined so that with $a^{n,\lambda,\nu}_i = \sum_{m=1}^{\infty} U^{\nu,i}_{m,(n,\lambda)} f^{\nu,i}_m$ the Hamiltonian has the following form:

$$H = H_{imp} + \sum_{\nu,i}\left\{t^{\nu,i}_0(d^\dagger_i f^{\nu,i}_1 + h.c.) + \sum_{m=1}^{\infty} t^{\nu,i}_m((f^{\nu,i}_m)^\dagger f^{\nu,i}_{m+1} + h.c.) + \sum_{m=1}^{\infty}\epsilon^{\nu,i}_m (f^{\nu,i}_m)^\dagger f^{\nu,i}_m\right\}$$

The transformation $U^{\nu,i}_{m,(n,\lambda)}$ is usually calculated iteratively for increasing m and the resulting hopping amplitudes $t^{\nu,i}_m$ and site energies $\epsilon^{\nu,i}_m$ usually inherit the $\Lambda^{-\frac{m}{2}}$ and Λ^{-m} dependence from $\gamma^{\nu,i}_{n,\lambda}$ and $\xi^{n,\lambda}_{i,\nu}$, respectively.

Bibliography

[1] Camille Aron and Gabriel Kotliar. Analytic theory of hund's metals: A renormalization group perspective. Phys. Rev. B, 91:041110, Jan 2015.

[2] H. Bruus and K. Flensberg. Many-Body Quantum Theory in Condensed Matter Physics: An Introduction. Oxford Graduate Texts. OUP Oxford, 2004.

[3] Ralf Bulla, Theo A. Costi, and Thomas Pruschke. Numerical renormalization group method for quantum impurity systems. Rev. Mod. Phys., 80:395–450, Apr 2008.

[4] Antoine Georges, Luca de' Medici, and Jernej Mravlje. Strong electronic correlations from hund's coupling. 2012.

[5] Antoine Georges and Gabriel Kotliar. Hubbard model in infinite dimensions. Phys. Rev. B, 45:6479–6483, Mar 1992.

[6] Antoine Georges, Gabriel Kotliar, Werner Krauth, and Marcelo J. Rozenberg. Dynamical mean-field theory of strongly correlated fermion systems and the limit of infinite dimensions. Rev. Mod. Phys., 68:13–125, Jan 1996.

[7] Walter Metzner and Dieter Vollhardt. Correlated lattice fermions in $d = \infty$ dimensions. Phys. Rev. Lett., 62:324–327, Jan 1989.

[8] Andrew K. Mitchell, Martin R. Galpin, Samuel Wilson-Fletcher, David E. Logan, and Ralf Bulla. Generalized wilson chain for solving multichannel quantum impurity problems. Phys. Rev. B, 89:121105, Mar 2014.

[9] W. Nolting. Grundkurs Theoretische Physik 7: Viel-Teilchen-Theorie. Springer-Lehrbuch. Springer Berlin Heidelberg, 2014.

[10] Ulrich Schollwoeck. The density-matrix renormalization group in the age of matrix product states. 2010.

[11] K. M. Stadler, A. K. Mitchell, J. von Delft, and A. Weichselbaum. Interleaved numerical renormalization group as an efficient multiband impurity solver. Phys. Rev. B, 93:235101, Jun 2016.

[12] K. M. Stadler, Z. P. Yin, J. von Delft, G. Kotliar, and A. Weichselbaum. Dynamical mean-field theory plus numerical renormalization-group study of spin-orbital separation in a three-band hund metal. Phys. Rev. Lett., 115:136401, Sep 2015.

[13] Katharina M. Stadler. Towards exploiting non-abelian symmetries in the dynamical mean-field theory using the numerical renormalization group. Master's thesis, Ludwigs-Maximilians-Universität München, Germany, 2013.

[14] D. Vollhardt, K. Byczuk, and M. Kollar. Dynamical mean-field theory. 2011.

[15] A. Weichselbaum. Discarded weight and entanglement spectra in the numerical renormalization group. Phys. Rev. B, 84:125130, Sep 2011.

[16] Andreas Weichselbaum. Non-abelian symmetries in tensor networks: a quantum symmetry space approach. 2012.

[17] Andreas Weichselbaum and Jan von Delft. Sum-rule conserving spectral functions from the numerical renormalization group. Phys. Rev. Lett., 99:076402, Aug 2007.

[18] Kenneth G. Wilson. The renormalization group: Critical phenomena and the kondo problem. Rev. Mod. Phys., 47:773–840, Oct 1975.

[19] Rok Zitko. Adaptive logarithmic discretization for numerical renormalization group methods. 2009.

[20] Rok Zitko and Thomas Pruschke. Energy resolution and discretization artefacts in the numerical renormalization group. 2008.

Erklärung

Hiermit erkläre ich, die vorliegende Arbeit selbständig verfasst zu haben und keine anderen als die in der Arbeit angegebenen Quellen und Hilfsmittel benutzt zu haben.

München, 23. September 2016

Andreas Gleis